Ludwig-Maximilians-Universität

Sigillum Universitatis Ludovici Maximiliani

Studying magnetic turbulence with radio polarimetry

Dissertation der Fakultät für Physik

DISSERTATION OF THE FACULTY OF PHYSICS

der Ludwig-Maximilians-Universität München

AT THE LUDWIG MAXIMILIAN UNIVERSITY OF MUNICH

für den Grad des

FOR THE DEGREE OF

Doctor rerum naturalium

vorgelegt von André Henri Waelkens

PRESENTED BY

aus São Paulo, SP (Brasilien)

FROM

München, 19.03.2009

Sigillum Universitatis Ludovici Maximiliani

1. Gutachter: Prof. Dr. Simon D. M. White

REFEREE:

2. Gutachter: Prof. Dr. Hans Böhringer

REFEREE:

Tag der mündlichen Prüfung: 05.06.2009

DATE OF THE ORAL EXAM:

FORTUNATE IS HE WHO HAS BEEN ABLE TO LEARN THE CAUSES OF THINGS.

Virgil

Contents

List of Figures

List of Tables

Zusammenfassung

Magnetisiertes Plasma ist im ganzen Universum vorhanden. Es wird in Sternen, Akkretionsscheiben, Galaxien und Galaxienhaufen beobachtet. Diese Dissertation erkundet die Charakteristika des diffusen magnetisierten Plasmas im interstellaren-Medium (ISM) und intracluster-Medium (ICM).

Um Turbulenz im ISM und ICM zu untersuchen, entwickeln wir eine Schätzfunktion für das Leistungsspektrum der magnetischen Spannkraft, welche die dynamisch wichtigste magnetische Kraft in subsonisch magnetischer Turbulenz ist. Die Schätzfunktion basiert auf Beobachtungen polarisierter Synchrotronemission im Faraday-rotationsfreien Frequenzbereich. Wir betrachten zwei verschiedene Magnetfeld-Szenarien: ein statistisch isotropes Feld und ein schwaches, gerichtetes Feld überlagert von einem statistisch isotropen Feld. Im zweiten Fall ist ausser dem Spannkraft-Leistungsspektrum auch das Magnetfeld-Leistungsspektrum messbar. Die Methode ist exakt für den Idealfall einer statistisch homogenen relativistischen Elektronenverteilung mit einem Energiespektrum mit spektralem Index $p = 3$ und einem isotropen Magnetfeld. Zur Vorbereitung der Anwendung der Methode auf Beobachtungen werden erst synthetische Daten behandelt, welche auf magnetohydrodynamischen Simulationen basieren und welche die Robustheit der Methode bestätigen.

Desweiteren haben wir, um das Magnetfeld der Milchstrasse zu untersuchen, den HAMMURABI Code entwickelt. Dieses Programm erzeugt aus theoretischen dreidimensionalen Modellen des ISMs synthetische Beobachtungen wie Synchrotronstrahlungsfluss, Faradayrotation, Dispersionsmaß und Ablenkungswinkel von hochenergetischen kosmischen Strahlen. Dies ermöglicht den Vergleich von theoretischen Modellen des galaktischen magnetisierten Plasmas mit einer Vielfallt von Beobachtungsgrößen. Wir erläutern einige Arbeiten die auf diesem Code basieren. Insbesondere besprechen wir, warum aufgrund einer Kombination von Rotationsmaßdaten, unpolarisierten und polarisierten Synchrotrondaten, sowie theoretischen Erwartungen an das galaktische Magnetfeld, auf um einen Faktor Zwei größere Skalenhöhe der galaktischen thermischen Elektronen geschloßen werden konnte. Dieses mit HAMMURABI erhaltene Ergebnis wurde vor kurzem in einer unabhängigen Analyse anderer Autoren bestätigt.

Schliesßlich wird untersucht ob der galaktischer kinetischer Sunyaev Zeldovich (kSZ) Effekt die Messungen der kosmischen Hintergrundstrahlung kontaminiert. Wir erproben die Detektierbarkeit des kSZ Effektes indem wir zu diesem Zweck einen optimalen linearen Filter entwickeln und ihn auf einen simulierten Idealfall anwenden. Wir erhalten einen Signal-zu-Rausch Verhältnis von nur 0.1 und zeigen damit, dass der kSZ Effekt als Kontamination der kosmischen Hintergrundstrahlungs vernachlässigt werden kann. Desweiteren zeigen wir, dass das Polarisationssignal, welches durch die Comptonstreuung von kSZ-Photonen erzeugt wird, keine relevante Kontamination der polarisierten kosmischen Hintergrundsstrahlung darstellt.

Abstract

Magnetised plasma permeates the Universe. It is present in stars, accretion discs, galaxies and clusters of galaxies. This dissertation investigates the characteristics of diffuse magnetised plasma in the inter-stellar-medium (ISM) and the intra-cluster-medium (ICM).

To probe turbulence in the ISM and ICM, we develop an estimator for the magnetic tension-force spectrum. It is based on polarised synchrotron emission data in the Faraday-rotation-free frequency regime. The tension force is the dynamically most important magnetic force in subsonic magnetic turbulence. We consider two magnetic field scenarios: a statistically isotropic field distribution, and a statistically isotropic field upon a small mean field. In the latter case the magnetic power spectrum can also be obtained in addition to the tension-spectrum. The method is exact in the ideal case of a homogeneous cosmic ray electron distribution with a power law energy spectrum with a spectral index $p = 3$, and isotropic magnetic fields. The method is applied to mock observations based on magneto-hydrodynamic simulations as a prelude to an application to real observations. We confirm the robustness of the estimator by comparing its output to the corresponding quantities directly computed from the simulation.

Furthermore, to investigate the global Galactic field we developed HAMMURABI. This software tool takes three-dimensional theoretical models for the ISM components and generates mock observations from them. It focuses on the main tracers of our Galactic magnetised plasma such as synchrotron flux, Faraday rotation, dispersion measure and ultra-high-energy-cosmic-ray delflections. HAMMURABI therefore permits us to confront models of the Galactic magnetised plasma with a broad range of real observations. We report on a number of works based on this code. In particular, due to simultaneous constraints of rotation measure, polarised and total synchrotron intensity, as well as theoretical predictions on the magnetic field and cosmic-ray electron distribution, the Galactic electron density scale height was suggested to be about twice as large as previously thought. This result obtained with HAMMURABI was recently confirmed independently by other authors using pulsar dispersion measure data.

Finally, we consider the role of the Galactic kinetic Sunyaev Zeldovich (kSZ) effect as a CMB foreground. We analyse the detectability of the Galactic kSZ effect by means of an optimally matched filter technique applied to a simulation of an ideal observation. We obtain a S/N ratio of 0.1, and demonstrate thereby that the Galactic kSZ effect can safely be ignored as a CMB foreground. Furthermore, we rule out any significant contamination of the polarised CMB signal by second scattering of galactic kSZ photons.

Chapter 1

Introduction

Nearly all of the visible universe is plasma. This work focuses on methods to achieve a better understanding of a particular class of cosmic plasmas, the diffuse magnetised plasmas, which are ubiquitous in the inter-stellar-medium (ISM) and the intra-cluster-medium (ICM).

These magnetised plasmas are an unique laboratory for magneto-hydro-dynamics (hereafter MHD), presenting us with the possibility to observe conditions which are attainable neither in numerical nor in laboratory experiments on Earth. Their study is paramount for shedding light on MHD turbulence and dynamo processes, on how the magnetic fields are amplified from seed fields and how they are mantained, as well as how the topology of observed magnetised plasmas is attained. For dynamo models for galaxies, our Galaxy offers the only detailed view into the inner workings of such a system, while extra-galactic observations provide a bird's-eye view on dynamos.

The properties of the magnetised ISM and ICM can be indirectly probed by a number of tracers such as synchrotron radiation, Faraday rotation measure, dispersion measure, the Sunyaev-Zeldovich effect, Zeeman splitting, free-free emission, ultra-high-energy-cosmic-ray deflection and dust emission as well as absorption. In this dissertation we explore these tracers as a means for constraining the properties of diffuse magnetised plasmas.

Moreover, the comprehension of the magnetised ISM and ICM is required for understanding processes such as the heat flow, cosmic-ray propagation and molecular cloud collapse as well as the associated star formation.

Additionally, the emission processes related to the magnetised plasma, in particular in the ISM, are often interfering with the detection of other interesting signals. For example, there was recently a claim of a so called WMAP haze (Hooper et al., 2007), an unusually steep synchrotron emission region near the Galactic plane. This is speculated to originate from synchrotron emission of high energy electrons produced by dark matter annihilation in the Galactic magnetic field. However, there are other Galactic emission mechanisms which make the detection uncertain. A better understanding of the magnetized ISM would help us to disentangle the different Galactic emission processes. Finally, the challenge to understand

Galactic emission is of paramount importance for cosmic microwave background (CMB) experiments. Cleaning these foreground emissions from the CMB signal is vital, in particular, for any CMB polarisation experiments aiming at measuring the extremely faint B-modes, which are believed to be a signature of inflation models (Tucci et al., 2005). Here, unlike in the case of unpolarised CMB fluctuations, the Galactic emission dominates over the cosmological signal at all frequencies.

In this work we develop and implement methods to probe the properties of diffuse magnetised cosmic plasmas on all scales accessible to observational resolution.

In the following we present an overview of the relevant diffuse cosmic magnetised plasmas to be studied by the methods developed in this work. We describe their characteristics and investigate through which observations and techniques information on their properties can be obtained.

The multitude of other plasma-dominated environments in astrophysics, such as accretion discs, solar and stellar atmospheres and winds are not addressed in this work.

1.1 Cosmic plasma everywhere

We want to focus on typical observations of diffuse magnetised plasmas targeted on two different classes of objects: the ICM in galaxy clusters and the ISM in external galaxies as well as our own Galaxy.

1.1.1 Magnetised ICM

Clusters of galaxies are the largest compact objects in the Universe. They are filled with very hot plasma with temperatures of a few to several keV. This is not a surprising fact. Galaxy clusters are the largest gravitational potentials around and therefore swallow the matter in their vicinity. This heats up by the energy gained during its infall. Due to the large virial temperature of clusters, all of the captured baryonic matter will be highly ionised.

Moreover, this plasma is also known to be magnetised with typical magnitudes for the field strength being around a couple of μG, while the origin of these magnetic fields is not well understood. The problem to understand the field's origin, as it was thought when people first addressed the issue of dilute astrophysical magnetic fields, arises from a mismatch in timescales. We know that the magnetic fields in the cosmos have a decay time $t_{decay} = \mathcal{L}/\mathcal{R}$. Here $\mathcal{L}$ is the inductance and $\mathcal{R}$ is the extremely small resistivity due to the correspondingly high conductivity in diffuse cosmic plasmas. For ICM conditions this time scale is much larger than the Hubble time. This means that once there is a field, it will stay around for a very long time, but conversely, if there is none, it is hard to create one. This property also leads to the magnetic phenomenon of flux freezing in the fluid, which can be assumed for plasmas in the ISM and the ICM for most of the observable scales.

Thus, if the Universe was simply born with a primordial field and flux freezing holds, the observed fields could have originated from such a primordial field which should have been further amplified by the compression of the plasma in gravitational flows. However, this hypothesis is somewhat disfavoured due to difficulties in explaining observations of fields in spiral galaxies. Their morphology does not agree with the field winding pattern expected due to galactic rotation (but see Howard & Kulsrud, 1997).

Although flux freezing has been used as an argument for sustaining the observed fields in clusters (Carilli & Taylor, 2002), it is not sufficient to explain the presence of small-scale field structures (Subramanian et al., 2006). These will be generated by random flows in galaxy clusters which tangle up the frozen-in fields. However, these will then drive motions via the Lorentz force, and these motions will decay, plausibly in the form of decaying MHD turbulence. What is meant by turbulent decay is that the energy of the original tangled field configuration, distributed over a range of scales, will cascade down to smaller scales where it eventually dissipates. It is observed to do so, by which mechanism though is still a matter of debate. The turbulent decay time in clusters is estimated to be 10^8yr (while the Hubble time is about $1.4 \cdot 10^{10}$yr), irrespective of the resistivity $\mathcal{R}$ or even viscosity of the gas. In other words, the turbulent field component should become negligibly small without a constant input of kinetic energy to regenerate the magnetic energy spectrum.

Galaxies also have magnetic fields, and are therefore candidates for providing the field in the ICM. The question of galactic magnetic field origin and properties is left for the next section. Observations show that the intra-cluster gas is enriched with metals, which should originate from galaxies, therefore it is reasonable to expect that some of the galactic fields were also stripped into the ICM. If a galactic field B_{ISM} is typically of order 3μG, the injected field into the cluster can be estimated to be $B_{ICM} \simeq (\rho_{ICM}/\rho_{ISM})^{2/3} B_{ISM}$ using magnetic flux conservation under the simplifying assumption of a spherically symmetric expansion of the gas. This mechanism will produce fields in the intra-cluster medium of the order of $B_{ICM} \simeq 0.03 - 0.1\mu G$, given that $\rho_{ICM}/\rho_{ISM} \simeq 10^{-3} - 10^{-2}$. This value falls short by about an order of magnitude of the observed cluster values of some few μG.

Other candidates for ICM fields are the outflows of active galaxies such as radio galaxies and quasars. Still, estimates on the field strength provided by those mechanisms are of the order of $0.1 - 1\mu$G.

The widely accepted explanation for the ICM magnetisation problem is believed to be the presence of an astrophysical dynamo. A dynamo can amplify existing seed magnetic fields to the observed values. These seed fields could have arisen in the cluster's history from a number of different sources as we have described.

Ever since the 19th century people like M. Faraday and Anyos Jedlik already knew about dynamo processes, but it was only in 1919 that Larmor (1919) suggested them to be responsible for astrophysical magnetic fields. A dynamo consists of the motion of charged particles in a magnetic field in such a way that it sustains and enhances a magnetic field. It can be seen that

this is in principle possible when looking at the ideal MHD induction equation

$$\partial B/\partial t = \nabla \times \left(\vec{u} \times \vec{B}\right) . \tag{1.1}$$

Here $\vec{u}$ is the velocity of the plasma and $\vec{B}$ is the magnetic field. We stress that a dynamo only enhances an existing magnetic field. It cannot create it, as can be understood from the equation above. Thus, dynamos require magnetic seed fields, of which we listed a number of candidates. A satisfactory dynamo model has then to amplify the seed field to observed values in the available time interval. The magnetic fields in galaxy clusters are thought to be amplified by fluctuating dynamos (the average field strength remains zero, hence the name), driven by the random flow of the electrically conducting fluid. This mechanism, unlike for the Earth, Sun, or our Galaxy, does not require any rotation, only an environment where random motions are constantly stirred. We also stress that the appearance of dynamo action is not constrained to the condition of ideal MHD.

Furthermore we can infer from the equation above that structure formation, which mainly defines the flow velocity $\vec{u}$ in galaxy cluster environments, leaves an imprint in the properties of the observed magnetic fields. The reverse is not necessarily true, since the energy density of the magnetic field in clusters is much smaller than the energy density of motion of the gas. The situation seems to be different in galaxies and star formation regions, as we will discuss later.

The fluctuating dynamo requires turbulent motions. The question is: what is stirring the gas? People assumed originally that the stirring comes from the turbulent wakes of cluster galaxies moving through the ICM (see e.g. Ruzmaikin et al., 1989). However, this would be only efficient if galaxies retain a large fraction of their gas. However in the cluster atmospheres galaxies are suffering from severe ram pressure gas stripping. A galaxy without gas will generate a turbulent wake only by gravitationally dragging the ICM, however this is not strong enough to drive turbulence in the ICM which can maintain μG magnetic fields. Later it was realised that mergers of clusters are the main drivers of ICM turbulence (Roettiger et al., 1999). Furthermore radio galaxy jets and buoyant radio lobes in galaxy clusters can also stir turbulence in their vicinity.

Finally, the magnetic topology in the ICM largely determines the preferred direction of cosmic ray diffusion and the heat conducting flows. For a better understanding of both processes an improved knowledge of turbulent magnetic fields in clusters would be helpful.

1.1.2 Magnetised ISM of the Milky Way and other galaxies

As in the case of clusters, galaxies are filled with plasma, though much colder given the smaller gravitational wells. Typical values for the Milky Way gas temperature are 8000K in the solar vicinity, orders of magnitude lower than that of the intra-cluster-plasma.

Studies of magnetised plasmas in galaxies usually focus their attention on spiral galaxies, mainly because their magnetic fields are easier to observe. Their high star formation rate implies a large cosmic ray production in super-nova shocks and also injects turbulence which drives the

magnetic dynamo. The cosmic-ray electrons spiral around the magnetic field lines and thereby emit synchrotron radiation, making the galaxy visible at radio wavelengths.

Moreover, we live in a galaxy, which provides us with a panorama on the inner workings of a dynamo with a richness of detail unattainable in external galaxies.

Observing magnetic fields in elliptical galaxies instead is more cumbersome. Although elliptical galaxies certainly have significant magnetic fields, they do not produce much synchrotron emission given the lack of cosmic rays due to their low star formation rate (Widrow, 2002). Moreover, the coherence length of the magnetic fields is lower than in spirals (Moss & Shukurov, 1996). Due to the resulting strong beam depolarisation effects, observations of polarised synchrotron as well as polarised dust emission are difficult. The existence of fields in those types of galaxies has to be probed by other means such as Faraday rotation (we get back to that in the next section).

We note that magnetised plasmas have also been observed in irregular galaxies. Recent results on a dwarf irregular galaxy with weak signs of global rotation indicate a regular magnetic field of the scale of the galaxy with an amplitude of $6 - 8\mu$G (Chyży et al., 2000), similar to those typically observed in spiral galaxies. However, fields tend to be mostly chaotic in irregular galaxies.

The plasma in spiral galaxies contains ordered fields on scales which range over the entire galaxy. We will refer to this as the galaxies' mean field structure. Additionally it also contains a turbulent component. Both are of the order of a couple of μG. The topology of the magnetic field is observed to be related to the spiral structure. Magnetic spiral arms follow their density counterparts, however, the ratio of regular to random component is highest in between the arms and lowest in the high density regions of spiral arms.

One should note that a picture of a standard spiral-galaxy-plasma is contradicted by large variations among different galaxies as observations reveal. Currently, there are about 50 spiral galaxies with known magnetic structure. A sizable number of those do not fit into the standard picture. Some show magnetic spiral arms without corresponding density counterparts as seen in observations of flocculent galaxies. Some seem to have extreme field strengths up to 50μG, such as M82, which also has an anomalously high star formation rate. And there exist massive density spiral arms which show a strong regular field associated with them, in contrast to the otherwise more regular inter-arm field in most spirals.

As for the case of clusters, it is thought that dynamo action is responsible for amplifying small seed fields to the observed field strengths. The difference to clusters is the existence of a mean field. Attempts to explain its origin have lead to the development of the so called mean-field dynamo theory (Steenbeck et al., 1966).

The alternative hypothesis that the galactic fields originate from primordial fields first proposed by Hoyle in the 1950s has difficulties. The observed spiral structure should be attained after only two or three full rotations of a galactic disc. Should the winding continue for some 50 turnovers or so, the field lines would present a much larger number of reversals as a function

of radius than observed. Moreover it was argued that these fields should diffuse away from the galaxies due to turbulent motions (Parker, 1973). However, see Howard & Kulsrud (1997) for an alternative view.

We argued in the previous section that the seed fields required by the fluctuating dynamo in clusters were probably provided by galaxies living within the cluster. Attempts at explaining on how the fields originated in the galaxies in the first place suffer from a lack of observational constraints, given the difficulty in observing primordial magnetic fields at high redshifts. What is required is a way of generating currents from scratch, a battery. There were several such mechanisms proposed and the most famous one is the Biermann battery (Biermann, 1950), which can produce small fields up to $10^{-12}\mu$G. Most of battery mechanisms rely on the different masses of the positive and negative charges in the neutral ionised plasma. In other words, ions are much heavier than the electrons in the plasma. Gravity and pressure gradients act differently on electrons and ions, which leads to charge separation and hence generates an electric field. If this has a non zero curl e.g. generated by non-aligned electron pressure and density gradients, Faraday's law of induction states that magnetic fields will be generated.

Such battery mechanism have probably produced the first fields in stars, which were then amplified by stellar dynamos. Stellar winds and supernovae explosions have then carried those stellar fields into the ISM of the galaxy, where it should have been further amplified by a galactic dynamo.

The galactic mean-field dynamo depends on the differential rotation of the galaxy. Let us illustrate this point (see also Parker, 1970; Widrow, 2002) with a toy case. The differential rotation winds up the frozen-in magnetic field lines, such that the field becomes toroidal. These fields are twisted by the Coriolis forces arising when ISM gas is lifted above the galactic plane due to supernovae explosions. This produces toroidal currents which imply the appearance of poloidal fields. These are then, again by differential rotation, twisted back into toroidal fields, and the cycle begins again. We note that mean-field dynamo action depends on the star formation rate, due to the necessary ingredient of supernova explosions lifting gas and driving the turbulence.

On small scales the ISM plasma is in a turbulent state. The frozen-in field lines are stretched and bent by turbulent motions of the gas. The magnetic field lines conversely resist deformations by exerting Lorentz force on the plasma. Energy and momentum injected at large scales are gradually passed on to smaller scales by turbulent decay until they eventually reach the dissipative scale, i.e. where magnetic flux is thought to be destroyed by non ideal MHD processes. The spectrum of velocity fluctuations in the ISM gas is observed to follow a power-law with spectral index of $-5/3$ (a characteristic predicted by turbulence theory Kolmogorov (1941)) which is claimed to hold over 12 orders of magnitude (Armstrong et al., 1981). We note however that this result is based on an interpretation of observations which could be misleading (Lazarian, 1992).

Magnetic fields in galaxies are dynamically important. Simulations suggest they have the

effect of smoothing out the ISM structure (Price et al., 2008). Furthermore, magnetic fields may prevent molecular cloud's from collapsing. In the event of a collapse they influence the cloud structures in the often observed regime where magnetic pressure dominates over gas pressure (Price & Bate, 2008), by suppressing accretion from the cloud on to the cores where star formation happens. Moreover, simulations suggest that magnetic fields suppress fragmentation in collapsing clouds (i.e. they tend to homogenise the clouds density distribution), due to the extra pressure supplied by the magnetic field which is not subject to the radiation losses from which the gas pressure suffers.

Finally, cosmic-ray diffusion within galaxies depends also strongly on the magnetic fields morphology and strength.

1.2 Target Properties

In the previous section, we sketched the state of our knowledge on properties and characteristics of the diffuse cosmic plasma in the ISM and the ICM. It is now our objective to draw attention to the set of observable properties which allow us to probe the workings of cosmic magnetised plasmas.

1.2.1 Magnetic field topology

Magnetic field structures are usually separated into large-scale and small-scale fields. This distinction is somewhat arbitrary. Most observational works draw the line between large-scale and small-scale fields where ordered structure can no longer be recognised with increasing observational resolution. We will follow the same approach. Of the objects we described, galaxy clusters do not present observable large-scale magnetic features. Only spiral galaxies are observed to have coherent large-scale fields, with some exceptions observed in irregular galaxies. Elliptical galaxies are currently not believed to have large-scale fields (Moss & Shukurov, 1996), however observations are difficult and thus very scarce.

Determining the properties of the large-scale fields of galaxies is important for a number of scientific applications.

Dynamo theory

Explaining the topology of large scale structure in spiral galaxies, such as field reversals between spiral magnetic arms, is paramount for any successful mean-field dynamo theory. The bends and twists inflicted on the field by the differentially rotating galactic disk evolve into the structures we see nowadays. The precise determination of the topology of that large-scale field would constrain the range of acceptable dynamo models.

UHECR origins

The large-scale magnetic field structure in the Galaxy, and possibly also the extra-galactic field, deflects ultra-high-energy-cosmic-rays (UHECRs). The origin and composition of UHECR particles is one of the major open questions in contemporary astrophysics. It is not clear whether or not they were created in say active galactic nuclei (such as BLLacs) or gamma ray bursts, nor by what mechanism.

Therefore, it would be important if the paths of UHECRs could be traced back trough the cosmic magnetised plasma which would permit us to determine what the sources of these particles are.

There are two major constraints on this problem. For lower energies, and thus smaller Larmor radii, UHECRs rapidly become isotropised due to their strong deflection in magnetic fields in the ISM and the inter-galactic-medium (IGM). The observations with the Auger astronomy array confirm a sharp transition from isotropy (where no back-tracing is possible) to anisotropy at energies of about $\propto 60\,\mathrm{EeV}$ ($\mathrm{EeV} = 10^{18}\mathrm{eV}$). For higher energy particles another constraint arises in the form of the CMB radiation field which becomes optically thick to severe photon-pion energy losses, the so-called GZK effect (Greisen, 1966; Zatsepin & Kuz'min, 1966). This implies that particles with energies above $\approx 60\,\mathrm{EeV}$ should originate not much farther than 100 Mpc away.

The measurements done with the Pierre Auger observatory show that UHECR particles of energies larger than 57 EeV have anisotropic arrival directions (so far 27 published events, The Pierre Auger Collaboration (2007)). Considering estimates for the deflection in Galactic magnetic fields of about $3 - 8\,\mathrm{deg}$, while the observatory has a precision of about 1 deg, a correlation of the arrival directions with the local large-scale structure was reported (The Pierre Auger Collaboration, 2007). In particular, there are indications that a correlation with active-galactic-nuclei is favoured, although this latter point is debated.

The precise knowledge about the extra-galactic and Galactic large-scale fields is a limiting factor when trying to determine from where the detected UHECRs originate. The particles travel overwhelmingly trough extra-Galactic space. The magnetic field there is believed to be concentrated in the large-scale structure filaments and clusters and should be tangled. UHECRs crossing clusters (μG fields) are certainly deflected to a degree which prevents back tracing, while those crossing voids are thought to travel unhindered. The amount of deflection in filaments is debated. For those, only theoretical estimates for the field strength exist, ranging from a fraction of μG to a fraction of nG. Unlike galaxies and clusters, filaments did not have time to complete their dynamo amplification and the estimated fields are thus sensitive to the assumed seed fields and the filaments age. Current estimates of UHECR deflection assume the Galactic field, even though it dominates only over a fraction of the UHECRs trajectory, to be the most significant contribution for deflections.

ISM tracers and CMB foregrounds

An understanding of the large-scale structure of the Galaxies magnetic field is also very important for a number of ISM tracers such as synchrotron radiation, Faraday rotation, dust emission and absorption, which we will be discussing in more detail in the next section. All these physical processes are due to interactions of particles or photons with the magnetised plasma. Therefore, any improved knowledge on either of them, the field, the particles or the photons travelling trough the Galaxy, will imply something about the others. Moreover, in the case of our own Galaxy, a good characterisation of the emission mechanisms is of paramount importance for CMB experiments. In particular CMB polarisation experiments will be highly dependent on the ability to subtract polarised foregrounds from the CMB signal. Unlike in the case of unpolarised CMB radiation, the polarised foregrounds dominates over the so called B-mode polarisation signal in the CMB. The measurement of such B-modes would be seen as a smoking gun for inflation theory, or at least a large subset of it (since inflation models which do not predict B-modes also exist, see e.g. Baumann et al. (2008)).

1.2.2 Turbulent magnetic fields

We observe disordered fields in all diffuse magnetised cosmic plasmas. While galaxy clusters present tangled magnetic fields only, spiral galaxies present random fields below scales of about 1 kpc. Studying those plasmas allows us to constrain possible MHD scenarios in an environment which is not reproducible in any experiment nor simulation on Earth. The latter is due to the computational limitations given the huge Fourier range over which one would have to run the simulation. Moreover, characterising the turbulent random flows of the magnetised plasma is relevant for dynamos in the ICM and the ISM. In the latter, the presence of cyclonic like motions in the plasma is defining for the mean-field dynamo.

MHD turbulence theory can be seen as essentially an attempt to reproduce Kolmogorov's ideas for hydrodynamic turbulence (Kolmogorov, 1941) on magnetised plasmas.

Kolmogorov's theory assumes an energy injection scale, a much smaller energy dissipation scale, and in between these, the inertial range, where energy cascades down to smaller scales at a constant rate in the so called turbulent cascade. The famous prediction of this theory is the $k^{-5/3}$ power-law for the energy spectrum. As previously mentioned, this has been observed (using various observation methods for the different scales) to hold in the ISMs electron density spectrum over as many as 12 decades of scales (Armstrong et al., 1981). Furthermore the $-5/3$ spectral index has also been observed in galaxy clusters (Enßlin & Vogt, 2003), solar winds and other astrophysical plasma environments.

So far, a description for MHD turbulence along the same lines as Kolmogorov's hydrodynamical turbulence has been elusive and even toy cases are not fully understood (Schekochihin & Cowley, 2007).

Idealised cases such as when there is only one injection scale, i.e. one scale at which energy

is pumped into the system, as well as only one dissipative scale (in MHD they often are different for kinetic and magnetic energy), are at most approximately satisfied in space. In galaxy clusters for example, mergers will be responsible for stirring in a broad range of length scales, making a comprehension of MHD turbulence challenging.

A statistical description of the magnetic turbulence is given by correlation tensors of different orders of the magnetic and the velocity fields. Commonly used quantities are the magnetic power-spectrum, the magnetic tension-force power spectrum, the helicity spectrum and so forth. These are of course not directly observable, however, they can partly be inferred from data as will be shown in this thesis. Obtaining such quantities is paramount for constraining the possible MHD scenarios in the ISM and the ICM.

1.3 Observational methods

Here we will give a brief account on what sort of tracers are commonly used to study the properties of diffuse magnetised plasmas. We focus mainly on their properties and observability, leaving technical considerations for latter.

1.3.1 Dispersion measure

A plasma is a dispersive medium, therefore electro-magnetic waves of different frequencies will travel trough it at different speeds. Thus, a wave form that incorporates a range of frequencies will change shape as it propagates. A sharply peaked wave typically flattens out. Pulsars are named precisely after this property of emitting sharply peaked waves at regular intervals. The arrival time t_a of a signal originally emitted by the pulsar simultaneously at all wavelengths will be different for each observation frequency ν. It will be a function of the thermal electron density n_e between the observer "*here*", and the pulsar location "*there*" along the line-of-sight (LOS) according to

$$t_a \propto \nu^{-2} \int_{here}^{there} dr\, n_e = DM\, \nu^{-2}\,. \tag{1.2}$$

Here r is the radial distance along the LOS and the dispersion measure is $DM = \int_{here}^{there} dr\, n_e$. It can be determined from the difference of arrival time measurements Δt_a at two distinct frequencies $DM = A\Delta t_a(\nu_1^{-2} - \nu_2^{-2})$ (where A is a constant). Now, if the distance to the pulsar is known, then the average electron density for that LOS can be computed. Conversely, if an average n_e is known, we can use DM for estimating distances of pulsars. Furthermore, if several pulsars exist along the LOS, then information about sections of the LOS can be inferred. In other words, say we have a pulsar at $there_1$ and the other at $there_2$, both along the same LOS. Then information about the electron density in between these two positions can be inferred, giving us three dimensional information on the thermal electron distribution. Thus DM's are a powerful tool to study the ISM structure of our Galaxy. The state of the art electron density models for

the Galaxy are based mainly on pulsar dispersion measurements (Cordes & Lazio, 2002, 2003). These models are crucial for interpreting RM data adequately. Upcoming radio telescopes such as the SKA are expected to offer a great wealth of such pulsar data (Beck & Gaensler, 2004).

1.3.2 Faraday rotation

Faraday rotation is the change of the polarisation angle χ of an electro-magnetic wave travelling trough a magnetised plasma as described by

$$\chi = RM\,\lambda^2 + \chi_0\,. \tag{1.3}$$

Here χ_0 is the intrinsic polarisation angle, i.e. the angle before the radiation has undergone any Faraday rotation. The rotation measure

$$RM \propto \int_{here}^{there} dr\, n_e\, B_{LOS} \tag{1.4}$$

will reveal LOS properties of the magnetic field B_{LOS} in the ISM or ICM, as well as the thermal electron number density n_e, in between *here* and *there*. The electron density distribution can be inferred from DM data, as seen in Sect. 1.3.1. Hence, having an idea of what n_e looks like, we can read of the average LOS magnetic field B_{LOS} between *here* and *there*. Analogously to the DM case, obtaining the RM for two different polarised sources at different radial distances along the same LOS allows us to infer properties of the field also in the interval between these two sources. We note that even when the electron density model is not know, RM data are still an useful tool for constraining magnetic field properties. Consider the example given in Fig. 1.1, where the RM is plotted as a function of the DM obtained for a number of pulsars approximately along the same LOS. In such a plot, the negative slope of the curve implies that the large-scale magnetic field component along the LOS is pointing towards the observer, while a positive slope implies a field pointing away from the observer as can be seen from Eq. 1.4. Therefore, the monotonically decreasing curve presented in the figure demonstrates that there is no field reversal along this particular LOS. The white filled squares, by the way, are not considered in this analysis since they are known to be associated to HII regions, which are observed to posses strong tangled magnetic fields[1] uncorrelated to the ISM field topology. Currently the number of pulsars with known RM and DM is of the order of 1000. Observatories like the SKA are estimated to increase that number to about 20.000 sources, greatly improving our knowledge about the large-scale structure of the magnetic field of the Galaxy (Beck & Gaensler, 2004). Apart from pulsars in the ISM, the Galactic magnetised plasma can also be probed by the comparatively less sparse extra-galactic polarised sources.

[1] It is believed that the magnetised plasma which collapsed/compressed to produce the star-forming and consequently HII region is tangled up due to the angular momentum of the collapsing cloud as well as due to stirring by the star formation processes.

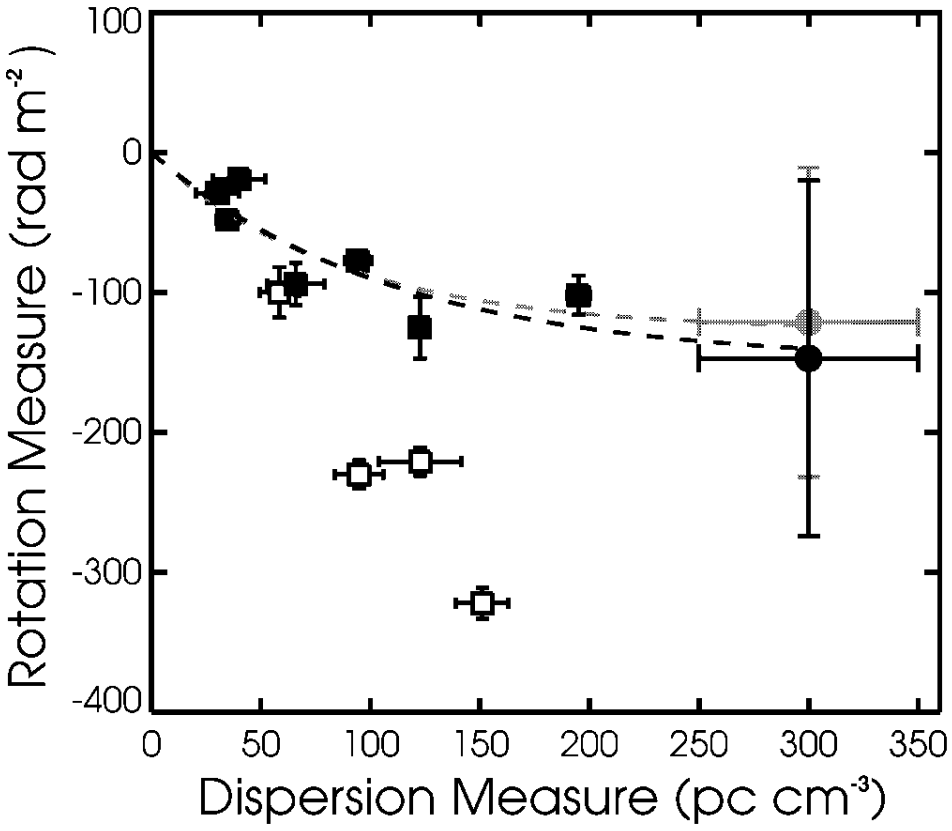

Figure 1.1: In this plot from Brown et al. (2003), the RM is plotted as a function of DM. The slope of the curve is always negative, which indicates that the LOS magnetic field in this direction points towards the observer. The white filled squares are measurements associated with HII regions and are not considered when fitting the displayed curves.

RM observations are also an unique way of probing the magnetised plasma in elliptical galaxies. The low star formation rate and consequent low cosmic-ray electron density does not permit to probe the magnetised plasma of these objects with synchrotron radiation. The dust density is also low, depleted for forming stars, therefore no polarised dust emission can be observed either. The challenge is thus to find strong enough polarised radio sources, such as radio jets and radio lobes, inbeded in the galaxy or behind it to be able to perform Faraday rotation measurements.

Finally, RM data has also been used to measure properties of turbulent magnetic fields in the ICM. The idea is that a large polarised source behind or inbeded in a cluster permits the construction of RM maps which reveal the magnetised ICM plasma between it and the observer. Here the electron density profile, given the much hotter plasma in clusters, can usually be obtained from X-ray observations. The fluctuations in the RM maps are a consequence of the fluctuations in the LOS integral of the turbulent magnetic field of the cluster. It can be shown that these RM fluctuations can be used to infer the magnetic power spectrum in galaxy clusters (see e.g. Enßlin & Vogt, 2003).

1.3.3 Synchrotron radiation

The most commonly used tracer of magnetised plasmas is synchrotron radiation. Charged particles with relativistic energies spiralling around in the magnetic field emit synchrotron radiation. Due to the relativistic beaming effect the emission is directed along the particle's velocity vector. At lower energies, and consequent lower emissivity, relativistic beaming does not happen, and one speaks of cyclotron radiation.

The charged particles which generate synchrotron emission in the ISM and the ICM are overwhelmingly cosmic-ray electrons. Protons and other charges emit very little, given their larger mass. The cosmic-ray electrons are assumed to have a power-law energy distribution $N(\gamma)\,d\gamma = C\,\gamma^{-p}\,d\gamma$. The quantity $\gamma = (1-\beta^2)^{-1/2}$ is the Lorentz factor, $N(\gamma)$ is the number density of particles in the interval $[\gamma, \gamma + d\gamma]$, p is the spectral index and C is dependent on the position in space while $\beta = v/c$, where v is the electron velocity and c the speed of light. The assumption of a power-law is motivated by shock acceleration theory (Drury, 1983) and is compatible with observations of cosmic-ray electron energies in the Earth's atmosphere over a large energy range. Furthermore we assume that cosmic-ray electrons propagate isotropically, which is confirmed by orbital experiments. The resulting synchrotron emissivity at a given position is

$$j \;\propto\; \nu^{\frac{1-p}{2}} B_t^{\frac{p+1}{2}} C\,. \tag{1.5}$$

Here ν is the observation frequency and B_t is the magnetic field component perpendicular to the LOS. The observed flux is given by

$$\mathrm{I}(\nu) = \int_0^\infty dr\, d\Omega\; j(r)\,, \tag{1.6}$$

where Ω is the solid angle while r is the radial distance along the LOS. The polarised flux is

$$P(\nu) = \int_0^\infty dr\, d\Omega\; j(r)\cdot f(p) e^{-2i\chi(r\vec{\hat{n}})} \tag{1.7}$$

where $f(p) = \frac{p+1}{p+7/3}$ is the polarisation fraction and χ is given by Eq. 1.3. Note that even without any Faraday rotation, say at very high frequencies, χ will still give the dependence on the intrinsic polarisation angle χ_0, i.e. at what polarisation angle the radiation is first emitted. The synchrotron flux also follows a power-law given by the spectral index $\alpha = (1-p)/2$.

The validity of the assumption of a power law is further strengthened by works on CMB foreground subtraction, which have so far been successful at recovering cosmological parameters by foreground-cleaning CMB maps assuming synchrotron emission with a constant spectral index. Recent works however start considering more complex spectral behaviour. CMB polarisation experiments aiming at measuring B-modes will have to be extremely precise about their foreground removal, since polarisation foregrounds, unlike in the unpolarised emission

case, dominate over the cosmological B-mode signal.

When one considers synchrotron emission over a large enough range the power-law spectra assumption breaks down. For example, on frequencies below 400MHz, the synchrotron spectrum flattens (Reich & Reich, 1988a; Reynolds et al., 1999). In other words, if we extrapolate the emission at higher frequencies from this flatter spectrum, we obtain values incompatible with observations. Thus the power law assumption is only valid over limited frequency ranges.

Polarised synchrotron observations probe the topology of large-scale fields in spiral galaxies. Furthermore, based on so called equipartition arguments, synchrotron emission also traces the magnetic field strength. Equipartition advocates that the energy density in the magnetic field, as well as the energy density in cosmic-ray electrons should be equal, which is often observed, but not understood. It is assumed that an overabundance of relativistic electrons is constantly fed into the magnetised ISM by supernova explosions and consequent shock acceleration. The rate at which particles of high energies escape the galaxy is a function of the magnetic field strength (of course also on the structure of the field, though this is traditionally ignored, or hidden in the assumption that all galactic fields are similar). Therefore, magnetic and cosmic-ray energy densities are at least related. The cosmic-ray electron energy density can be inferred from X-ray emission. Equipartition, if existent at all, may break down in galaxies where star formation is no longer active (e.g. elliptical galaxies).

1.3.4 Polarised dust emission and extinction

On observational frequencies higher than 60GHz, dust emission is the dominant diffuse radiation. This is true both in the unpolarised, as well as in the polarised case. Dust particles absorb optical starlight and reemit mainly in the infrared. Approximately 20% of starlight energy in the Galaxy is absorbed and remitted by dust particles.

Polarised dust emission as well as polarised absorption critically depend on grain alignment processes.

The alignment of dust grains is a function of the type of grain and the magnetic field direction, a fact known for over 50 years but only recently claimed to be approaching understanding (Lazarian, 2003).

A consequence of grain alignment is the polarisation of starlight due to extinction. Moreover, the aligned grains also emit circular as well as linearly polarised radiation. Although much theoretical progress has been made on this front, the emission mechanisms of all different dust particles are still not fully understood. In particular, although we clearly measure polarised dust emission, it is uncertain what grains produce it.

Polarised starlight, and polarised dust emission by aligned grains are the principal techniques for studying magnetic fields in molecular clouds. These studies are particularly relevant since star formation is thought to be influenced by magnetic fields in the molecular

clouds. It should be stressed that the reliability of dust polarimetry as a magnetic field tracer is constrained by the limitations in theoretical understanding of the alignment and emission processes, as well as the composition of the dust cloud.

We should also mention so-called spinning dust emission. This emission mechanism has been proposed to explain the so called anomalous dust signal seen by several foreground subtraction works on the lower observational frequencies of WMAP data (the K, Ka and Q, 23GHz, 33GHz, 41GHz respectively). There are two proposed mechanisms: electric-dipole emission or magneto-dipole emission of spinning dust particles. Further details can be found in Draine & Lazarian (1998).

1.3.5 The Sunyaev-Zeldovich effect

The Sunyaev-Zeldovich (SZ) effect describes the inverse Compton scattering of CMB photons by clouds of free electrons such as the ones of the atmosphere in galaxy clusters (Sunyaev & Zeldovich, 1972, 1980). The scattering-induced frequency shift due to the thermal motion in the electron cloud is called the thermal SZ effect, while the kinetic SZ effect is caused by the bulk motion of the cloud. The thermal SZ effect is observed in galaxy clusters due to the very hot plasma residing in them. Their kinetic SZ effect is usually negligible. The picture however changes for galaxies, with their much smaller potential wells containing cooler plasma, as well as much less of it, and therefore leave only a very faint thermal SZ imprint on the CMB photons. In this case, as demonstrated in this work, the kinetic SZ effect is stronger. However, this effect is still too faint to present a detectable signature. Therefore only the thermal SZ effect, and only for galaxy clusters, can practically be used as a diagnostic probe of diffuse plasmas in the cosmos.

1.4 Aims

A direct measurement of the properties of diffuse magnetised plasmas in the cosmos is not possible. However, as we described above, a range of observations associated with different combinations of the physical properties of the magnetised ISM and ICM is accessible, out of which characteristics of the diffuse cosmic plasma can be inferred. In this dissertation we present methods for constraining the magnetised plasma's properties on all observationally accessible scales.

In chapter 2 we derive estimators, based on polarised synchrotron observables, for obtaining statistical characteristics of small scale isotropic magnetic fields. We demonstrate that the tension force power spectrum, as well as the magnetic power spectrum can be written as a function of the synchrotron observation maps. In light of these quantities different MHD scenarios can be discriminated, therefore constraining the properties of small scale field behaviour in the ISM and the ICM.

To study the large-scale properties of the Galactic magnetic field, we present a code for simulating emission processes which trace the magnetised Galactic plasma. It is developed based on three-dimensional input models for the thermal electrons, the cosmic ray electrons and the magnetic field. The resulting mock observations are confronted to the corresponding observational data allowing us to constrain the magnetised ISM properties of the Milky Way. In chapter 3 we present this code, called HAMMURABI. Moreover, the findings of three distinct works are shown as an example application of the code in radio astronomy.

We investigate the importance of the Galactic kinetic Sunyaev-Zeldovich effect as a CMB foreground. In chapter 4 we explain how this was done using an altered version of the HAMMURABI code for computing the expected signal assuming a state of the art thermal electron density distribution, a simple model for the Galaxy rotation curve and standard knowledge about the CMB. It is shown that although the signal is much stronger than the thermal Sunyaev-Zeldovich effect, it can still be safely ignored as a CMB foreground, both in the polarised and in the unpolarised case. Conversely, it can also not be used as a probe for the magnetised plasma properties of our Galaxy.

We present our concluding remarks in chapter 5.

Chapter 2

Probing turbulence with the Stokes correlators

Note: The bulk of this chapter, as well as the Appendix A, is part of a paper submitted to MNRAS (Waelkens et al., 2009b). Sects. 2.2 and 2.4.5 have been added. Sect. 2.5.2 and Appendix A.2.2 have been written by Alexander Schekochihin.

2.1 Introduction

Magnetised plasma is present almost everywhere in the observable Universe, from stars and accretion disks to the interstellar and the intracluster medium (respectively ISM and ICM). A large fraction of this magnetised plasma is in a turbulent state. Understanding the origin of the cosmic magnetic fields and their evolution towards their observed state embedded in magnetised plasma turbulence, apart from being a tantalising intellectual challenge in its own right (Brandenburg & Subramanian, 2005; Subramanian et al., 2006; Schekochihin & Cowley, 2005, 2006; Schekochihin et al., 2007), is also crucial in the construction of theories of large-scale dynamics and transport in many astrophysical systems. For example, magnetic fields are expected to be dynamically important in determining the angular momentum transport in accretion discs (Pringle & Rees, 1972; Shakura & Syunyaev, 1973), to control star formation and the general structure of the ISM (where magnetic fields prevent molecular clouds from collapsing and suppress fragmentation; see, e.g., Price et al., 2008, and references therein), and to play an important role in galaxy discs as well as galaxy clusters, where they influence the viscosity and thermal conductivity of the ISM and ICM (Chandran & Cowley, 1998; Narayan & Medvedev, 2001; Markevitch et al., 2003) and the propagation of cosmic rays (e.g., Strong et al., 2007; Yan & Lazarian, 2008b). Theoretical models of all these phenomena require some assumptions to be made about the spatial structure of the tangled magnetic fields permeating the constituent turbulent plasmas. However, as theory of magnetised plasma turbulence is in its infancy as a theoretical subject, there is no consensus about what this spatial structure is. In

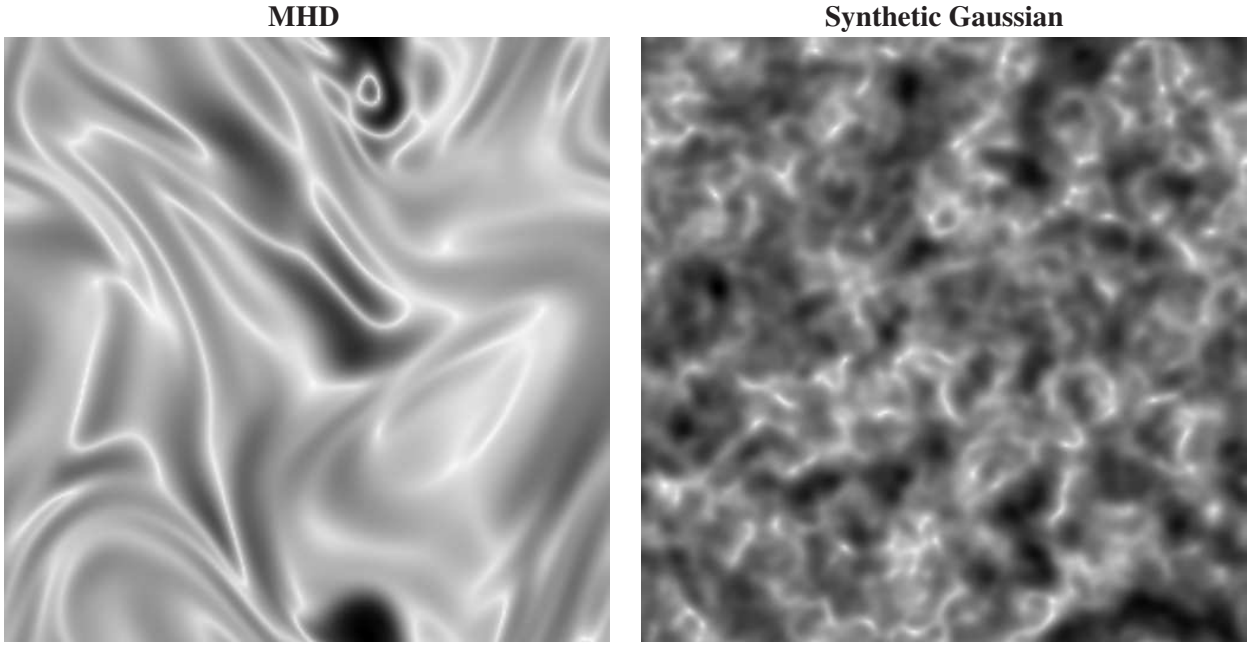

Figure 2.1: *Left panel*: MHD-dynamo-generated magnetic field (Schekochihin et al., 2004) (saturated state of their Run S4). *Right panel*: A synthetic divergence-free Gaussian random field realisation with identical power spectrum. These are cross-sections of the field strength $|B|$ (dark represents stronger field, white weaker field). The magnetic-field and tension-force power spectra are shown in Fig. 2.2.

order to make progress both in understanding the turbulence and in modelling its effect on large-scale dynamics and transport, it is clearly desirable to be able to extract statistical information about the field structure from observational data (Enßlin & Vogt, 2006; Enßlin et al., 2006).

Diffuse synchrotron emission is observed throughout the ISM and the ICM, as well as in the lobes of radio galaxies (e.g. Westerhout et al., 1962; Wielebinski et al., 1962; Carilli et al., 1994; Reich et al., 2001; Beck et al., 2002; Wolleben et al., 2006; Haverkorn et al., 2006b; Reich, 2006; Clarke & Ensslin, 2006; Schnitzeler et al., 2007; Laing et al., 2008). The fact that synchrotron emission is readily observable and is a good tracer of the magnetic-field strength and orientation makes it a key source of information that can serve as a reality check for theories of magnetised plasma turbulence and magnetogenesis (origin of the magnetic fields).

In this work, we will be focusing on how the synchrotron-emission data can be used to characterise the structure of the tangled magnetic fields permeating the ISM and the ICM. In this context we refer to previous studies which sought to recover statistical information about the structure of of these fields in the ICM from the Faraday rotation measure (RM) data (Enßlin & Vogt, 2003; Vogt & Enßlin, 2003, 2005; Govoni et al., 2006; Guidetti et al., 2008), as well as studies of the ISM (Haverkorn et al., 2006a, 2008), also based on the RM data, and the work of Spangler (1982, 1983) and Eilek (1989a,b) based on polarised synchrotron emission data. In formal terms, all of these papers are concerned with at most second-order statistics, namely the magnetic-field power spectrum, or the two-point correlation function of the magnetic field. Our

work complements those previous efforts by drawing on the fact that polarised-emission data carries information about 4th-order statistics of the magnetic field. In particular, we present a practical method for obtaining the tension-force power spectrum. As will be shown in greater detail in the following, this quantity contains statistical information about the spatial structure of the tangled magnetic fields that is missing in the second-order statistics and, most importantly, is actually observable with radio telescopes mapping polarised synchrotron emission.

In Sect. 2.2, we present a brief introduction to ideal magneto-hydro-dynamics (hereafter MHD), which is often a good approximation for describing the magnetised ISM and ICM. In Sect. 2.3, we explain why the tension-force power spectrum is an interesting quantity to measure and how it allows one to diagnose the magnetic-field structure. In Sect. 2.4, we explain the assumptions we make about the magnetic field (Sect. 2.4.1 and Sect. 2.4.2) and the observational data (Sect. 2.4.3; see also Appendix A.1) and propose a method of reconstructing the tension-force power spectrum from the Stokes maps (Sect. 2.4.4 and Sect. 2.4.6). We then generalise our method slightly for the case when a weak mean field is present and show that in this case the power spectrum of the magnetic field itself may be obtainable from the Stokes correlators (Sect. 2.4.7). Most detailed analytical calculations required in this section are presented in Appendix A.2. In Sect. 2.5 we demonstrate the validity of our method by testing it on synthetic observational data generated from numerical simulations. A brief summary and conclusion to the chapter is given in Sect. 2.6.

2.2 Ideal magneto-hydro-dynamics

Studying the plasma in the ISM and the ICM requires a description of its dynamics. On the observable scales of these media it is often a good approximation to assume that ideal MHD governs the dynamics of the magnetised plasmas. Therefore, to better characterise the properties of the magnetised ISM and the magnetised ICM, we offer a brief description of some of the properties of ideal MHD. We stress however that assuming ideal MHD is not required for the work presented here.

In general a plasma is described by MHD if its particles are sufficiently isotropic. Isotropy can be a result of particle-particle collisions, as well as particle-plasma-wave interactions. In dilute environments such as the ICM the latter is the dominant scattering mechanism. The rate of particle scatterings needs to be high enough that the treatment of the particles phase-space density can be simplified to gas kinetics on macroscopic scales. We will present the particular case of ideal MHD. In this case the scattering rate is so high that the pressure P is isotropic and the heat flow is small. We further assume a completely ionised gas (mostly the case in the ISM), making it is unnecessary to deal with a second neutral fluid. Even when the gas is only partially ionised it can still be treated as a single fluid, provided the ion-neutral collisionality is large enough so that charged particles and neutral particles move together (a separate treatment is required, e.g. in star formation regions). In the one-fluid regime the mean density ρ, the mean

velocity $\vec{u}$, the mean pressure P, and the magnetic field $\vec{B}$ as a function of position $\vec{r}$ and time t fully describe the plasma. Following Russel M. Kulsrud (2005) and taking into account that the resistivity in the ISM and the ICM is almost zero, one obtains the ideal MHD equations

$$\begin{aligned} \frac{\partial \rho}{\partial t} + \nabla \cdot (\rho \vec{u}) &= 0\,, \\ \rho \frac{\partial \vec{u}}{\partial t} &= -\nabla p + \vec{j} \times \vec{B}\,, \\ \frac{d}{dt}\left(\frac{p}{\rho^{\gamma}}\right) &= 0\,, \\ \frac{\partial \vec{B}}{\partial t} &= \nabla \times (\vec{u} \times \vec{B})\,. \end{aligned} \tag{2.1}$$

Respectively the continuity equation, the equation of motion, the entropy equation and the magnetic induction equation. These equations determine the temporal evolution of ρ,$\vec{u}$,P, and $\vec{B}$.

2.2.1 Flux freezing

One of the most important properties of an ideal plasma is the phenomenon known as flux freezing. It is a consequence of Eq. 2.1 that $\int_A dA\, \vec{n}\, \vec{B}$ is a constant in time. Here A is some surface while $\vec{n}$ is an unitary vector perpendicular to it. This implies that the magnetic field lines are bodily transported by the plasma, or conversely, that the number of field lines embedded in a volume unit of the moving fluid does not change in time.

The phenomenon of flux freezing in the ISM and ICM can be qualitatively understood as a consequence of the high inductance and low resistivity of the magnetised plasma. A suitable analogy is a simple circuit with an inductor of inductance $\mathcal{L}$ and a resistor of resistivity $\mathcal{R}$, connected to a battery with constant electro-motive-force (emf) ε_0. Solving the resulting differential equation $\varepsilon_0 - \mathcal{L}\frac{dI}{dt} = I\mathcal{R}$ for the current $I(t)$, we obtain the characteristic decay time $t_{decay} = \mathcal{L}/\mathcal{R}$. Now, as it happens $\mathcal{L}$ is very large while $\mathcal{R}$ is very small in the ISM and the ICM. Indeed, the decay time is estimated to be orders of magnitude larger than the Hubble time. As already pointed out in the introduction, there are mechanisms which can transport magnetic fields away from the ISM by turbulent motions (Parker, 1973), or cascade the energy down to scales where ideal MHD no longer holds and the magnetic energy dissipates. This allows fields to decay in timescales much shorter than the Hubble time. The amplification and maintenance of the observed fields is thought to be a consequence of dynamo action (Steenbeck et al., 1966; Parker, 1970, 1973; Subramanian et al., 2006; Schekochihin et al., 2004).

Figure 2.2: *Left panel*: Magnetic-field power spectra for the fields shown in Fig. 2.1. *Right panel*: Tension-force power spectra for the same fields.

2.2.2 MHD Turbulence

Hydrodynamical turbulence attempts to describe the broadband disordered fluctuations in the velocity field of a gas (Kolmogorov, 1941). The cornerstone of this theory is the universality of physics in the inertial range, i.e. in between the injection scale (the large scale at which the fluid is stirred), and the dissipation scale (where the motion energy is dissipated away). For example, whether you stir a cup of coffee with a spoon or a fork should be irrelevant for the fluid motions at any scale in the inertial range. Furthermore, the theory assumes that no special points (homogeneity), special scales (scale invariance), or special directions (isotropy) exist and that interactions between comparable scales dominate (scale locality of interactions). Although the extent to which these assumptions hold in nature is debated. The prediction of a power spectrum of the velocity field with a spectral index $-5/3$ has been shown to be compatible with several observations (e.g. Schuecker et al., 2004; Vogt & Enßlin, 2003, 2005). In particular, such a power spectrum is claimed to have been observed to exist over 12 orders of magnitude in the electron density spectrum in the ISM (Armstrong et al., 1981, 1995; Lazio et al., 2004). However, this latter statement is based on the interpretation of observations which other authors caution might be misleading (Lazarian, 1992).

MHD turbulence is essentially an attempt to adapt this kind of thinking to magnetised fluids. However, mainly based on MHD simulations (with rare exceptions, the main laboratory for such science), it has been realised that key assumptions such as isotropy, locality of interactions and universality of physics in the inertial range, do not hold in several cases. MHD turbulence should explain the amplification, topology and maintenance of the magnetic fields in space (e.g. dynamos), as well as explaining the observations related to transport of heat and cosmic rays (e.g. global temperature profiles in galaxy clusters).

The work we present here is a tool to discriminate between different turbulence scenarios, however, as should be stressed, it does not rely on any turbulence picture at all.

2.3 Motivating the tension-force power spectrum estimator

Turbulent plasmas exhibit in general very complex magnetic structures (see Fig. 2.1), which are best characterised by statistical means. The most widely used quantity for this purpose is the power spectrum

$$M(k) = 4\pi k^2 \langle |\vec{B}(\vec{k})|^2 \rangle, \tag{2.2}$$

where $\vec{B}(\vec{k})$ is the Fourier transform of the magnetic field (see Sect. 2.4.1). The angle-bracket averaging includes averaging over all directions of $\vec{k}$, so the power spectrum measures the amount of magnetic energy per wavenumber shell $|\vec{k}| = k$. It is related via the Fourier transform to the second-order two-point correlation function (or structure function) of the magnetic field. It is an attractive quantity to measure because phenomenological theories of turbulence typically produce predictions for characteristic field increments between two points separated by a distance in the form of power laws with respect to that distance (Kolmogorov, 1941; Iroshnikov, 1963; Kraichnan, 1965; Goldreich & Sridhar, 1995; Boldyrev, 2006; Schekochihin et al., 2007)—and such predictions are most obviously tested by measuring the spectral index (or the scaling exponent of the structure function). However, knowing the spectrum is not enough and can, in fact, be very misleading, for reasons having to do both with the physics of magnetic turbulence and with formal aspects of describing it quantitatively.

All scaling predictions for magnetized plasma turbulence proposed so far are, implicitly or explicitly, based on the assumption that magnetic fluctuations at sufficiently small scales will look like small Alfvénic perturbations of a larger-scale "mean" field (this is known as the Kraichnan 1965 hypothesis). Numerical simulations of MHD turbulence carried out without imposing such a mean field do not appear to support this hypothesis (Schekochihin et al., 2004), although the currently achievable resolution is not sufficient to state this beyond reasonable doubt and the results are to some extent open to alternative interpretations (Haugen et al., 2004; Subramanian et al., 2006). What seems to be clear is that the magnetic field has a tendency to organise itself in long filamentary structures ("folds") with field-direction reversals on very small scales (Schekochihin et al., 2004; Brandenburg & Subramanian, 2005). Filamentary magnetic structures are, indeed, observed in galaxy clusters (Eilek & Owen, 2002; Clarke & Ensslin, 2006), although the field reversal scale does not appear to be nearly as small as implied by MHD turbulence simulations—a theoretical puzzle solving which will probably require bringing in kinetic physics (see discussion in Schekochihin & Cowley, 2006).

It is clear that both the current and future theoretical debates on the structure of magnetic turbulence would benefit greatly from being constrained observationally in a rigorous way. For the reasons explained above, in order to do this, we must be able to diagnose nontrivial spatial structure, which cannot be done by looking at the magnetic power spectrum alone. Let us explain this in more detail.

Consider a divergence-free, helicity-free, statistically homogeneous and isotropic field as a minimal model for the fluctuating component of the magnetic field in galaxies and clusters. If this field also obeyed Gaussian statistics exactly or, at least, approximately, its power spectrum would be sufficient to completely describe its statistical properties because all higher-order multi-point statistics could be expressed in terms of the second-order two-point correlators and, therefore, the power spectrum. Assuming such Gaussian statistics, Spangler (1982, 1983) and Eilek (1989a) proposed to calculate the magnetic power spectrum using the observed total and polarised synchrotron radiation intensity, quantified by the Stokes parameters I, Q and U (see Appendix A.1). Computing two-point correlation functions of the Stokes parameters, henceforth referred to as Stokes correlators, one essentially obtains two-point, 4th-order correlation functions of the magnetic field in the plane perpendicular to the line of sight (Sect. 2.4.4). If the statistics are Gaussian or if Gaussianity is adopted as a closure assumption, the 4th-order correlators can be split into second-order correlators, so the power spectrum follows.

The problem with this approach to magnetic turbulence is that the Gaussian closure essentially assumes a structureless random-phased magnetic field, which then is, indeed, fully characterised by its power spectrum. It is evident in Eq. 2.2 that all phase information, which could tell us about the field structure, is lost in the power spectrum. As we explained above, both numerical and observational evidence (and, indeed, intuitive reasoning; see Schekochihin et al. 2004; Schekochihin & Cowley 2005) show that magnetic fields do have structure and are very far from being a collection of Gaussian random-phased waves. Their spectra tell us little about this structure. This rather simple point is illustrated in Fig. 2.1: the right panel depicts an instantaneous cross section of a 3D magnetic field obtained in a typical MHD dynamo simulation taken from Schekochihin et al. (2004), while the left panel shows a synthetically generated divergence-free Gaussian random field with exactly the same power spectrum (shown in Fig. 2.2, left panel). The folded structure discussed above is manifest in the simulated field but absent in the Gaussian one: in the former case, the field typically varies across itself on a much shorter scale than along itself and the regions of strongest bending are well localised, whereas in the latter case, the field is uniformly tangled and has similar variation along and across itself.

So how can one differentiate between such different fields in a systematic and quantitative way (i.e., other than by simply looking at visualisations)? As was pointed out by Schekochihin et al. (2002, 2004), this can be done by looking at the statistics of the tension force

$$\vec{F} = \frac{\vec{B} \cdot \vec{\nabla} \vec{B}}{4\pi}. \tag{2.3}$$

As a formal diagnostic, the tension force is a measure not just of the field strength but also of the gradient of the field along itself, thus it is strong if a field line is curved, and weak if the field line is mostly straight. The tension-force field associated with a folded magnetic field

(strong, straight direction-alternating fields in the "folds", weak curved fields in the "bends") will obviously be very different from the one associated with a random Gaussian field. As shown in Fig. 2.2 (right panel), their power spectra

$$T(k) = 4\pi k^2 \langle |\vec{F}(\vec{k})|^2 \rangle \tag{2.4}$$

do, indeed, turn out to be very different: flat for the folded field, peaked at the smallest scales for the Gaussian field. Why a flat tension-force spectrum is expected for a folded field is discussed in Schekochihin et al. 2004, their § 3.2.2, where numerical measurements of the tension-force statistics can also be found. In contrast, for the Gaussian field, one obviously gets $T(k) \propto k^2 M^2$, hence the peak at the small scales.

In physical terms, the tension force is one of the two components of the Lorentz force

$$\frac{1}{c}\,\vec{J} \times \vec{B} = -\vec{\nabla}\frac{B^2}{8\pi} + \frac{\vec{B}\cdot\vec{\nabla}\vec{B}}{4\pi}, \tag{2.5}$$

where the first term on the right-hand side is the magnetic pressure force, and the second term is the magnetic tension force, as defined in Eq. 2.3. In subsonic turbulence, the tension force essentially determines the dynamical back reaction of the magnetic field on the plasma motions because regions with higher magnetic pressure can be expected to have correspondingly weaker thermal pressure, so that the magnetic pressure forces are mostly balanced by oppositely directed thermal pressure forces.

Thus, measuring tension-force power spectra not only permits one to discriminate quantitatively between different magnetic turbulence scenarios but also provides a detailed insight into the MHD physics occurring in space, because it quantifies the properties of the dynamically relevant force in the magnetic turbulence. It is perhaps worth stressing this last point. In principle, many 4th-order statistical quantities that one might construct out of the Stokes correlators should be able to discern between different magnetic-field structures, but the tension-force power spectrum also has a clear physical meaning.

It is a stroke of luck that not only the tension-force power spectrum is the diagnostic that we would ideally like to know from the theoretical point of view, but it turns out that, under mild simplifying assumptions, it can be fully recovered from the statistical information contained in the Stokes correlators and, therefore, it is observable! This will be demonstrated in detail in the following sections. Such an outcome is not automatic: other potentially interesting statistical quantities such as the magnetic-energy power spectrum or the magnetic pressure-force statistics are not so directly imprinted into the Stokes correlators and require further assumptions in order to be extractable from the same data.

2.4 Method

In this section, we outline a formal theoretical framework for converting polarised-emission observables into the physically interesting statistical characteristics of the magnetic field under a number of simplifying assumptions.

2.4.1 Magnetic Field

Let us assume some volume V of interstellar or intracluster plasma to be filled with a magnetic field $\vec{B}(\vec{x})$ and a magnetised relativistic electron population giving rise to the synchrotron emission we observe (Fig. 2.3). We use a Cartesian coordinate system (x, y, z), where z is the line of sight. The volume under consideration is assumed to have depth L in this direction. The magnetic field can be decomposed into two parts:

$$\vec{B} = \overline{\vec{B}} + \vec{b}, \tag{2.6}$$

where $\overline{\vec{B}} = \langle \vec{B} \rangle$ is the regular (mean) field throughout the volume under consideration and $\vec{b}$ is the fluctuating ("turbulent") field. The former is assumed to be known and the latter is what we aim to study. We will work out its various correlation functions and their relationship to observable quantities—this can be done both in position space and in Fourier space in largely analogous ways. The Fourier transform of the field is defined according to

$$\hat{\vec{b}}(\vec{k}) = \frac{1}{V} \int d^3\vec{x}\, e^{-i\vec{k}\cdot\vec{x}} \vec{b}(\vec{x}), \qquad \vec{b}(\vec{x}) = \sum_{\vec{k}} e^{i\vec{k}\cdot\vec{x}} \hat{\vec{b}}(\vec{k}), \tag{2.7}$$

where $\vec{x} = (x, y, z)$. In what follows we will drop the hats on the Fourier transformed quantities. Note that discrete and continuous wave-vector spaces are related via a simple mnemonic:

$$\sum_{\vec{k}} \Leftrightarrow \frac{V}{(2\pi)^3} \int d^3\vec{k}. \tag{2.8}$$

2.4.2 Assumptions: Homogeneity and Isotropy

We will make two key assumption about the fluctuating magnetic field: statistical homogeneity and isotropy. The first of these is not a serious restriction of generality as, essentially, we would like to calculate statistical information based on data from subvolumes within which system-size spatial variation of the bulk properties of the astrophysical plasma under consideration can be ignored. The second assumption, the isotropy, is more problematic because of the known property of magnetised turbulence to be strongly anisotropic with respect to the direction of the mean field, *provided the mean field is dynamically strong* (see discussion and exhaustive reference lists in Schekochihin & Cowley, 2005; Schekochihin et al., 2007). It will, therefore,

only be sensible to apply our method to astrophysical situations where the mean field is either absent or weak, i.e., $\overline{B}^2 \ll \langle|\vec{b}|^2\rangle$. This should be a very good approximation for the ICM and may also be reasonable in parts of the ISM (e.g., in the spiral arms; see Haverkorn et al., 2006a, 2008).

In what follows, we will first consider the case of $\overline{B} = 0$ and then provide a generalisation of our results to the case of a weak mean field (Sect. 2.4.7). In both cases, we will first show how far one can get without the isotropy assumption and then find that only assuming isotropy are we able to calculate the tension-force power spectrum. It will also turn out that, in the case of a non-zero weak mean field, additional information can be gleaned from polarised-emission data, including the power spectrum of the fluctuating field (normally not available without the Gaussian closure, as discussed in Sect. 2.3).

Physically, we might argue that a weak mean field does not modify the turbulent dynamics and, therefore, does not break the statistical isotropy of the small-scale turbulent field. Obviously, if the bulk of the magnetic energy turns out to reside above or at some characteristic scale l_B, the statistically isotropic fluctuating field at that scale will look like a (strong) mean field to fluctuations at scales smaller than l_B and assuming isotropy of those fluctuations will almost certainly be wrong. Thus, our method can only be expected to handle successfully magnetic fluctuations at scales larger than l_B. This, however, is sufficient to make the outcome interesting because the key question in the theoretical discussions about the nature of the cosmic magnetic turbulence referred to in Sect. 2.3 is precisely what determines l_B (is it the reversal scale of the folded fields? what is that scale?) and how diagnosing the spatial structure of the field at scales above l_B might help us answer this question.

Note that a field organised in folds or filaments, as in Fig. 2.1 (left panel), is statistically isotropic because, while the folds extend over long distances, their orientation is random.

2.4.3 Observables: Stokers Parameters

Our direct observable is the partially linearly polarised synchrotron emission of the relativistic electrons gyrating in the magnetic field. This emission is measured by radio telescopes in projection onto the sky in terms of the Stokes parameters I, Q and U. Let us briefly recapitulate the relevant physics.

We assume a relativistic electron population that is spatially homogeneous, has an isotropic pitch-angle distribution, and a power-law energy distribution:

$$N(\gamma)d\gamma = C\gamma^{-p}d\gamma, \tag{2.9}$$

where γ is the Lorentz factor and N the number of electrons per γ per unit volume. The observed emission will then be partially linearly polarised (Rybicki & Lightman, 1979) and, therefore, at any given observed (radio) frequency ν, it is fully characterised by the Stokes parameters I, Q and U as functions of the sky coordinate $\vec{x}_\perp = (x, y)$ (the spatial coordinate in the plane

perpendicular to the line of sight). This is explained in somewhat more detail in Appendix A.1.

We further assume $p = 3$ in Eq. 2.9 (corresponding to the frequency distribution $\propto \nu^{-1}$). This is a convenient choice because then all Stokes parameters are quadratic in the magnetic field, which means that their two-point correlation functions will give us 4th-order statistics. We stress that this power law, although expected by theoretical shock acceleration models (Drury, 1983), is, of course, a simplification of reality (see, e.g. Strong et al., 2007). However, it is usually a sufficiently good approximation over fairly wide frequency ranges for many synchrotron sources. Thus, $p = 3$ is reasonably close to the values observed for our own Galaxy (Reich & Reich, 1988a; Tateyama et al., 1986), the values obtained by CMB foreground subtraction techniques (e.g. Tegmark & Efstathiou, 1996; de Oliveira-Costa et al., 2008; Dunkley et al., 2008; Bottino et al., 2008), and found in extra-galactic observations of radio-galaxies (Beck et al., 1996). While the theoretical developments that follow do depend on taking $p = 3$, the numerical tests of the resulting method reported in Sect. 2.5.2 will show that it is not essential that $p = 3$ be satisfied particularly precisely. Deviations from $p = 3$ can be addressed analytically in a more quantitative way by a Taylor expansion around $p = 3$, which we leave for further work.

Finally, we assume the observed volume to be optically thin and its Faraday depth to be negligible at the observation frequency ν. At high frequencies, both conditions tend to be satisfied, Faraday rotation being in most cases the greater constraint. For example, in our Galaxy, Faraday rotation is a relevant phenomenon at frequencies below a few GHz, while the medium remains mostly optically thin down to frequencies of a few hundred MHz, where free-free absorption starts being relevant (see Sun et al., 2008, and references therein). In cases where Faraday rotation is present in the frequency range of the data, we assume that a Faraday de-rotation has been applied. Even in the case of source-intrinsic Faraday rotation, this can still be achieved using Faraday tomography techniques (Brentjens & de Bruyn, 2005).

Under these conditions the Stokes parameters can be written as the following line-of-sight integrals

$$\begin{aligned} I(\vec{x}_\perp) &= \frac{1}{L}\int_0^L dz \left[B_x^2(\vec{x}) + B_y^2(\vec{x})\right], \\ Q(\vec{x}_\perp) &= \frac{1}{L}\int_0^L dz \left[B_x^2(\vec{x}) - B_y^2(\vec{x})\right], \\ U(\vec{x}_\perp) &= \frac{1}{L}\int_0^L dz\, 2B_x(\vec{x})B_y(\vec{x}), \end{aligned} \tag{2.10}$$

where L is the depth of the emission region. The dimensional prefactors converting the magnetic-field strength to radio emissivity have been suppressed (see Appendix A.1).

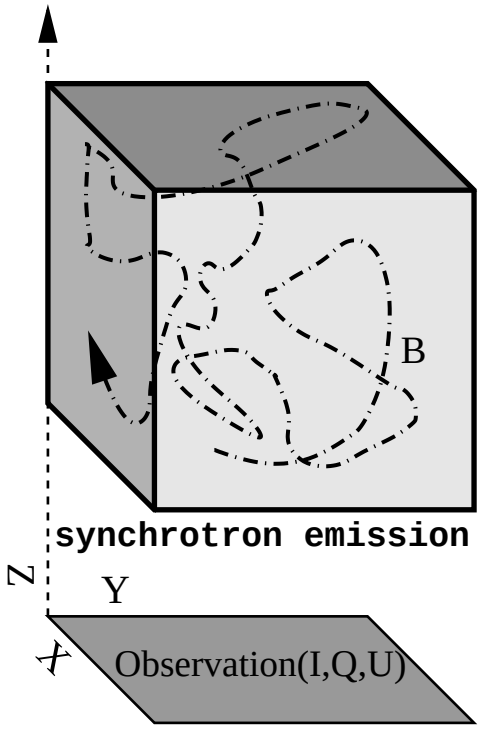

Figure 2.3: Magnetic field and the observables: artist's impression.

2.4.4 From Stokes Correlators to Magnetic-Field Statistics

Thus, observed polarised emission provides us with three scalar fields related quadratically to the magnetic field projected onto the plane perpendicular to the line of sight. We can construct 6 two-point correlators of these fields, which we will refer to as the Stokes correlators:

$$\Sigma_{XY}(\vec{r}_\perp) = \langle X(\vec{x}_\perp)\, Y(\vec{x}_\perp + \vec{r}_\perp)\rangle, \tag{2.11}$$

where $X, Y \in \{I, Q, U\}$ and $\langle ...\rangle$ denote a statistical average performed over the observational maps, which usually means volume averaging with respect to the sky coordinate $\vec{x}_\perp$.

Are the Stokes correlators sufficient to reconstruct the statistics of the magnetic field?

In formal terms, the statistical properties of a stochastic field are fully described by its n-point distribution function, or, equivalently, by the full set of its n-point, m-th order correlation tensors. In practice, this is too much information, most of it is not observable in any realistic situation, and in any event, only a few of these correlators can be interpreted in simple physical terms and are, therefore, useful for a qualitative understanding of the field structure. As the Stokes correlators are 4th order in the magnetic field and measure its correlations between two points in space, it is the two-point, 4th-order correlation tensor that will be relevant to this

discussion:

$$\begin{aligned} C_{ij,mn}(\vec{r}) &= \langle B_i(\vec{x})B_j(\vec{x})B_m(\vec{x}+\vec{r})B_n(\vec{x}+\vec{r})\rangle \\ &= \langle H_{ij}(\vec{x})H_{mn}(\vec{x}+\vec{r})\rangle, \end{aligned} \tag{2.12}$$

where, for notational convenience, we have introduced the field tensor $H_{ij} = B_i B_j$. The angle brackets denote statistical average, understood ideally as an ensemble (or time) average and in practice, if we are dealing with one observed realisation of the field, as the volume average: $\langle \ldots \rangle = (1/V) \int d^3\vec{x}(\ldots)$. Implicitly, performing a volume average relies on the assumption of statistical homogeneity (Sect. 2.4.2), i.e., independence of the statistical properties of the field of the reference point $\vec{x}$ where they are calculated. In terms of Fourier-space quantities, we have

$$C_{ij,mn}(\vec{r}) = \sum_{\vec{k}} e^{i\vec{k}\cdot\vec{r}} C_{ij,mn}(\vec{k}), \quad C_{ij,mn}(\vec{k}) = \langle H^*_{ij}(\vec{k})H_{mn}(\vec{k})\rangle, \tag{2.13}$$

where the Fourier transforms of all quantities are defined similarly to Eq. 2.7.

Let us write the Stokes correlators in terms of the correlation tensor $C_{ij,mn}$. It is particularly easy to do this in Fourier space because the line-of-sight integration in Eq. 2.10 amounts simply to picking the $k_z = 0$ component of the field:

$$\begin{aligned} I(\vec{k}_\perp) &= H_{xx}(\vec{k}_\perp) + H_{yy}(\vec{k}_\perp), \\ Q(\vec{k}_\perp) &= H_{xx}(\vec{k}_\perp) - H_{yy}(\vec{k}_\perp), \\ U(\vec{k}_\perp) &= 2H_{xy}(\vec{k}_\perp), \end{aligned} \tag{2.14}$$

where $\vec{k}_\perp = (k_x, k_y, 0)$. Therefore, the Fourier transforms of the Stokes correlators [Eq. 2.11] are

$$\begin{aligned} \Sigma_{II}(\vec{k}_\perp) &= C_{xx,xx}(\vec{k}_\perp) + C_{xx,yy}(\vec{k}_\perp) + C^*_{xx,yy}(\vec{k}_\perp) + C_{yy,yy}(\vec{k}_\perp), \\ \Sigma_{QQ}(\vec{k}_\perp) &= C_{xx,xx}(\vec{k}_\perp) - C_{xx,yy}(\vec{k}_\perp) - C^*_{xx,yy}(\vec{k}_\perp) + C_{yy,yy}(\vec{k}_\perp), \\ \Sigma_{UU}(\vec{k}_\perp) &= 4C_{xy,xy}(\vec{k}_\perp), \\ \Sigma_{IQ}(\vec{k}_\perp) &= C_{xx,xx}(\vec{k}_\perp) - C_{xx,yy}(\vec{k}_\perp) + C^*_{xx,yy}(\vec{k}_\perp) - C_{yy,yy}(\vec{k}_\perp), \\ \Sigma_{IU}(\vec{k}_\perp) &= 2\left[C_{xx,xy}(\vec{k}_\perp) + C_{yy,xy}(\vec{k}_\perp)\right], \\ \Sigma_{QU}(\vec{k}_\perp) &= 2\left[C_{xx,xy}(\vec{k}_\perp) - C_{yy,xy}(\vec{k}_\perp)\right]. \end{aligned} \tag{2.15}$$

This immediately implies that

$$\begin{aligned}
C_{xx,xx}(\vec{k}_\perp) &= \frac{1}{4}\left[\Sigma_{II}(\vec{k}_\perp) + \Sigma_{QQ}(\vec{k}_\perp) + 2\mathrm{Re}\,\Sigma_{IQ}(\vec{k}_\perp)\right], \\
C_{yy,yy}(\vec{k}_\perp) &= \frac{1}{4}\left[\Sigma_{II}(\vec{k}_\perp) + \Sigma_{QQ}(\vec{k}_\perp) - 2\mathrm{Re}\,\Sigma_{IQ}(\vec{k}_\perp)\right], \\
C_{xx,yy}(\vec{k}_\perp) &= \frac{1}{4}\left[\Sigma_{II}(\vec{k}_\perp) - \Sigma_{QQ}(\vec{k}_\perp) - i2\mathrm{Im}\,\Sigma_{IQ}(\vec{k}_\perp)\right], \\
C_{xy,xy}(\vec{k}_\perp) &= \frac{1}{4}\Sigma_{UU}(\vec{k}_\perp), \\
C_{xx,xy}(\vec{k}_\perp) &= \frac{1}{4}\left[\Sigma_{IU}(\vec{k}_\perp) + \Sigma_{QU}(\vec{k}_\perp)\right], \\
C_{yy,xy}(\vec{k}_\perp) &= \frac{1}{4}\left[\Sigma_{IU}(\vec{k}_\perp) - \Sigma_{QU}(\vec{k}_\perp)\right]. \qquad (2.16)
\end{aligned}$$

These are the only components of the correlation tensor Eq. 2.13 that are observable directly and it is only their dependence on the wave vector perpendicular to the line of sight that can be probed. No correlators that involve the projection of the field on the line of sight (B_z) can be known, which is a consequence of the fact that synchrotron observations probe only the perpendicular to the line-of-sight magnetic field component.

2.4.5 The consequences of isotropy on correlation functions

We have already made implicit use of the assumption of homogeneity when computing the ensemble average of the 4th-order correlation tensor by performing a volume average. In this section we will explore the consequences of the isotropic magnetic field assumption (Sect. 2.4.2) on correlation functions by making use of a mathematical technique called the "invariant theory of isotropic tensors" (Robertson, 1940), and can be used in a number of different physical fields. Assuming isotropy it tells us how to write a correlation function of any order in the most compact form possible. In other words, the information content of a correlation function.

Here we present only the concepts of that theory for the simple case of a second order correlation function, while we leave the cumbersome computations for 3th- 4th-order correlation functions required for our specific computations to the App. A, although the necessary steps for the generalisation of the technique are presented at the end of the section.

The information content of a second order correlation function

It is more intuitive to start the derivation in real space. We consider a second order correlation function of some statistically homogeneous vector field $\vec{b}$,

$$c_{i,j}(\vec{r}) = \langle b_i(\vec{x}) b_j(\vec{x}') \rangle \,. \qquad (2.17)$$

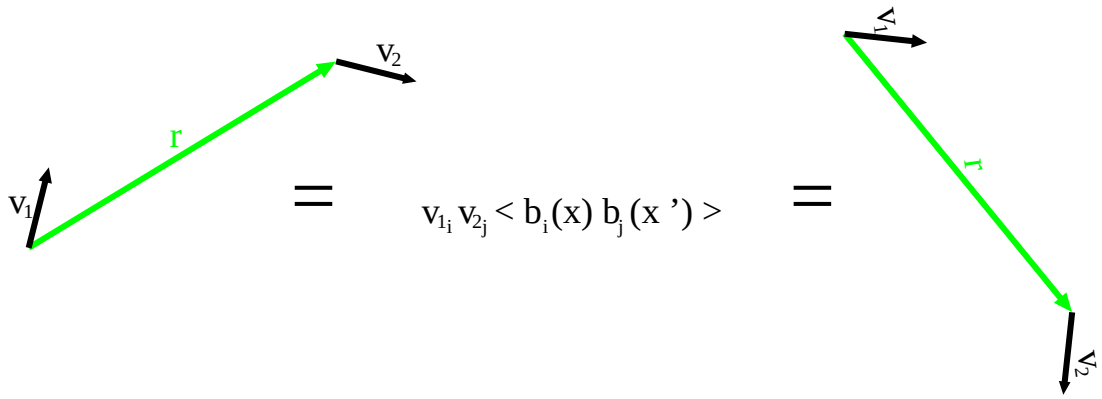

Figure 2.4: If the vector field $\vec{b}$ is isotropic, the correlation function in Eq. 2.18 is only dependent on the magnitude of $\vec{r}$ and the relative orientation of $\vec{r}$, $\vec{v}_1$ and $\vec{v}_2$.

Here, $\vec{r} = \vec{x}' - \vec{x}$, and the lower case $c_{i,j}$ specifies that we are considering only the fluctuating part of the field, i.e. $\overline{\vec{B}} = 0$ (see Eq. 2.6). If, however, we wish the correlation in some arbitrarily directed vector components we simply have

$$c(\vec{r}, \vec{v}_1, \vec{v}_2) = \vec{v_1}_i \vec{v_2}_j c_{i,j}(\vec{r}) = \vec{v_1}_i \vec{v_2}_j \langle b_i(\vec{x}) b_j(\vec{x}') \rangle \,, \tag{2.18}$$

where $\vec{v}_1$ and $\vec{v}_2$ are unit vectors.

Let us now assume isotropy. This means, as can readily be seen from Fig. 2.4, that the correlation function given in Eq. 2.18 depends only on the relative orientation of $\vec{v}_1$, $\vec{v}_2$, $\vec{r}$, and on the absolute magnitude of the latter. Furthermore, we know by construction (Eq. 2.18) that the correlation function $c(\vec{r}, \vec{v}_1, \vec{v}_2)$ is a bilinear function of $\vec{v}_1$ and $\vec{v}_2$.

The quantities that give us the relative orientations of our three vectors are thus the scalar products of the form $v_{1i} r_i$, $v_{2i} r_i$, $v_{1i} v_{2i}$ and the vector product $\epsilon_{ijp} v_{1i} v_{2j} r_p$. The bilinearity condition and the fact that the correlation function also depends on the absolute magnitude of $\vec{r}$ in an unknown form leaves us with

$$c_{i,j}(\vec{r}) \;=\; \tilde{m}_1(r)\delta_{ij} + \tilde{m}_2(r)\hat{r}_i\hat{r}_j + \tilde{m}_3(r)\epsilon_{ijp}\hat{r}_p \,, \tag{2.19}$$

where $\tilde{m}_i$ are unknown independent functions of r, and $\hat{r}_i = r_i/r$. This is as good as it gets, we have, assuming isotropy, reduced the correlation function to the minimum necessary information of three scalar functions which depend only on the distance r, not its direction.

The scalar functions the correlation function depends on can sometimes be interpreted as physically significant quantities. We will demonstrate that by pursuing our example a bit further, and taking it into Fourier space,

$$c_{i,j}(\vec{k}) \;=\; \langle b_i^*(\vec{k}) b_j(\vec{k}) \rangle \,,$$

and

$$c(\vec{k}, \vec{v}_1, \vec{v}_2) \quad = \quad v_{1\,i} v_{2\,j} c_{i,j}(\vec{k}) \,.$$

Though statistical homogeneity no longer holds in Fourier space, isotropy does, since the Fourier transform does not add any preferred direction into the problem. This implies that the correlation function $c(\vec{k}, \vec{v}_1, \vec{v}_2)$ will depend on the relative orientation of the wave vector $\vec{k}$ to $\vec{v}_1$ and $\vec{v}_2$ as well as on the absolute magnitude of $\vec{k}$.

Similarly to Eq. 2.19, we can therefore write

$$c_{i,j}(\vec{k}) \quad = \quad m_1 \delta_{ij} + m_2 \hat{k}_i \hat{k}_j + m_3 \epsilon_{ijp} \hat{k}_p \,. \tag{2.20}$$

Here m_i are unknown independent functions of k (and, we stress, not Fourier pairs of the m_i functions in real space), while $\hat{k}_i = k_i/k$.

Let us now say that the field $\vec{b}$ is also divergence-free. This means that $k_i b_i(\vec{k}) = 0$. Applying this to Eq. 2.20 we obtain $m_2 = -m_1$. We renormalise $m_1 \to m_1/2$ so that it is in accord with the form of Eq. 2.2 and Eq. A.15, where it is identified as the magnetic power spectrum. Finally we redefine $m_3 \to i m_3$, so that all m_i functions are real. We are then left with the final form

$$c_{i,m}(\vec{k}) \quad = \quad \frac{m_1}{2}(\delta_{im} - \hat{k}_i \hat{k}_m) + i\, m_3\, \epsilon_{imp}\, \hat{k}_p \,. \tag{2.21}$$

As the reader can verify, $m_1(k) = c_{i,i}(\vec{k})$ is actually the power spectrum of the field $\vec{b}$ (in accord with Eq. A.15 and Eq. 2.2). Furthermore, $m_3(k)$ is the helicity spectrum. We note that this identification with known physical quantities of the m_i functions is not always possible, as is the case e.g. in higher order correlation functions (see App. A.2).

Higher order correlation functions

The same reasoning applied in the previous section to a second order correlation function can also be applied to correlation functions of any order. We write

$$c(\vec{r}_1, \cdots, \vec{r}_N; \vec{v}_1, \cdots, \vec{v}_M) = \vec{v}_1 \cdots \vec{v}_M \, c_{i,j,\cdots,m,n}(\vec{r}_1, \cdots, \vec{r}_N) \,, \tag{2.22}$$

where

$$c_{i,j,\cdots,m,n}(\vec{r}_1, \cdots, \vec{r}_N) = \langle b_i(\vec{x})\, b_j(\vec{x} + \vec{r}_1) \cdots b_m(\vec{x} + \vec{r}_{N-1})\, b_n(\vec{x} + \vec{r}_N) \rangle \,. \tag{2.23}$$

Again, we know the correlation function will be M-linear in $\vec{v}_1, \cdots, \vec{v}_M$, and the relative orientation of $\vec{v}_1, \cdots, \vec{v}_M$ and $\vec{r}_1, \cdots, \vec{r}_N$ is given by scalar products of them, or scalar products of their vector products (there are simply no further options). Reducing the correlation function in Eq. 2.22 to its most compact form simply requires assuring that no redundancies are

left in the combination of the scalar products, or scalar products of vector products (see e.g. Appendix A.2.1).

Applying the invariant theory of isotropic tensors to $C_{ij,mn}$, it turns out, if no mean field is present ($\overline{B} = 0$), we only need to know seven independent scalar functions of $k = |\vec{k}|$ to reconstruct $C_{ij,mn}$ fully (see Eq. A.28 in Appendix A.2.1). It also turns out that only four of the Stokes correlators of an isotropic field contain independent information: Σ_{II}, two of Σ_{QQ}, Σ_{UU}, Σ_{QU} and one of Σ_{IQ}, Σ_{IU}. For example, if we keep Σ_{II}, Σ_{QQ}, Σ_{UU} and Σ_{IQ}, the other two Stokes correlators are

$$\begin{aligned} \Sigma_{IU} &= \Sigma_{IQ} \tan 2\varphi, \\ \Sigma_{QU} &= \frac{1}{2}(\Sigma_{QQ} - \Sigma_{UU}) \tan 4\varphi, \end{aligned} \tag{2.24}$$

where φ is the angle between $\vec{k}_\perp$ and the x axis of the frame in which the Stokes parameters are measured, i.e., $\vec{k}_\perp = k_\perp(\cos\varphi, \sin\varphi, 0)$. These relations are useful in constructing well behaved expressions for the observables (see Sect. 2.4.6 and Appendix A.2.2). They could also be useful in practical situations when the Stokes maps might not be perfect, so one might have more (or higher-quality) data on some Stokes correlators than on others.

We see that even with isotropy we do not have enough observables to measure the general 4th-order statistics of the magnetic field (seven independent scalar functions needed, four available). However, the information carried by the Stokes correlators does suffice to reconstruct some of the correlation functions of the field. How to determine whether any particular 4th-order correlator is observable is explained in Appendix A.2.2. Luckily, we find that we can reconstruct the tension-force power spectrum, which is a physically interesting quantity because it diagnoses the geometrical structure of the magnetic field and its dynamical action on the plasma motions (Sect. 2.3). Although its derivation follows from the general procedure given in Appendix A.2.2 (see Appendix A.2.2), it is perhaps illuminating to provide an individual derivation for this quantity.

2.4.6 Tension-Force Power Spectrum

The tension force [Eq. 2.3] is $F_i = B_j \partial_j B_i = \partial_j H_{ij}$, where we have omitted the factor of $1/4\pi$). Therefore, its spectrum [Eq. 2.4] is

$$T(k) = 4\pi k^2 \Phi(k), \tag{2.25}$$

where

$$\Phi(k) = \langle F_i^*(\vec{k}) F_i(\vec{k}) \rangle = k_j k_n C_{ij,in}(\vec{k}). \tag{2.26}$$

We do not have any directly observable information about $k_z \neq 0$, so let us set $\vec{k} = \vec{k}_\perp = k_\perp(\cos\varphi, \sin\varphi, 0)$. Then

$$\Phi(k_\perp) = \Phi_1 + \Phi_2, \tag{2.27}$$

where Φ_1 is the part that is directly recoverable from the Stokes correlators [using Eq. 2.16]:

$$\begin{aligned}\Phi_1 &= k_x^2\left[C_{xx,xx}(\vec{k}_\perp) + C_{xy,xy}(\vec{k}_\perp)\right] + k_y^2\left[C_{xy,xy}(\vec{k}_\perp) + C_{yy,yy}(\vec{k}_\perp)\right] \\ &\quad + 2k_xk_y\mathrm{Re}\left[C_{xx,xy}(\vec{k}_\perp) + C^*_{yy,xy}(\vec{k}_\perp)\right] \\ &= \frac{1}{4}k^2\left[\Sigma_{II} + \Sigma_{QQ} + \Sigma_{UU} + 2\mathrm{Re}\left(\Sigma_{IQ}\cos 2\varphi + \Sigma_{IU}\sin 2\varphi\right)\right],\end{aligned} \tag{2.28}$$

whereas Φ_2 is the part that contains magnetic-field components parallel to the line of sight and, therefore, not picked up by the polarised-emission observations:

$$\Phi_2 = k_x^2 C_{xz,xz}(\vec{k}_\perp) + k_y^2 C_{yz,yz}(\vec{k}_\perp) + 2k_xk_y\mathrm{Re}C_{xz,yz}(\vec{k}_\perp). \tag{2.29}$$

It is to reconstruct this missing information that we have to assume isotropy, because it gives us a symmetry relationship between the unobservable correlators and the observable ones. If no mean field is present ($\overline{B} = 0$), it is possible to show (see Appendix A.2.2) that, for a statistically isotropic magnetic-field distribution,

$$\begin{aligned}\Phi_2 &= k^2\left\{C_{xy,xy}(\vec{k}_\perp) - \frac{k_xk_y}{k_x^2 - k_y^2}\left[C_{xx,xy}(\vec{k}_\perp) - C_{yy,xy}(\vec{k}_\perp)\right]\right\} \\ &= \frac{1}{4}k^2\left(\Sigma_{UU} - \Sigma_{QU}\tan 2\varphi\right).\end{aligned} \tag{2.30}$$

Assembling the directly observable [Eq. 2.28] and the inferred [Eq. 2.30] part of the tension-force power spectrum, we arrive at an expression for $\Phi(k)$ solely in terms of the Stokes correlators. There are two further steps that need to be taken to bring this expression into a practically computable form.

Firstly, let us recall that, while the Stokes correlators in Eq. 2.28 and Eq. 2.30 depend on the vector $\vec{k}_\perp$, the tension-force spectrum Φ must depend only on $k = |\vec{k}_\perp|$. It is, therefore, permissible (and, in fact, increases the quality of the statistics) to average our expression for Φ over the angle φ (i.e., over a shell $|\vec{k}_\perp| = k$ in the wavenumber space).

Secondly, the fact that, for an isotropic field, only 4 of the 6 available Stokes correlators are independent [see Eq. 2.24] can be used to construct many theoretically equivalent expressions for $\Phi(k)$. Additional freedom comes from the angle independence of $\Phi(k)$ and, therefore, the possibility of doing weighted angle averages (see Appendix A.2.2). The strategy for choosing a particular formula for practical computations is to avoid having singularities in the

coefficients: such as the factor of $\tan 2\varphi$ in Eq. 2.30. How to do this systematically is explained in Appendix A.2.2, but here we simply give the result:

$$T(k)=\frac{1}{2}\,k^4\int_0^{2\pi}d\varphi\Big[\Sigma_{II}+2\left(\Sigma_{IQ}\cos 2\varphi+\Sigma_{IU}\sin 2\varphi\right)-\Sigma_{QU}\sin 4\varphi \\ +\frac{1}{2}\left(3-\cos 4\varphi\right)\Sigma_{QQ}+\frac{1}{2}\left(3+\cos 4\varphi\right)\Sigma_{UU}\Big]. \tag{2.31}$$

This formula is derived in Appendix A.2.2 from our general method, but can also be easily seen to follow directly from Eq. 2.28 and Eq. 2.30 via Eq. 2.24, angle averaging and multiplication by the wave-number-space volume factor of $4\pi k^2$ [see definition of $T(k)$, Eq. 2.25]. Eq. 2.31 is our final expression for the tension-force power spectrum.

Thus, we have accomplished our goal of showing that, despite the scarcity of the observable information, the tension-force power spectrum can be fully reconstructed from the available Stokes correlators (in Appendix A.2.2, we also show how to construct all other observable 4th-order quantities). In Sect. 2.5, we will test our method of doing this, but first, we generalise it slightly to the case of weak mean field.

2.4.7 Case of Weak Mean Field: Observing the Magnetic-Field Power Spectrum

We now relax the assumption that $\overline{\vec{B}}=0$ in Eq. 2.6. Then the 4th-order correlation tensor $C_{ij,mn}$ [Eq. 2.12] can be written in terms of the mean field and of the correlation tensors of the fluctuating field:

$$\begin{aligned} C_{ij,mn}(\vec{r}) \;=\;& \overline{B}_i\overline{B}_j\overline{B}_m\overline{B}_n+\overline{B}_i\overline{B}_j\langle b'_m b'_n\rangle+\overline{B}_m\overline{B}_n\langle b_i b_j\rangle \\ &+\overline{B}_i\overline{B}_m\langle b_j b'_n\rangle+\overline{B}_i\overline{B}_n\langle b_j b'_m\rangle \\ &+\overline{B}_j\overline{B}_m\langle b_i b'_n\rangle+\overline{B}_j\overline{B}_n\langle b_j b'_m\rangle \\ &+\overline{B}_i\langle b_j b'_m b'_n\rangle+\overline{B}_j\langle b_i b'_m b'_n\rangle \\ &+\overline{B}_m\langle b_i b_j b'_n\rangle+\overline{B}_n\langle b_i b_j b'_m\rangle \\ &+\langle b_i b_j b'_m b'_n\rangle, \end{aligned} \tag{2.32}$$

where unprimed quantities are evaluated at $\vec{x}$ and the primed ones at $\vec{x}+\vec{r}$. Due to homogeneity, correlation tensors depend only on $\vec{r}$ and not on $\vec{x}$ (and the statistical average can be interpreted as a volume average over $\vec{x}$). This means that the first three terms in Eq. 2.32 have no spatial

dependence at all, while the rest of the tensor can be written in Fourier space as follows:

$$\begin{aligned} C_{ij,mn}(\vec{k}) &= \frac{1}{V}\int d^3\vec{r}\, e^{-i\vec{k}\cdot\vec{r}} C_{ij,mn}(\vec{r}) \\ &= \overline{B}_i\overline{B}_m c_{j,n}(\vec{k}) + \overline{B}_i\overline{B}_n c_{j,m}(\vec{k}) \\ &\quad + \overline{B}_j\overline{B}_m c_{i,n}(\vec{k}) + \overline{B}_j\overline{B}_n c_{i,m}(\vec{k}) \\ &\quad + \overline{B}_i c^*_{mn,j}(\vec{k}) + \overline{B}_j c^*_{mn,i}(\vec{k}) \\ &\quad + \overline{B}_m c_{ij,n}(\vec{k}) + \overline{B}_n c_{ij,m}(\vec{k}) \\ &\quad + c_{ij,mn}(\vec{k}). \end{aligned} \tag{2.33}$$

This is the Fourier-space correlation tensor introduced in Eq. 2.13, which has now been expressed in terms of the mean field and the second-, 3rd- and 4th-order correlation tensors of the fluctuating field:

$$c_{i,m}(\vec{k}) = \langle b^*_i(\vec{k}) b_m(\vec{k})\rangle = \frac{1}{V}\int d^3\vec{r}\, e^{-i\vec{k}\cdot\vec{r}}\langle b_i b'_m\rangle, \tag{2.34}$$

$$c_{ij,m}(\vec{k}) = \langle h^*_{ij}(\vec{k}) b_m(\vec{k})\rangle = \frac{1}{V}\int d^3\vec{r}\, e^{-i\vec{k}\cdot\vec{r}}\langle b_i b_j b'_m\rangle, \tag{2.35}$$

$$c_{ij,mn}(\vec{k}) = \langle h^*_{ij}(\vec{k}) h_{mn}(\vec{k})\rangle, = \frac{1}{V}\int d^3\vec{r}\, e^{-i\vec{k}\cdot\vec{r}}\langle b_i b_j b'_m b'_n\rangle, \tag{2.36}$$

where $h_{ij}(\vec{k}) = (1/V)\int d^3\vec{x}\, e^{-i\vec{k}\cdot\vec{x}} b_i(\vec{x}) b_j(\vec{x})$.

Thus, the presence of the mean field leads to second- and 3rd-order statistics of the fluctuating field appearing alongside the 4th-order ones in the tensor $C_{ij,mn}$. Since the Stokes correlators probe the total field, this means that some information about the second- and 3rd-order statistics could be extracted from them, provided the mean field itself can be independently determined and thus used as a "probe" (in fact, it turns out that only its orientation generally has to be known and even that knowledge is not always necessary, although easily obtainable; see Appendix A.2.3).

As before, we need additional symmetry assumptions about the fluctuating field in order to make a transition from the Stokes correlators to theoretically/physically interesting quantities. The technically rigorous choice would be to assume that the statistics of $\vec{b}$ will depend on one special direction, that of the mean field, and be isotropic in the plane perpendicular to it. This, however, leads to a very large number of independent scalar functions appearing in the general form of $C_{ij,mn}$ and while it is probably worth working them all out, it is quite unlikely that the 6 available Stokes correlators will be sufficient to reconstruct anything of value. Therefore, we make a simplifying assumption (the physical grounds for which are discussed in Sect. 2.4.2) that the mean field is so weak ($\overline{B}^2 \ll \langle b^2\rangle$) that the fluctuating field remains statistically isotropic. Under this assumption, the case of a weak mean field becomes a straightforward generalisation of the zero-mean-field case considered above. The main gain is that a weak mean field allows

us to use the Stokes correlators to determine not just the power spectrum of the tension force but also the power spectrum of the magnetic field itself: as $M(k) = 4\pi k^2 c_{i,i}$ [Eq. 2.2], it is recovered from the second-order terms in Eq. 2.33.

The mathematical details of reconstructing the magnetic-field power spectrum are relegated to Appendix A.2.3. There are many equivalent expressions that can be derived for it; here we display three of them:

$$\begin{aligned} M(k) &= \frac{2k^2}{\overline{B}_\perp^2 \cos 2\Theta} \int_0^{2\pi} d\varphi \, \mathrm{Re}\Sigma_{IQ} \\ &= \frac{2k^2}{\overline{B}_\perp^2 \sin 2\Theta} \int_0^{2\pi} d\varphi \, \mathrm{Re}\Sigma_{IU} \\ &= \frac{k^2}{2\overline{B}_\perp^2 \sin 2\Theta} \int_0^{2\pi} d\varphi \, (\Sigma_{QQ} - \Sigma_{UU}), \end{aligned} \tag{2.37}$$

where Θ is the angle between the x axis and the projection of the mean field onto the plane perpendicular to the line of sight, $\overline{B}_\perp$ is the magnitude of this perpendicular projection. Although these are easy to measure (Appendix A.2.3), they are manifestly not necessary to determine the functional shape of the spectrum. Thus, we have three independent expressions from which we can deduce this functional shape. That the results should be consistent with one another is a good test of our assumptions (most importantly, the statistical isotropy of the fluctuating part of the field).

The calculation of the tension-force power spectrum is entirely analogous to the zero-mean-field case (see Appendix A.2.3). The result is that Eq. 2.31 still holds subject to two modifications: real part has to be taken of all Stokes correlators and a term proportional to $M(k)$ has to be subtracted, namely

$$T_{\overline{B}\neq 0}(k) = \mathrm{Re}T_{\overline{B}=0}(k) - \frac{1}{8} k^2 \overline{B}_\perp^2 M(k), \tag{2.38}$$

where $T_{\overline{B}=0}(k)$ is given by Eq. 2.31.

Finally, a disclaimer is in order with regard to the practical applicability of the results obtained for the case of a weak mean field. Since we assumed the mean field to be small compared to the fluctuating field, $\overline{B}^2 \ll \langle b^2 \rangle$, the terms in Eq. 2.32 that contain $\overline{B}_i$ are small compared to $\langle b_i b_j b'_m b'_n \rangle$. Thus, in order for the second-order statistical information in Eq. 2.32 to be recoverable, the errors associated with the imperfect isotropy of the fluctuating field must be very small—smaller than $O(\overline{B}^2)$. It is not guaranteed that this is either justified physically or achievable in practice and the verdict on the usefulness of the results of this section will depend on extensive numerical tests, which will not be undertaken in this paper and are left for future work.

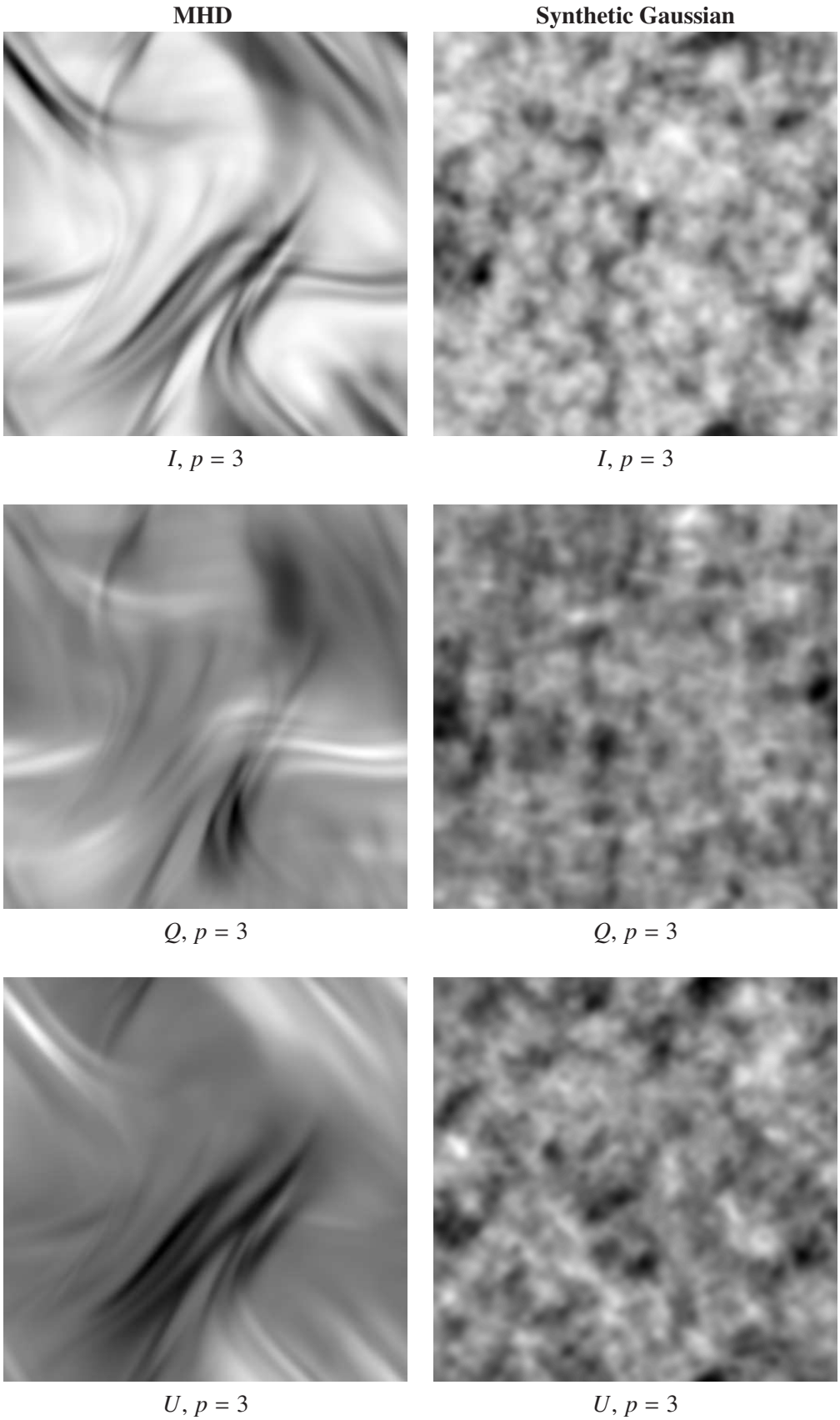

Figure 2.5: Examples of synthetic I, Q and U maps generated from an MHD-simulated magnetic field (*left panels*) and a synthetic Gaussian field (*right panels*). The same data cubes were used as in Fig. 2.1.

Figure 2.6: *Left panel:* The bold solid red line shows the tension-force power spectrum reconstructed via Eq. 2.31 from the synthetic Stokes maps (Fig. 2.5) based on an MHD-simulated field (saturated state of the Run S4 of Schekochihin et al., 2004). The bold dotted black line is the same spectrum computed directly from the full three-dimensional data (same as Fig. 2.2, right panel). The errors bars on the estimated spectrum are obtained by comparing results from synthetic Stokes maps obtained by integrating along three orthogonal "lines of sight" (the three axes of the data cube). The thin solid blue line with error bars and the thin dotted black line represent analogous information for a synthetic Gaussian field. *Right panel:* Similar to the left panel, but the reconstructed tension-force spectra are based not on the estimate Eq. 2.31 but on the full information about the projected (line-of-sight integrated) spectra, i.e., they are given by the sum of Φ_1 [Eq. 2.28] and $\Phi 2$ [Eq. 2.29] calculated in terms of $C_{ij,mn}(\vec{k}_\perp)$ (including its unobservable line-of-sight components).

2.5 Numerical Tests

Having presented the analytical derivation of our method, we now present a proof-of-concept numerical test by analysing two data cubes containing randomly tangled magnetic fields: a saturated magnetic field generated by fluctuation dynamo in an MHD simulation (Run S4 of Schekochihin et al. 2004) and a divergence-free, random-phased Gaussian field synthetically generated to have the same spectrum as the MHD field (Fig. 2.2; snapshots of the two fields are shown in Fig. 2.1). Both fields have zero mean, so the results of Sect. 2.4.7 are not tested here.

2.5.1 Case of $p = 3$

We first test the validity of our method for the case of the electron spectral index $p = 3$, assumed throughout the analytical developments presented above. For each data cube, we designate one of its axes as the "line of sight" and integrate the field along it according to Eq. 2.10. This produces three synthetic two-dimensional Stokes maps (Fig. 2.3; examples of such I, Q and U maps are shown in Fig. 2.5). Since we have the full three-dimensional information for both fields, we can compute the tension-force power spectra directly and then compare them to the spectra obtained by applying our estimator, Eq. 2.31, to the synthetic Stokes maps.

In Fig. 2.6 (left panel) we plot the tension-force power spectra reconstructed using our estimator, Eq. 2.31, for a realisation of an MHD simulated field and for a synthetic Gaussian

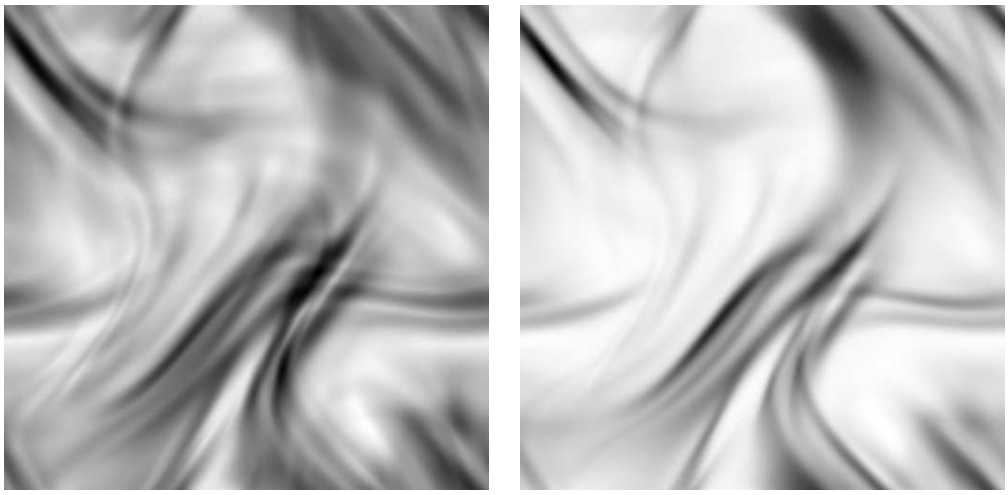

I, $p = 1.5$ I, $p = 4.5$

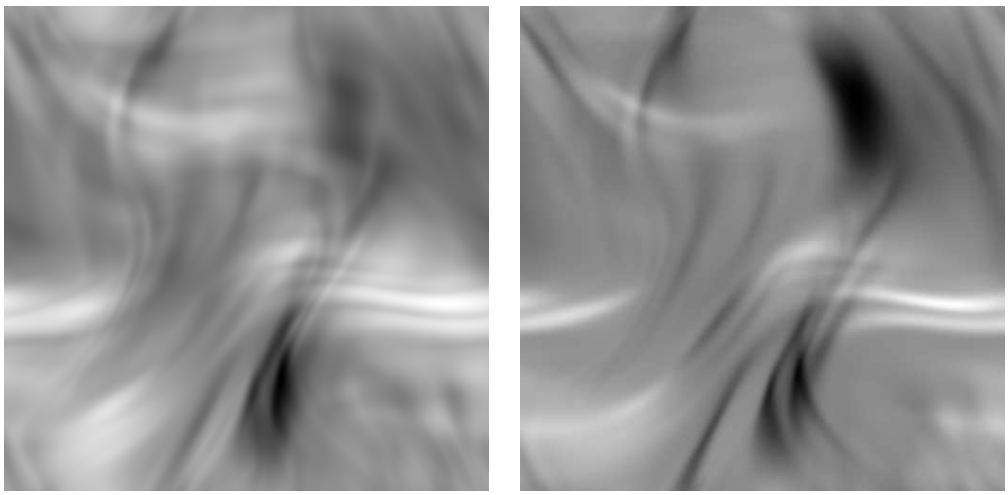

Q, $p = 1.5$ Q, $p = 4.5$

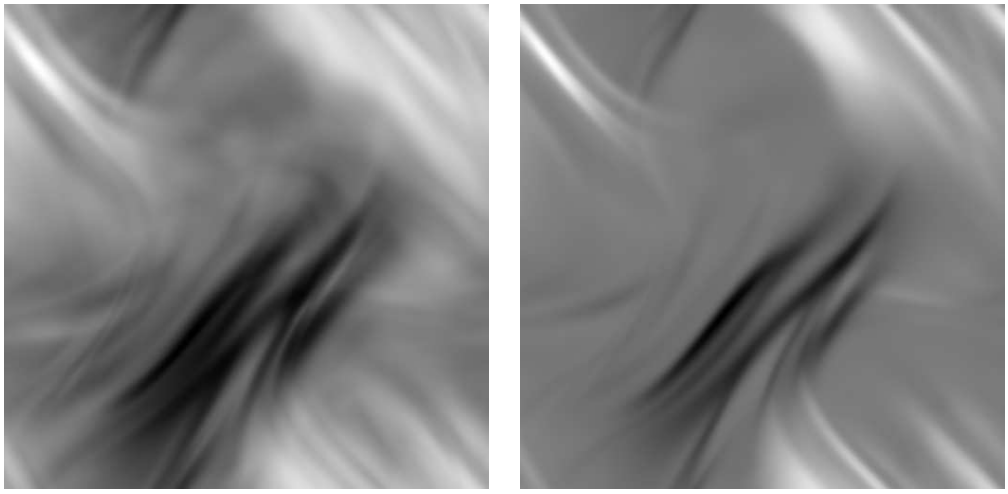

U, $p = 1.5$ U, $p = 4.5$

Figure 2.7: The Stokes maps calculated according to Eq. 2.39 for two extreme values of the electron spectral index, $p = 1.5$ (*left panels*) and $p = 4.5$ (*right panels*). These are to be compared with the Stokes maps for $p = 3$ shown in the left panel of Fig. 2.5.

field. They are compared to the same spectra directly computed from the three-dimensional data cubes [according to Eq. 2.4]. The reconstructed spectra are obtained as an average over three synthetic Stokes maps, each obtained by choosing as the "line of sight" one of the three orthogonal axes of the data cube. This allows us to estimate the accuracy of the reconstruction, represented in Fig. 2.6 by the error bars.

For both types of field, the performance of our estimator is clearly excellent. The relative error bars for the Gaussian random field are substantially smaller than for the MHD field, which makes sense in view of the former's more small-scale and less structured character. The salient point that emerges from the comparison of the two fields is that the tension-force spectrum can be recovered from the synthetic observations with an accuracy easily permitting to discriminate between the structured (folded) MHD field and the structureless Gaussian one. This suggests that the proposed estimator is a robust tool for diagnosing magnetic turbulence from polarised emission data and for discriminating between different scenarios of magnetic-field evolution and saturation (see discussion in Sect. 2.3).

The test that we have presented only allows us to assess the quality of our method under idealised conditions, namely, assuming that the observation is noiseless, that no observational-window effects are present, that the relativistic-electron energy distribution is homogeneous and has the spectral index $p = 3$, and that the Faraday rotation is either negligible or has been effectively subtracted (Sect. 2.4.3). Thus, the errors in our reconstructed spectra are due to two factors: firstly, a certain amount of information is lost in the projection of the three-dimensional data onto a two-dimensional Stokes map (the line-of-sight integration); secondly, the assumptions of statistical homogeneity and isotropy (Sect. 2.4.2), upon which our estimator depends, are imperfectly satisfied by any particular realisation of the field. It is interesting to ask what is the relative contribution of these two sources of inaccuracy to the errors of reconstruction represented by the error bars in the left panel of Fig. 2.6. This is addressed the right panel of the same figure, which is analogous to the left panel, but instead of the spectra reconstructed via Eq. 2.31, it shows the spectra resulting just from the line-of-sight integration (setting $k_z = 0$) of the full tensor $C_{ij,mn}$, i.e, they use the unobservable z components of this tensor that enter in Eq. 2.29 rather than infer them from the observable components and the isotropy assumption. Comparing the right and left panels of Fig. 2.6 suggests that much of the reconstruction error (especially at large wave numbers) is due to the loss of information associated with the line-of-sight integration, not to imperfect isotropy—and this is despite the fact that the MHD field contains magnetic structures with virtually box-size parallel coherence lengths (see the left panel of Fig. 2.1).

2.5.2 Case of $p \neq 3$

Assuming that the electron spectral index $p = 3$ was an idealisation of the real observational situation that we needed for the theoretical justification of our method because Stokes

Figure 2.8: These plots show the same comparisons as the left panel of Fig. 2.6, but for a number of values of the electron spectral index $p \neq 3$. The Stokes maps were calculated according to Eq. 2.39. Some of these Stokes maps are shown in Fig. 2.7.

parameters are strictly quadratic in the magnetic field only if $p = 3$ (see Appendix A.1). While $p = 3$ is not a bad approximation of reality, one cannot expect it to be satisfied very precisely (see discussion and references in Sect. 2.4.3), so in order for our method to be practically useful for real observations, it must be reasonably insensitive to the exact value of p. This sensitivity is very easy to test.

Let us generalise our definition of the Stokes parameters [Eq. 2.10] to the case of $p \neq 3$: suppressing the dimensional prefactors as before, we get (see Appendix A.1)

$$\begin{aligned} I(\vec{x}_\perp) &= \frac{1}{L}\int_0^L dz \left[B_x^2(\vec{x}) + B_y^2(\vec{x})\right]^{(p-3)/4} \left[B_x^2(\vec{x}) + B_y^2(\vec{x})\right], \\ Q(\vec{x}_\perp) &= \frac{1}{L}\int_0^L dz \left[B_x^2(\vec{x}) + B_y^2(\vec{x})\right]^{(p-3)/4} \left[B_x^2(\vec{x}) - B_y^2(\vec{x})\right], \\ U(\vec{x}_\perp) &= \frac{1}{L}\int_0^L dz \left[B_x^2(\vec{x}) + B_y^2(\vec{x})\right]^{(p-3)/4} 2B_x(\vec{x})B_y(\vec{x}). \end{aligned} \tag{2.39}$$

Clearly, for $p > 3$, the extra factor of $(B_x^2 + B_y^2)^{(p-3)/4}$ causes the statistics to be effectively weighted towards regions where the field is stronger, for $p < 3$, towards those where it is weaker. This point is illustrated by Fig. 2.7, which shows that increasing/decreasing p roughly corresponds to increasing/decreasing the contrast in the Stokes maps.

The range of values that p can realistically be expected to take is roughly $p \in [1.5, 3.5]$ (see references in Sect. 2.4.3). Since this implies that $(p-3)/4 \in [-0.375, 0.125]$ are not very large powers, there is *a priori* a hope that the effect of deviations from $p = 3$ might not be catastrophic for our estimator. This, indeed, proves to be correct. In Fig. 2.8, we show the tension-force spectra reconstructed from Stokes maps generated using Eq. 2.39 with a number of values of p and compare them to the true spectra. Even for values of p significantly different from 3 (roughly in the range $p \in [2.5, 3.5]$), our estimator works extremely well, except at the highest wave numbers.

Note that the extra factor of $(B_x^2 + B_y^2)^{(p-3)/4}$ in Eq. 2.39 changes the overall amplitude of the Stokes parameters in comparison to what it would have been with $p = 3$, so we can only hope to recover the functional shape of the tension-force power spectrum, not its overall magnitude. In the numerical data used above this potential source of reconstruction error is not very visible because values of the magnetic field are close to unity in code units, but in any realistic observational situation, the shift in amplitude of the Stokes parameters may be significant. Importantly, however, we see in Fig. 2.8 that in all cases we have tested, the shape of the reconstructed tension-force power spectrum still makes it unambiguously possible to discriminate between qualitatively different field structures as represented by the MHD and Gaussian fields.

The numerical tests presented above are meant to demonstrate in principle that the approach taken in this paper is a valid one. We did not attempt to test the robustness of our approach by

including into our synthetic data model all of the complications that will arise in handling real observational data. A known caveat is that observational window functions, due to the finite size of the radio source of the telescope beam, will lead to a redistribution of power in the recovered spectrum, so that the large-scale power may swamp the signal at high wave numbers (Vogt & Enßlin, 2003). Both further tests and applications of our method to real data are left to future work.

2.6 Chapter conclusion

We have demonstrated that it is possible to reconstruct the power spectrum of the tension force associated with tangled astrophysical magnetic fields as a linear combination of the radio synchrotron observables, the Stokes correlators. This was done under a set of simplifying assumptions about the synchrotron emission data (Sect. 2.4.3) and also by assuming a statistically homogeneous and isotropic stochastic magnetic field (Sect. 2.4.2). The tension-force power spectrum emerges as a particular case from a subset of observable 4th-order statistics (Sect. 2.4.6 and Appendix A.2.2)—a nontrivial fact because in general, the Stokes maps do not carry sufficient information to reconstruct all of the 4th-order correlators of the magnetic field (see Sect. 2.4.4 and Appendix A.2.2).

The observability of the tension-force power spectrum is a stroke of good fortune because this quantity plays an important role in diagnosing the spatial structure of the magnetic turbulence (Schekochihin et al., 2004) and allows one to distinguish between different theoretical scenarios for the evolution and saturation of the cosmic magnetic field, which was not possible to do on the basis of lower-order statistics such as the magnetic power spectrum; it also reveals physically interpretable dynamical properties of the system under observation, namely the force exerted by the field on the ambient plasma (see discussion in Sect. 2.3).

Furthermore, we have shown that if the observed magnetic field possesses a small regular component that does not affect the isotropy of the fluctuating part of the field, it may be possible to obtain from the Stokes maps the power spectrum of the fluctuating field itself, as well as that of its tension force (Sect. 2.4.7).

Thus, physically relevant information about the spatial structure and dynamical properties of the magnetic turbulence is contained in the polarised emission maps and can be extracted. This work is an attempt to pave the way towards analysing the large amount of existing and upcoming radio-synchrotron observational data (see, e.g., Gaensler, 2006; Enßlin et al., 2006; Beck, 2008) with the aim of achieving a better understanding of the nature of magnetised turbulence in cosmic plasmas.

Chapter 3

The Hammurabi code

Note: The bulk of this chapter, as well as the Appendix C.1, was published as Waelkens et al. (2009a). Sect. 3.5.3 has been added, and contains published (Jansson et al., 2007) and ongoing work led by collaborators (L. Fauvet and J. Macias-Perez).

3.1 Introduction

Several different types of observation are able to probe the Galactic magnetized ISM: synchrotron radiation, rotation measure, UHECR deflection, dust-related observations (e.g. starlight polarization (Heiles, 2000) and polarized dust emission), and atom-alignment spectroscopic observations, for example, have been proposed (see Yan & Lazarian, 2006).

A more robust understanding of the interstellar magnetized plasma and its radio-emission, related processes is also paramount for current and future CMB experiments (see, e.g., Miville-Deschenes et al., 2008; Page et al., 2007), where the accuracy of the measurements of the polarized CMB signal in particular will be limited by our knowledge of foreground emission (Tucci et al., 2005).

Observational studies of the magnetized ISM are usually based on a single type of observable. However, since the different observables and measurement methods provide complementary information, it is logically more sensible to constrain the magnetized ISM by considering simultaneously all possible observations. We address the need to confront those observations with models by presenting a publicly available software[1] capable of generating mock synchrotron and Faraday rotation observations as well as mock UHECR deflection maps.

The code is constructed in a fashion that should allow its adaptation to complete any type of all or partial-sky line-of-sight integral observations (see, e.g., Waelkens et al. 2008 and Sun et al. 2008).

We briefly summarize previous work on magnetized ISM modeling in Sect. 3.2, and then

[1] Software available at
http://www.mpa-garching.mpg.de/hammurabi

describe the involved Faraday rotation, UHECR deflection, and synchrotron physics, and the simplifying assumptions used in our computation in Sect. 3.3. The implementation of a line-of-sight (hereafter LOS) integration scheme that mimics radiative transfer is discussed in Sect. 3.4. We present some test output using standard, magnetic-field, thermal- and cosmic-ray electron models. We discuss the role of the turbulent field and subgrid modeling in Sect. 3.5.1, and that of helical magnetic fields in Sect. 3.5.1. Finally, we present our conclusion in Sect. 3.6.

3.2 Previous work on Galactic magnetized ISM modeling

Several different magnetized ISM models have already been developed by the community. For example, there are the models of, Beuermann et al. (1985), Han et al. (2006), Brown et al. (2003), Haverkorn et al. (2006b), Page et al. (2007), Sun et al. (2008), Vallée (2008), and Frick et al. (2001) for fitting parametrized Galactic models to data, and Moss & Sokoloff (2008), Sokoloff & Shukurov (1990), Sur et al. (2007), and Brandenburg & Subramanian (2005) for dynamo-theory-based predictions of observational features of GMFs. Feasibility studies for radio telescopes such as LOFAR must address the modeling of small-scale GMF structures (see Jelić et al., 2008, for a first attempt). The data used are mostly total and polarized emission radio surveys of the Galaxy (Taylor et al., 2003; Gaensler et al., 2001; Haslam et al., 1982; Reich & Reich, 1986; Page et al., 2007) as well as measurements of Faraday rotation (Dineen & Coles, 2005; Johnston-Hollitt et al., 2004; Han et al., 2006) and a starlight polarization catalog compiled by Heiles (2000). Theoretical predictions are also heavily based on experience obtained from analyzing synchrotron observations of other spiral Galaxies (see e.g. Beck et al., 1996). Our work complements previous efforts by making it possible to compare simultaneously the largest possible number of observables to theoretical predictions.

3.3 Magnetised ISM tracers

In this chapter we describe the physical processes and assumptions made when developing the HAMMURABI code. This code serves to confront theoretical models of the magnetised ISM with corresponding observations. Section 3.3.2 is also of importance for our derivations concerning the Stokes correlators in chapter 2 and the App. A.

3.3.1 Faraday rotation

The polarisation angle of an electromagnetic wave is rotated when crossing a magnetised plasma, an effect known as Faraday rotation (see e.g. Rybicki & Lightman (1979)). The observed polarisation angle χ is a function of the rotation experienced when crossing the magnetised plasma, the observation wavelength λ, and its original (or intrinsic) angle χ_0 at

the polarised source,

$$\chi = RM\,\lambda^2 + \chi_0\,. \tag{3.1}$$

The rotation measure (hereafter RM), which quantifies the linear rate of change of the angle χ as a function of λ^2, is a function of the integral of the magnetic field $\vec{B}_{LOS}$ along the LOS weighted by the thermal electron density n_e,

$$RM = a_0 \int_{there}^{here} dr\, n_e\, B_{LOS}\,, \tag{3.2}$$

where $a_0 = q_e^3/(2\pi m_e^2 c^4)$, m_e is the electron mass, c is the speed of light, and q_e is the electron charge. RM is positive if the field points towards the observer.

The RM can be measured directly by a fit to Eq. 3.1 only in the particular case of a Faraday screen, i.e., if the observer and the polarised source have a cloud of magnetised plasma in-between them, but no source-intrinsic, Faraday rotation occurs. In the more complicated scenario of several sources along the LOS being embedded in the magnetised plasma, the RM cannot be measured in that way since the polarisation angle will no longer obey a linear dependence on λ^2. A complicated dependence of the polarisation angles on frequency arises in such a case, a situation typically found in our Galaxy, where the synchrotron-emitting cosmic-ray electron population is embedded in the magnetised plasma that produces the Faraday rotation simultaneously.

3.3.2 Synchrotron emission, total and polarised

Relativistically moving charges in a magnetic field emit synchrotron radiation. In modelling the Galaxy we consider a cosmic-ray electron population generated mainly by supernova explosions and subsequent shock acceleration, and a GMF of strength equal to a few micro Gauss and of as a yet unknown topology. In the following, a couple of simplifying assumptions are made:

- The relativistic CR electrons have an isotropic velocity distribution, as measured to high accuracy to be the case at our location in the Galaxy (although, their propagation is anisotropic due to the presence of ordered magnetic fields; Yan & Lazarian 2008b).

- The cosmic-ray electron spectrum is assumed to be a power law with spectral index p. This widely used simplification is motivated by the theory of shock acceleration (a.k.a. Fermi acceleration, which predicts power-law energy distributions; Drury 1983), has been successfully applied to CMB foreground subtraction (Tegmark & Efstathiou, 1996; de Oliveira-Costa et al., 2008; Dunkley et al., 2008; Bottino et al., 2008), and is simultaneously confirmed by the measured cosmic-ray electron spectrum at Earth (e.g. Gaisser & Stanev, 2004, and references therein). However, the same observations, as well as sophisticated simulations, have shown that the power-law assumption is inadequate for the entire energy spectrum (see Strong et al., 2007). Without the power-law assumption

and any other constraint on the shape of the energy distribution of the cosmic ray electrons implies that the analytic computations of the synchrotron emissivity are no longer possible and an integration over energy must be made, a numerically time-consuming operation that the current implementation of the code does not perform (see Sect. 3.5.1).

The synchrotron emissivity (i.e. power per unit volume per unit frequency per unit solid angle) is partially linearly polarised. Its intensity and polarisation properties depend on the strength and orientation of the perpendicular (with respect to the LOS) component of the magnetic field, B_t, and the cosmic-ray electron spatial and energetic distribution. The emissivities are usually subdivided into two components, $j_{\perp,\parallel} = dE_{\perp,\parallel}/dt\, d\omega\, d\Omega\, dV$, respectively perpendicular and parallel to B_t, following Rybicki & Lightman (1979) and Westfold (1959):

$$\begin{aligned} j_\perp(\omega,\vec{r}) &= \frac{1}{4\pi}\frac{\sqrt{3}q^3}{8\pi mc^2}\omega^{\frac{1-p}{2}}\left(\frac{2mc}{3q}\right)^{\frac{1-p}{2}} B_t(\vec{r})^{\frac{p+1}{2}} C(\vec{r}) \\ &\times\Gamma\left(\frac{p}{4}-\frac{1}{12}\right)\left[\frac{2^{\frac{p+1}{2}}}{p+1}\Gamma\left(\frac{p}{4}+\frac{19}{12}\right)+2^{\frac{p-3}{2}}\Gamma\left(\frac{p}{4}+\frac{7}{12}\right)\right], \end{aligned} \tag{3.3}$$

and

$$\begin{aligned} j_\parallel(\omega,\vec{r}) &= \frac{1}{4\pi}\frac{\sqrt{3}q^3}{8\pi mc^2}\omega^{\frac{1-p}{2}}\left(\frac{2mc}{3q}\right)^{\frac{1-p}{2}} B_t(\vec{r})^{\frac{p+1}{2}} C(\vec{r}) \\ &\times\Gamma\left(\frac{p}{4}-\frac{1}{12}\right)\left[\frac{2^{\frac{p+1}{2}}}{p+1}\Gamma\left(\frac{p}{4}+\frac{19}{12}\right)-2^{\frac{p-3}{2}}\Gamma\left(\frac{p}{4}+\frac{7}{12}\right)\right]. \end{aligned} \tag{3.4}$$

Here C depends on the position in the Galaxy and is defined by $N(\gamma)d\gamma = C\gamma^{-p}d\gamma$, γ being the Lorenz factor, $N(\gamma)$ the number density of electrons $\in [\gamma, \gamma + d\gamma]$, and p the spectral index as mentioned above. The charge of the electron is given by q_e, the mass by m_e, and $\omega = 2\pi\nu$, where ν is the observation frequency. The specific intensity I is a function of observation frequency and LOS direction $\vec{\hat{n}}$ given by

$$I(\omega,\vec{\hat{n}}) = \int_0^\infty dr\, \left(j_\perp(\omega, r\,\vec{\hat{n}}) + j_\parallel(\omega, r\,\vec{\hat{n}})\right), \tag{3.5}$$

and the polarised specific intensity P expressed as a complex variable is (see Burn, 1966):

$$P(\omega,\vec{\hat{n}}) = \int_0^\infty dr\, \left(j_\perp(\omega, r\,\vec{\hat{n}}) - j_\parallel(\omega, r\,\vec{\hat{n}})\right) e^{-2i\chi(r\,\vec{\hat{n}})}.$$

The intrinsic emission polarisation angle χ_0 is given by the inclination towards the Galactic North Pole of the local perpendicular-to-the-LOS component of the magnetic field at each position in space (same convention as adopted in Page et al., 2007). The Stokes I, Q, and U

parameters [2] are then represented by integrals over solid angle Ω:

$$\mathrm{I} = \int d\Omega\, I,$$

and

$$\mathrm{Q} - i\mathrm{U} = \int d\Omega\, P.$$

3.3.3 Free-free scattering

Free-free emission, also referred to as bremsstrahlung, arises from the scattering of charged particles by each other. Following Rohlfs & Wilson (1996), we write the free-free intensity (in Kelvin) as

$$I_{ff}(\omega) = \int_0^{\tau_{max}} d\tau\, T_e(\tau) e^{-\tau(\vec{r},\omega)}, \tag{3.6}$$

where I_{ff} is the measured temperature (in Kelvin), T_e is the electron temperature (in Kelvin), and the optical depth is given by

$$\tau = 8.235 \times 10^{-2} T_e^{-1.35}(\vec{r})(\omega/2\pi)^{-2.1} EM(\vec{r})\,. \tag{3.7}$$

Here the frequency $\omega/2\pi$ is in GHz and the emission measure (EM) (in pc/cm^{-6}) is

$$EM = \int_{r_0}^{r_1} dr\, n_e^2. \tag{3.8}$$

Furthermore, at low frequencies free-free absorption is also significant for synchrotron radiation, which is attenuated by a factor $exp(-\tau)$.

3.3.4 UHECR propagation

UHECR's are deflected by the GMF due to the Lorentz force. The Larmour radius for relativistic particles is $r_g = p\,c/Z\,q_e\,B_t$, $Z\,q_e$ being the charge of the UHECR, and p the momentum perpendicular to the magnetic field B_t. Provided the sources of UHECRs can be identified, an UHECR deflection measure (UDM) can be extracted from the UHECR arrival distribution by fitting the arrival data (position and energy). The net deflection of an UHECR can be approximated by the LOS integral (see e.g. Kachelrieß et al., 2007)

$$\Theta_{\mathrm{offset}} \approx \int dl\, \vec{r}_g^{-1} = \frac{Z\,q_e}{pc} \int dl \vec{B}_t \equiv \frac{Z\,q_e}{pc} U\vec{D}M. \tag{3.9}$$

[2] Here the specific intensities are written in italics (I,Q,U), while the observed Stokes parameters (I,Q,U) are denoted by Roman letters.

3.4 Implementation

In this section we present the implementation of the physics described in chapter 3.3 and the technical characteristics of the HAMMURABI code. Given a

- 3D GMF model,
- 3D cosmic-ray electron density model,
- 3D thermal electron density model,

HAMMURABI computes full sky maps for

- the Galactic RM contribution to the extra-galactic sources,
- synchrotron I,Q, and U Stokes parameters, taking into account intrinsic Galactic Faraday depolarisation,
- free-free emission and,
- UHECR deflection intensity and orientation maps.

The sky maps in HAMMURABI are subdivided into equal area pixels following the HEALPix[3] pixelization scheme of Górski et al. (2005). The total number of pixels for an all-sky map, which defines the angular resolution, is $N_{\rm pix} = 12\,\mathrm{NSIDE}^2$, with $\mathrm{NSIDE} = 2^k$ and $k = 0, \ldots, 13$ (a HEALPix package limitation, which can be altered, see App. C.1). The angular size of a pixel ($\Delta\theta$) can be approximated by

$$\Delta\theta \approx \sqrt{\frac{3}{\pi}}\frac{3600'}{\mathrm{NSIDE}}\,. \tag{3.10}$$

The observation volume associated with one of the HEALPix-map pixels is sampled along the LOS at a constant radial interval Δr. As a consequence of the conical shape of the implied effective observation beam, the volume units increase with radius, and hence the weights of the sampling points along the LOS also increase. To limit the amount of non-homogeneity in the sampling, the code allows the volume resolution to be increased by splitting the beam into subbeams at some radius, which subsequently can be split further later on. We refer to the the implied 3-D sampling grid as the "3D HEALPix grid"(for further details, see Appendix C.1).

Formally, the maximally achievable volume resolution, i.e. the largest volume unit at the finest possible resolution $\Delta\theta \sim 0.43'$, (corresponding to $\mathrm{NSIDE} = 2^{13}$) is $V_{ext} = 4\pi R_{max}^2 \Delta r (12 \cdot 2^{26})^{-1} \sim (4\mathrm{pc})^3$ for $R_{max} \sim 32$kpc and $\Delta r = 4$pc, since we impose an approximately cubic volume unit according to $\Delta r \sim (4\pi R_{max}^2/12 \cdot 2^{26})^{1/2}$. This implies that variations in the input parameters (e.g. magnetic field and thermal electron distribution) on scales smaller

[3] http://healpix.jpl.nasa.gov

than this volume can only be taken into account with subgrid modelling if they persist to the largest radii simulated. We however, note that this is an upper limit because fluctuations are probably stronger closer to the Galactic disk, where resolution, due to the cone-like shape of the observational volume, is in all cases higher.

The quantities described in chapter 3.3 are obtained by means of a discretisation of the respective integrals, as detailed in Appendix C.1. We note that Sun et al. (2008) enhanced the original code by introducing free-free absorption. This implementation is relevant mainly to frequencies below 408 MHz. Furthermore, Sun et al. (2008) also introduced an empirical coupling between the thermal electron density and the random component of the RM. This implementation is necessary to explain the degree of depolarisation in their simulated 1.4GHz map. It is stressed by the authors that the theoretical interpretation thereof is unclear. Although present in the code, it is not described here (for further details, see Sun et al. (2008)).

The 3D HEALPix grid, since the value of one observation pixel stems from the contribution of several subbeams, allows one to take into account approximately effects such as beam depolarisation (see Appendix C.2 for details).

3.4.1 Features

HAMMURABI is also suitable for simulations of partial sky coverage. A single pixel or a list of pixels, representing either patches or separate locations on the sky output maps, can be computed. There is also the option to compute RMs for an individual pixel only out to a specified distance. This is relevant to simulating RM observations of radio pulsars or other polarised sources with distance information, in our own Galaxy. Polarised sources along the same LOS allow fractions of the ISM plasma to be probed, unlike extragalactic polarised sources, which enable the study of the integrated RM along the entire LOS through the Galaxy. The mock observations in this case are completed without beam-splitting and at the highest possible angular resolution, since RM are effectively obtained from point sources.

3.5 Examples

We select standard 3D input models to demonstrate the capabilities of the code. The scope of this section is to present a proof of concept of what can be achieved by HAMMURABI. Applications of the code were presented by Jansson et al. (2007) and Sun et al. (2008), while work with L. Fauvet and J. Macias-Perez is underway. Here we will mainly be referring to the results of Sun et al. (2008). Their preferred GMF model and cosmic-ray electron model, derived by attempting to fit a broad range of observables, are compared to the corresponding models suggested by Page et al. (2007), and fitted to reproduce solely the polarisation angles observed by the WMAP satellite. Sun et al. (2008) demonstrated that the Page et al. (2007) model as well as every model in the literature analysed in their work were unable to reproduce different

sorts of observations of the magnetised ISM satisfactorily, since they are all constructed by considering only a particular sort of data. The discrepancies of the models presented here, visible by eye, illustrate the code's abilities. Additionally, in Sect. 3.5.3, we briefly present the results of Jansson et al. (2007) as well as a brief overview of work in progress with L. Fauvet and J. Macias-Perez .

3.5.1 Inputs

All input models presented here can be easily substituted by other models.

The thermal electron density model

For the thermal electron distribution we use the NE2001 model (see Cordes & Lazio, 2002, 2003). This model subdivides the Galaxy into several large-scale structure elements such as a thin disk, a thick disk, spiral arms, as well as some local small-scale elements such as supernova bubbles. The NE2001 model presents a smooth thermal electron distribution. To take into account the clumpiness of the medium, we introduce a filling factor $f_e(z) = 0.07 \exp(2|z|)$, (see Berkhuijsen et al., 2006; Sun et al., 2008, for details) where z is the distance from the Galactic plane in kpc.

Thermal electron temperature model

Sun et al. (2008) proposed a thermal electron temperature (T_e) model

$$T_e(\vec{r}) = 5780 + 287r - 526|z| + 1770z^2\,, \tag{3.11}$$

based on work by Quireza et al. (2006), Reynolds et al. (1999), and Peterson & Webber (2002), where T_e is in Kelvin and the length scales are in kpc.

The cosmic-ray electron density model

We use the cosmic-ray electron density models suggested by Page et al. (2007) and Sun et al. (2008).

- The model in Page et al. (2007) consists of an exponentially decaying disk with characteristic height $h_d = 1\,\mathrm{kpc}$ and characteristic radius of $h_r = 5\,\mathrm{kpc}$. We note that to compute the synchrotron emissivity, as can be seen in Eqs. 3.3 and 3.4, we require knowledge of the spatially dependent function C, not the cosmic-ray electron density. However, since we are assuming a Galaxy-wide, unique, power-law, energy spectral slope with a spectral index $p = 3$ (note that in principle the code allows us to associate a different spectral index with each volume unit), these quantities are proportional to each other. The value of $C_{\mathrm{Earth}} = 6.4 \cdot 10^{-5}\mathrm{cm}^{-3}$ at Earth's position is observed (see e.g. Fig. 4 of Strong

et al., 2007), and although it is unclear that this is representative of other regions in the Galaxy (Sun et al., 2008; Pohl & Esposito, 1998; Strong et al., 2004), we use it as a zeroth order approximation of the normalisation (which is neither necessary nor provided by Page et al. (2007)) of our distribution,

$$C = C_0 \, exp\,[-r/h_r] \; sech^2(z/h_d)\,, \tag{3.12}$$

where r is the Galactic radius, while z is the height, and C_0 is such that $C = C_{\mathrm{Earth}}$ at Earth's position.

- Sun et al. (2008) proposed

$$C(R,z) = C_0 \exp\left(-\frac{R - R_\odot}{8 \text{ kpc}} - \frac{|z|}{1 \text{ kpc}}\right) \tag{3.13}$$

where $C_0 = C_{\mathrm{Earth}}$, while $C(R < 3 \text{ kpc}) = C(R = 3 \text{ kpc})$ and $C(|z| > 1) = 0$. The abrupt truncation at a scale height of $|z| > 1$ is necessary to accommodate low synchrotron emission at high latitudes, where an anomalously strong halo magnetic field is required to account for high RM measurements. Sun et al. (2008) cautioned that this appears unrealistic and suggests that a larger scale height of the thermal electron density (roughly twice as large as the one suggested by Cordes & Lazio (2002)) could resolve the problem by diminishing the required value of the halo magnetic field. This was confirmed by a joint analysis of pulsar dispersion measures and Hα emission by Gaensler et al. (2008). Furthermore the spectral index p is 3 for observational frequencies higher than 408 MHz and 2 otherwise. Sun et al. (2008) adopted this simplification based on observations of Roger et al. (1999) and Reich & Reich (1988a,b), which support a flatter spectrum below 408 MHz.

The frequency dependence of the observed spectral index, which is adjusted by hand in the Sun et al. (2008) model, occurs, we emphasise, because the assumption of a single power-law energy distribution of the cosmic-ray electrons (used in this work) is not applicable to the entire spectrum (as mentioned in Sect. 3.3.2). To reproduce the frequency dependence of the observed spectral index in a consistent way, an extension of the code is planned, incorporating outputs of simulations such as GALPROP (Strong et al., 2007), which present spatially varying density and non-power-law like cosmic-ray energy spectra, into HAMMURABI. We note that this also implies that an integration over all energies would be required, significantly increasing the computation time.

Large-scale Galactic magnetic-field models

The behaviour of the synchrotron emissivity is dependent mainly on the magnetic-field distribution, as shown in Eqs. 3.3 and 3.4.

It is a common practise to subdivide the Galactic magnetic field into large-scale and small-scale components. The latter will be addressed in Sect. 3.5.1. The subdivision into these two classes of fields is somewhat arbitrary, and we adopt the convention that the large-scale field is statistically anisotropic at any point in the Galaxy, while the small-scale field is not.

GMF modelling has been completed in direct studies of the Galactic magnetic field. See Page et al. (2007), Sun et al. (2008), Jansson et al. (2007), Haverkorn et al. (2006b), Brown et al. (2003), Han et al. (2006), and others; in the context of UHECR propagation, see Kachelrieß et al. (2007), Tinyakov & Tkachev (2002), Prouza & Šmída (2003), and Harari et al. (2000). Inspired by observations of the radio-polarisation patterns of other spiral galaxies, GMF models typically, present spiral-like structures. We present simulations using the model of Page et al. (2007) and the favoured (ASS+RING) model proposed by Sun et al. (2008). The expressions, along with some other models not presented in this chapter but included in the code, are reproduced in Appendix C.3. Alternative magnetic field models can easily be incorporated into the code.

Small-scale magnetic field

Although the turbulent component of the GMF has been studied extensively (see e.g. Haverkorn et al. (2003), Han et al. (2004), and Haverkorn et al. (2006b, 2008) as well as chapter 2), there is, to our knowledge, not yet any model that describes it to a satisfactory degree. Observational constraints on its strength relative to that of the large-scale field imply that it is of roughly the same amplitude (i.e. a couple of micro Gauss; Beck 2001). Given a magnetic-field power spectrum, HAMMURABI allows one to simulate, a Gaussian random-field realisation. A realistic turbulent field, however, need not be Gaussian, since simulations of turbulence contain sheet-like structures that evidently differ from that expected of a Gaussian field (see e.g. Schekochihin et al. (2004), Schekochihin & Cowley (2006), as well as the discussion in chapter 2). This implies that the Gaussian random field should by construction reproduce the correct two point statistics of a true field, although it will not reproduce the higher order statistics because real fields are not observed to be Gaussian (see e.g. the figures in Jaegers (1987) and Clarke & Ensslin (2006)). Furthermore, this modelling assumes that the power spectrum of the field is known, which in the case of the Galaxy, to our knowledge, has not yet been determined. There are, however, measurements of the magnetic power spectrum in the intra-cluster medium (e.g. Vogt & Enßlin, 2005; Guidetti et al., 2008; Govoni et al., 2006). Furthermore, we note that the random field simulation is performed on a Cartesian grid and then interpolated to the 3D HEALPix grid, from which the mock observations are computed. This interpolation can introduce an error, which is small if the 3D HEALPix grid has volume units at least as small as those of the Cartesian grid. We also note that the Gaussian random field is *not* divergence-free, although we refer the reader to Sect. 3.5.1.

Helical fields

Helical magnetic fields have a broken mirror symmetry and can be illustrated most effectively by twisted flux tubes. Topological helicity is given by $\int dV\, A \cdot B$, where A is the vector potential of the field, and $B = \nabla \times A$. Current helicity is given by $\int dV\, j \cdot B$, where j is the electrical current, satisfying $j = \nabla \times B$. Both types of helicity are closely related. Topological helicity is an almost conserved quantity, even in non-ideal MHD, and plays a crucial role in magnetic-dynamo theory. Therefore, HAMMURABI, in addition to its own in-built, power-spectrum-based, Gaussian-random-field generator, was adapted to accept random small-scale fields with magnetic helicity generated by a separate code. This code, also available for download, is called GARFIELDS (first applied in Kitaura & Ensslin, 2007). The field becomes divergence-free in Fourier space by subtracting the component parallel to the wave vector and multiplying it by 3/2 to compensate for the loss of power (which is valid in the case of isotropy)

$$\hat{B}'_i = \frac{3}{2}\hat{B''}_i \left(1 - \overline{k}_i\right) , \tag{3.14}$$

where $\hat{B}''$ is the original Gaussian random field, while the divergence-free component $\hat{B}'_i = \hat{B}'_i(\vec{k})$ is such that $\langle \hat{B}'_i \hat{B}'^{*}_j \rangle = \left(\delta_{ij} - \overline{k}_i \overline{k}_j\right) \hat{m}_1(k)/2$, where $\hat{m}_1(k)$, as in Eq. 2.2, is the magnetic power spectrum (for details see the discussion in Sect. 2.4.5.). The hat denotes a Fourier transform, δ is the Kronecker delta, $\overline{k}_i$ is an unit vector, and ϵ_{ijk} is the permutation symbol. The helicity is imprinted onto the divergence free Gaussian random field $\vec{B}'$ by

$$\hat{B}_m = \frac{1}{\sqrt{1+\alpha^2}} \left(\delta_{jm} + i\alpha\epsilon_{ijm}\overline{k}_i\right) \hat{B}'_j , \tag{3.15}$$

where Maximal helicity is found for $\alpha = -1$ and 1, and leads to a magnetic correlation tensor of the form

$$\langle \hat{B}_i \hat{B}^{*}_j \rangle = \left[\frac{1}{2}\left(\delta_{ij} - \overline{k}_i \overline{k}_j\right) - i\epsilon_{ijk}\overline{k}_k \frac{\alpha}{1+\alpha^2}\right] \hat{m}_1(k) . \tag{3.16}$$

We note that the divergence-free and helical properties of the simulated small-scale field only hold true in the Cartesian grid onto which GARFIELDS writes the field. As above, when projecting this onto the 3D HEALPix grid, an error occurs, which is smaller for finer 3D HEALPix grids. Furthermore, we note that the separately specified large-scale field does not need to posses any of the aforementioned characteristics.

3.5.2 Synchrotron and RM outputs: comparison with observations

We compare our example simulation with observed data. The mock total intensity I, polarised intensity P, polarisation angle PA and RM maps for our two different field configurations, and slightly different cosmic-ray electron distributions of Sun et al. (2008) and Page et al. (2007)

are shown in comparison to the observed synchrotron emission at 0.408 MHz (total intensity) and 23 GHz (polarised emission), and a RM map extrapolated from the existing still sparse RM observations (Fig. 3.1). All maps in this figure and throughout the paper are presented at a resolution of NSIDE = 128, Δr = 0.21kpc, $H_{\rm obs}$ = 2, $H_{\rm max}$ = 3 (see definitions in Appendix C.1). A Gaussian random field with a Kolmogorov spectrum $k^{-5/3}$ and a lower cutoff at k_0 = 1kpc^{-1} (see, e.g., Han et al., 2004), and an upper cutoff given by the Nyquist frequency of the simulation box $k_{Nyquist}$ = 3.2kpc^{-1}, was added to both large-scale GMF models. We caution that this scale range is insufficient to describe the turbulent field in the Galaxy, as is evident from the even smaller-scale fluctuations present in the observations, although it serves our demonstration purposes. Following Sun et al. (2008), the random field amplitude is $\langle B_{ran}^2 \rangle^{1/2} = 3\mu$G.

Magnetised ISM models in the literature are designed mostly to fit a selected set of data. For example, Page et al. (2007) reproduced PA observations, and, as can be seen in Fig. 3.1, were able to do this remarkably well. However, their model was evidently unable to reproduce any of the other observations (as shown by Sun et al., 2008). Furthermore, Sun et al. (2008) noted that most spiral magnetic-field configurations have similar PAs, suggesting a highly degenerate fitting problem.

The Sun et al. (2008) models for the GMF and cosmic-ray electron distributions were designed to reproduce longitude and latitude RM profile observations and I and P observations at 408 MHz, 1.4 GHz, and 22.8 GHz, but no optimisation was performed for the PA observations. We note also that Sun et al. (2008), unlike Page et al. (2007) who completed a parameter scan, adjusted the model parameters based on trial and error. The attentive reader might notice a faint horizontal-stripe-like pattern in the I and P simulations of this model, which is due to a combination of our limited radial step size Δr = 0.21kpc, and an abrupt cut in the cosmic-ray electron density at 1 kpc away from the Galactic plane (as discussed in Sect. 3.5.1). In other words, the code cannot resolve a sharp cut. A smaller Δr, of course, would cause the feature to vanish, although it would be inconsistent with our recommendation in Appendix C.1 to define Δr such that the maximum volume unit at the largest shell is close to a cubic form. The most striking difference between the two models lies probably in the different RM maps, mainly due to so-called field reversals in the Sun et al. (2008) model, which are absent in the WMAP model.

3.5.3 Additional studies with HAMMURABI

So far we have mainly illustrated the code's capabilities by referring to results obtained in Sun et al. (2008). We reserve this section to briefly present the findings of two further related works we are involved in: Jansson et al. (2007) as well as current progress of a collaboration headed by L. Fauvet and J. Macias-Perez. Both works perform systematic parameter scans, unlike the trial and error approach of Sun et al. (2008). Moreover, their approaches on how to evaluate the

Page et al. 2007	Sun et al. 2008	observations

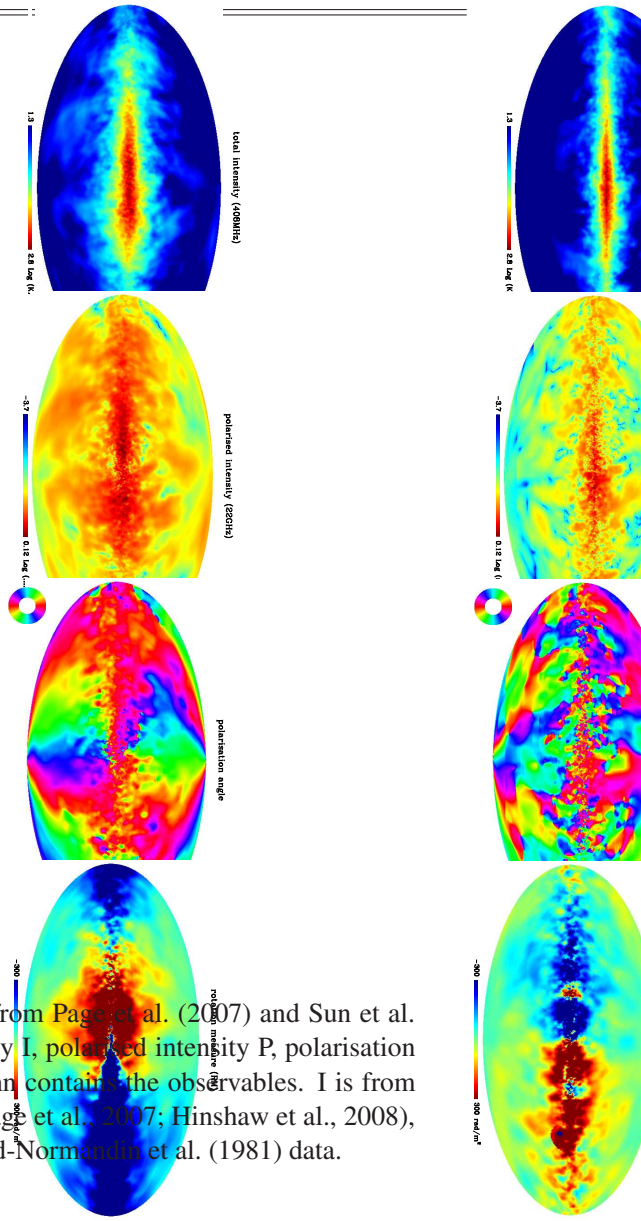

Figure 3.1: Comparison of mock observations based on models from Page et al. (2007) and Sun et al. (2008) with observed data. Each row corresponds to total intensity I, polarised intensity P, polarisation angle PA and rotation measure RM respectively. The third column contains the observables. I is from Haslam et al. (1981, 1982), P and PA are WMAP observations (Page et al., 2007; Hinshaw et al., 2008), while RM is from Dineen & Coles (2005) derived from the Simard-Normandin et al. (1981) data.

goodnes of fit and the parametrisation suggested for their models are different. The diversity of ways the problem of constraining the Galactic magnetised ISM is addressed is appropriate given its complexity.

The Jansson et al. (2007) work

In Jansson et al. (2007) the constraints on the Galactic magnetic field imposed by the WMAP K-band (i.e. 23 GHz) polarisation observations[4] (Page et al., 2007) are studied. At these frequencies the dominating polarised emission mechanism is sychrotron radiation, and Faraday rotation effects are negligible. The signal is therefore only dependent on the Galactic magnetic field and the cosmic-ray electron density. We choose the later to be fixed to the Page et al. (2007) model (see Sect. 3.5.1). We concentrated on modeling the more relevant Galactic magnetic field. The synchrotron emissivity depends on the magnetic field by a power of $(p+1)/2$, where usualy $p \approx 3$, instead of a power of 1 dependence, as is the case for the cosmic-ray electron density (see Eqs. 3.3 and 3.4).

Following the parametrisation presented in the App. C.3.3, we have in Galacto-centric cylindrical coordinates (see the App. C.3 for the conventions)

$$\begin{cases} B_{\hat{r}} &= B(r,\theta,z)\sin pitch\,, \\ B_{\hat{\varphi}} &= B(r,\theta,z)\cos pitch\,, \\ B_{\hat{z}} &= B(r,\theta,z)\,, \end{cases}$$

and

$$\begin{aligned} B(r,\theta,z) &= B(r,\theta)e^{\frac{z}{z_0}}\,, \\ B(r,\theta) &= B(r)\cos\left(\theta - \beta ln\left(\frac{r}{r_0}\right)\right)\,, \\ B(r) &= \begin{cases} b_0\dfrac{r_c}{r} & r \geqslant r_c\mathrm{kpc} \\ b_0 & r < r_c\mathrm{kpc} \end{cases}\,. \end{aligned}$$

Here b_0, r_c, z_0 and the pitch angle *pitch* are the parameters which charaterise the model. The mock observations generated from the corresponding parametrisation are confronted with the observed WMAP data by means of a χ^2 fit

$$\chi^2_Q = \sum_{i=1}^{pixels} \frac{\left(Q_i^{model} - Q_i^{data}\right)^2}{\sigma^2_{Q,i}}\,. \tag{3.17}$$

Here, the $\sigma^2_{Q,i}$ corresponds to the variance of the 1 deg patches (the original resolution at K-

[4]The total intensity data is not analysed since it is not clear what sort of emission mechanism is behind it (see Miville-Deschenes et al., 2008).

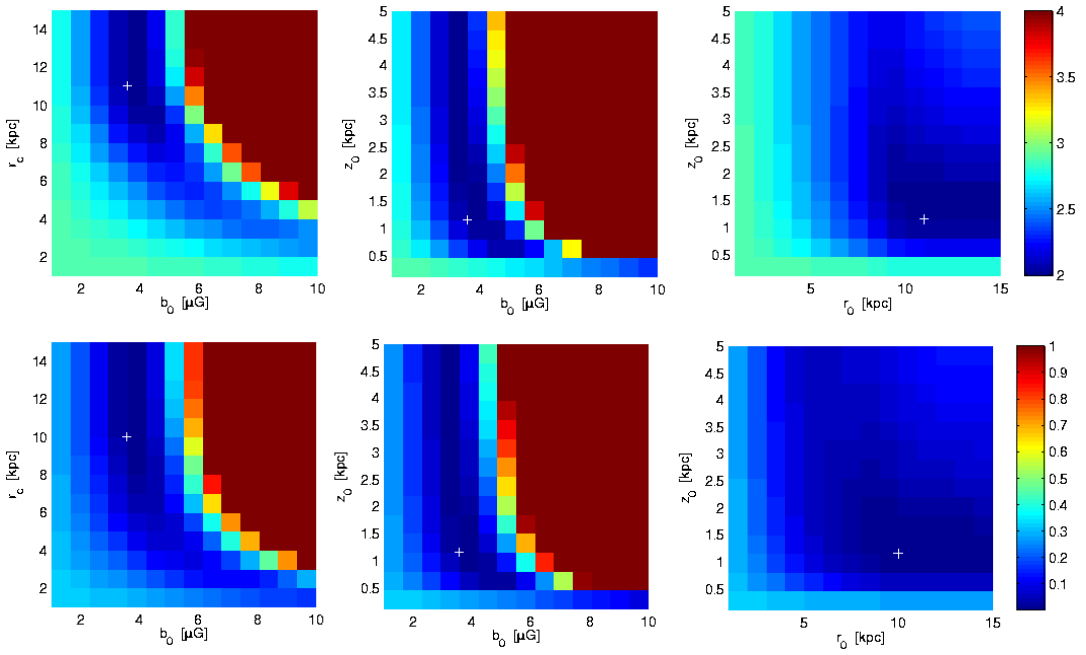

Figure 3.2: χ^2 contour plots for the Jansson et al. (2007) magnetic field.

band) contained inside a smoothed 4 deg patch. The maps are smoothed since the idea here is to probe the larger scales of the field. The Eq. for U is similar to Eq. 3.17. The quantity to be minimised is $\chi^2_{QU} = \chi^2_U + \chi^2_Q$.

Keeping the magnetic pitch angle $pitch = -10$ deg and $r_0 = 10.55$ kpc and using a regular grid to sample the parameter space, Jansson et al. (2007) find no unique best-fit parameters, as a number of combinations of the search parameters yield a χ^2 very close to the minimum.

Figure 3.2 shows the results of a similar parameter scan, but this time applied to mock observations generated with $b_0 = 3.5\,\mu$G, $r_c = 10$ kpc, $z_0 = 1.15$ kpc, $pitch = -10$ deg and $r_0 = 10.55$ kpc. The goal here is to retrieve the input parameters. As can be clearly seen in the contour plots in Fig. 3.2, the ambiguity in the solution remains. Nevertheless the input parameters could be recovered for this exercise. Jansson et al. (2007) conclude that even with ideal data the discrimination between different Galactic magnetic field models based on polarisation data alone is difficult. This goes along the lines of the statement of Sun et al. (2008), as mentioned in Sect. 3.5.2, that most spiral magnetic-field configurations have similar PA patterns.

The Fauvet & Macias-Perez work

Following the work of Aumont (2007), L. Fauvet and J. Macias-Perez expanded the HAMMURABI code to simulate also dust emission observations. This is particularly attractive, since dust emission does not depend on the cosmic-ray electron distribution, therefore providing an extra independent constraint on the properties of the Galactic magnetic field. However, we note that

unlike the code's standard magnetised ISM tracers (synchrotron, Faraday rotation, UHECR deflection and free-free emission), the physics of dust alignment, radiation and absorption is not yet fully understood as well as being considerably more complex (Lazarian, 2003). The resulting uncertainties in the dust physics models make the constraining of the magnetic field and dust properties even more challenging.

In a similar approach as the one proposed by Page et al. (2007), the three dimensional information on the Galactic magnetic field model is used to extrapolate the polarisation properties of the Finkbeiner et al. (1999) dust emission map. I.e., the polarisation angle map and the polarisation fraction map are computed from a three dimensional magnetic field model. Multiplying the polarisation fraction map with the Finkbeiner et al. (1999) map yields the polarised intensity map. The polarisation angle map can then be used to obtain the respective Q and U Stokes parameter maps.

The dust distribution is modelled as a single component gas with number density

$$n_d(r,z) = n_{d,0}\, e^{-r/h_{d,r}}\, e^{-z/h_{d,z}}\,. \tag{3.18}$$

Here r and z are the usual Galacto-centric cylindrical coordinates. The characteristic hight of the dust disc is $h_{d,z} = 0.1\,\mathrm{kpc}$, while the characteristic radial length is $h_{d,r} = 3\,\mathrm{kpc}$. The normalisation, given by $n_{d,0}$, is not specified, since the resulting polarisation maps will have their normalisation pegged to the total intensity map.

The Q and U Stokes parameters are computed first according to

$$\Delta I_d = n_d\, \Delta R \tag{3.19}$$

$$\Delta Q_d = n_d\, \cos(2\chi_0)\, F(\chi_0)\, \Delta R\,, \tag{3.20}$$

$$\Delta U_d = n_d\, \sin(2\chi_0)\, F(\chi_0)\, \Delta R\,. \tag{3.21}$$

As before, χ_0 is the intrinsic polarisation angle of the dust emission. The intensity in this model is dependent only on the dust density. The $F(\chi_0) = \sin^3\chi_0$ factor is empirically determined, and is related to the dust extinction (see Aumont, 2007, for details).

After the LOS integration the Q and U maps are renormalised according to

$$Q_{d,\,final} = (Q_d/I_d)\, G\,, \tag{3.22}$$

$$U_{d,\,final} = (U_d/I_d)\, G\,. \tag{3.23}$$

Here $G = I_{d,\,FDS}(\nu/\nu_{FDS})^{\beta_d}$, with the spectral index for dust β_d, and $I_{d,\,FDS}$ the Finkbeiner et al. (1999) map which is at frequency $\nu_{FDS} = 353\mathrm{GHz}$. The renormalisation is analogous for the synchrotron emission. However, the template is the Haslam 408 MHz map (Haslam et al., 1981, 1982).

The goodnes of fit in this work is determined by how well the resulting temperature and polarisation power spectra fit the observed ones. The result of a parameter scan for the magnetic

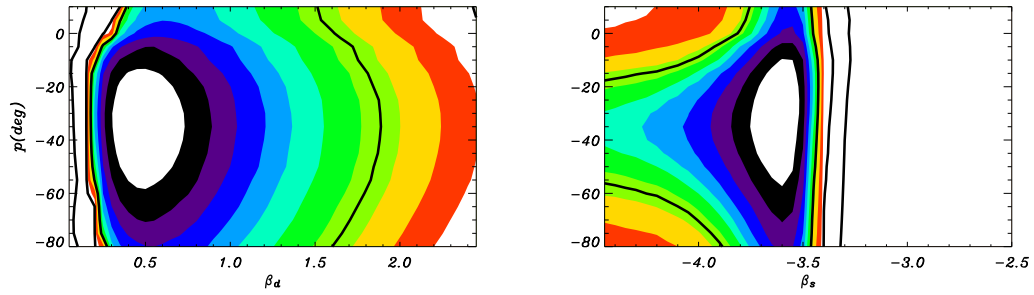

Figure 3.3: Parameter contour plots for dust spectral index β_d, pitch angle and the synchrotron spectral index β_s.

field described in the App. C.3.4, is shown in Fig. 3.3. The prefered values for the synchrotron spectral index are on the higher end of what is infered from observations. Remarcably unusual are the extremely high values for the pitch angle. The reason and implications for this are not yet clear and require further investigations.

3.5.4 Helicity in the ISM?

Our code provides the possibility to study the effects of magnetic helicity on observations. In Fig. 3.4, field realisations with and without helicity are compared. Although they are clearly different, there is no qualitative difference between the single frequency maps from fields with helicity and without. This implies that measuring helicity in the ISM is difficult and the necessary multi-frequency methods required for its measurement in Faraday tomography observations (Brentjens & de Bruyn, 2005; Schnitzeler et al., 2007) still have to be developed. The availability of a tool for generating mock observations might be of assistance in developing these methods and feasibility studies for observations designed to determine the helicity in the ISM.

3.5.5 UHECR deflection outputs

As a generic tool for studying the GMF, HAMMURABI also helps in preparing UHECR-based magnetic field studies, once the sources of the UHECR particles have been identified. We included the option to compute the deflection of ultra-relativistic charges by the GMF in the code. This is yet another observable by which the GMF may be further constrained in the future. Particles of enough high energies (above 57 EeV, where $EeV = 10^{18} eV$) are not isotropised by the magnetic fields, therefore their arrival directions can be used to probe the structure of the field. Presently, there are a few dozen registered events at those energies, and their origin is still speculative (The Pierre Auger Collaboration, 2007). Figure 3.5 represents the deflection intensity for the large-scale Sun et al. (2008) model. We note that the strong halo field is controversial (as discussed in Sect. 3.5.1). The deflection angle of an individual UHECR is

Figure 3.4: Polarised intensity of a field without and one with helicity. The colours in the plot are equally distributed over an area to enhance the visualisation of structures at the expense of proportionality information.

Figure 3.5: UHECR deflection measure map from the Sun et al. (2008) large-scale magnetic field model. To date, only a few dozen UHECR detections above 57 EeV have been reported (The Pierre Auger Collaboration, 2007).

calculated by multiplying the deflection intensity map by $Z\,q_e/p\,c$ for this particle, as in Eq. 3.9.

A LOFAR, SKA, WMAP, Planck tool

The frequency range of HAMMURABI synchrotron simulations, from ~ 100 MHz to ~ 100 GHz, covers currently running experiments such as WMAP as well as the upcoming generation of radio telescopes such as Planck, LOFAR and SKA. HAMMURABI has been developed to support the scientific exploitation of the data of these experiments and to provide synthetic observations for design studies. It is capable of generating full- or partial-sky (not shown) maps as well as individual LOS (see Fig. 3.7), which are useful for non-diffuse measurements, such as RMs.

Figure 3.6 shows the full-sky polarised intensity P for the aforementioned Sun et al. (2008) model (applying their low frequency corrections due to free-free absorption and a random RM enhancement factor, motivated by a coupling between thermal electrons and the random magnetic field). This model was shown to reproduce the global features of latitude and longitude profiles of observations at 1.4GHz. Our intention was to demonstrate the effect of Faraday depolarisation, which, as can be seen, changes the patterns on the maps as a function of frequency.

Figure 3.6: Simulated polarised intensity P at 1 and at 2GHz of the Sun et al. (2008) model. The colours in the plot are equally distributed over area to enhance the visualisation of structures at the expense of proportionality information. The Faraday depolarisation effect changes the complex patterns as a function of the wavelength. The higher thermal electron density on the Galactic plane keeps Faraday depolarisation active long after it already ceased to be relevant in the Galactic halo.

Figure 3.7: The simulated rotation measure as a function of dispersion measure. We used a Gaussian random field with an upper cutoff of 5 kpc and a root-mean-square of 6 μGauss. Pulsar polarisation measurements are, with the advent of SKA, expected to become numerous, allowing us to chart the GMF in three-dimensions, as shown here, where the RM is plotted as a function of the DM for one LOS.

In principle, multi-frequency simulations permit one to take into account beam-width depolarisation effects. Since measurements completed using true telescopes correspond to an integral over some frequency band, bandwidth depolarisation will also occur provided the Faraday effects are sufficiently strong across the bandwidth. Although bandwidth depolarisation is not a standard HAMMURABI feature, it can be emulated by coadding closely spaced frequency maps.

The framework of the code is built to allow additions of any other beam-like observables such as in Waelkens et al. (2008), Sun et al. (2008).

3.6 Chapter conclusion

We have presented the HAMMURABI code, a tool for simulating rotation-measure, total and polarised Galactic synchrotron-emission maps while taking into account Faraday rotational-depolarisation effects and UHECR deflection maps.

By considering a set of well-known input models from the literature (NE2001 for the thermal electron distribution, Sun et al. (2008) and Page et al. (2007) for the cosmic-ray electron distribution and the Galactic magnetic field), we provided example outputs, comparing them to corresponding observations to illustrate the code's abilities as a scientific tool for charting the Galactic magnetised plasma and the cosmic-ray electron distribution.

In the same spirit we also presented findings obtained with the HAMMURABI code (Jansson

et al., 2007), as well as ongoing work led by L. Fauvet and J. Macias-Perez.

Full galaxy simulations are currently limited by the finite HEALPix-grid resolution, which prohibit us from probing fluctuations with characteristic lengths of less than 4 pc. A second limitation is that the widely-used approximation of a power-law energy distribution of the cosmic-ray electrons has been shown to be questionable by sophisticated cosmic-ray propagation simulations (Strong et al., 2007). The degree to which this affects the precision of our simulations has yet to be assessed. Furthermore, our non-ray-tracing calculations of UHECR deflections may not fulfil the strict precision requirements when the UHECR's trajectory through the Galaxy becomes deflected sufficiently, but serve rather as a first approximation.

It was shown that, unsurprisingly, models designed to fit only a fraction of the available observational data on GMF might fail to reproduce the remaining observational information not taken into account in their construction.

This is an indication that the constraints to the GMF might be highly degenerate. Hence confronting the models with the broadest possible range of observations on the Galactic magnetic field is paramount to achieving any useful statement about the field. The motivation for multi-observation constraints, as done by Sun et al. (2008), is well illustrated by a recent work of Gaensler et al. (2008), which confirms the suggestion of a thermal electron density scale hight twice as large as the one used in NE2001 model.

Furthermore we have displayed HAMMURABI's capabilities of generating low-frequency mock observations, where Faraday effects play a significant role. This can be used in feasibility studies and the analysis of true observations by forthcoming low-frequency radio telescopes such as LOFAR or SKA (note that the latter can also observe at high-frequencies).

HAMMURABI can be applied in constraining the Galactic magnetised plasma and increasing our understanding of radio Galactic emission and UHECR source locations. Already a worthy scientific goal by itself, it will also have implications on our understanding on foreground emission subtraction for experiments such as Planck or WMAP.

Chapter 4

The Sunyaev-Zeldovich effect as a CMB foreground

Note: This chapter, as well as Appendix B.1, was published as Waelkens et al. (2008). Figures 4.4 and 4.5 and 4.6 were produced by M. Maturi. The optimally linear matched filter developed with M. Maturi was also applied in a work related to an attempt to detect the Rees-Schiama effect (Maturi et al., 2007), which is not further addressed here.

Here we present a brief theoretical introduction to the SZ effect and perform an order-of-magnitude estimate of the galactic tSZ and the kSZ effects as a first step toward investigating their importance as CMB foregrounds. We do also investigate whether any relevant contamination of the CMB polarisation signal due to the galactic kSZ effect is expected.

4.1 Introduction

The role of the Sunyaev Zeldovich effect (hereafter SZ) as a CMB foreground has been widely studied for clusters of galaxies (see for example Sunyaev & Zeldovich (1972), Sunyaev & Zeldovich (1980), Birkinshaw (1999), Dolag et al. (2005) and Schäfer et al. (2006)). Due to the high cluster temperatures the relevant effect in these cases is the thermal SZ effect (hereafter tSZ), while the kinetic SZ effect (hereafter kSZ) is secondary. In this work we study the galactic SZ effect. The relevance of the tSZ effect as a galactic foreground has been ruled out by previous studies (see e.g. Hinshaw et al., 2007, also section 4.2). As we will show, however, the kSZ effect makes a significantly higher contribution. This is confirmed by an independent galactic kinetic SZ effect simulation made by Hajian et al. (2007), with whose results ours agree. Even though the galactic kSZ effect is more significant than the tSZ effect, we demonstrate by means of the optimally matched filter technique that it is still not a significant CMB foreground.

We extend our search by also investigating whether the second scattering of galactic kSZ effect photons could present a significant CMB polarisation foreground. The strength of the the

polarised signal due to Thomson scattering by galactic electrons is determined by the intensity of the incident quadrupole radiation in the rest frame of the electron. Hence we assess the importance of a polarised foreground by the intensity of the incident quadrupole radiation source.

We will show, that the polarisation signal due to the intrinsic CMB quadrupole is far more significant than that caused by secondary scattering of the kSZ induced quadrupole. In addition we also examined the relevance of the CMB quadrupole induced by the mildly relativistic motion of the galaxy in the CMB rest-frame. This effect, however, is known to be an order of magnitude smaller than the intrinsic CMB quadrupole (Hinshaw et al., 2007) hence, although it is slightly more relevant for polarisation production than the kSZ quadrupole, also negligible. The CMB quadrupole induced polarisation by galactic electrons has been shown to be an insignificant CMB polarisation foreground (Hirata et al., 2005). We confirm this result in sec. 4.5.2, where we demonstrate by means of a matched filter that no galactic signal can be detected even assuming an idealised experiment. Hence polarisation contributions due to the weaker galactic kSZ effect can safely be ignored as CMB polarisation foreground.

The structure of the paper is the following. In section 4.2 we give a brief description of the SZ effect, while in section 4.3 we describe the Thomson scattering theory and check for the relevance of the kSZ effect polarisation signal. Section 4.4 describes our simulation of the galactic SZ effect and the polarised Thomson scattering emission. In Section 4.5 we describe our attempt to measure the SZ and polarised Thomson scattering signature in our simulations. We draw conclusions in Section 4.6 and discuss how both the kSZ and the polarised Thomson signal can be ignored as CMB foregrounds.

4.2 The Sunyaev-Zeldovich effect

The SZ effect is a distortion of the CMB signal caused by the scattering of the CMB photons on moving free electrons (see Sunyaev & Zeldovich, 1972, 1980). There are two components of the SZ effect: the thermal SZ effect due to the electron thermal velocities and the kinetic SZ effect caused by the bulk motion of electrons in the CMB rest frame. The CMB spectrum distorted by the Compton scattering is given by

$$\begin{aligned} I(x) &= I_{CMB}(x) + \delta I_{tSZ}(x) + \delta I_{kSZ}(x) \\ &= i_0[i(x) + g(x)y - h(x)\overline{\tau\beta}], \end{aligned} \tag{4.1}$$

where $x = h\nu/(kT)$ is the dimensionless frequency. The CMB blackbody spectrum is

$$I_{CMB}(x) = i_0\, i(x), \tag{4.2}$$

with normalisation factor $i_0 = 2(kT_{CMB})^3/(hc)^2$ and spectral shape $i(x) = x^3/(e^x - 1)$. The second term on the right hand side of Eq. 4.1 describes the tSZ effect. This effect has a spectral shape given by

$$g(x) = \frac{x^4 e^x}{(e^x - 1)^2} \left(x \frac{e^x + 1}{e^x - 1} - 4 \right) , \tag{4.3}$$

and amplitude given by the Comptonisation parameter for a given line-of-sight (LOS),

$$y = \frac{\sigma_T}{m_e c^2} \int dl \, n_e(l) \, kT_e(l). \tag{4.4}$$

The last term on the right hand side of Eq. 4.1 represents the kSZ effect. It has the spectral shape

$$h(x) = \frac{x^4 e^x}{(e^x - 1)^2} \tag{4.5}$$

and depends on the LOS integral

$$\overline{\tau\beta} = \sigma_T \int dl \, n_e(l) \, \beta(l). \tag{4.6}$$

Here β is the velocity component along the LOS in units of the speed of light.

It is common practise to display CMB measurements in terms of temperature distortion maps. This is specially convenient for the kSZ effect, which can be interpreted as a frequency independent change to the original CMB temperature. The spectral distortions introduced by the kSZ effect are

$$I(x') \simeq I(x) + \left(\frac{\partial I}{\partial x'} \right)_{x'=x} (x' - x) = i_0 \left(i(x) - h(x) \frac{\delta T}{T_{CMB}} \right) , \tag{4.7}$$

and therefore identical to spectral distortions generated by a temperature change, to first order. Here $x' = \frac{h\nu}{kT'}$, where $T' = T_{CMB} + \delta T$ and $\delta T \ll T_{CMB}$. Comparing Eq. 4.1 and 4.7 suggest the identification $\overline{\tau\beta} = \delta T_{kSZ}/T_{CMB}$. In contrast, the tSZ spectral distortions cannot be described by a simple frequency-independent temperature change. However, for our galaxy the kSZ effect dominates by orders of magnitude over the tSZ effect, as we show in chapter 4.

Order of magnitude estimate of the Galactic thermal SZ effect

Previous works have ruled out the relevance of the thermal SZ effect as a foreground for the CMB (see Hinshaw et al., 2007). They estimate $y \simeq 2 \times 10^{-8}$ by assuming a maximal temperature, density and LOS distance in Eq. 4.4. Thus they argue that the SZ effect can safely be ignored as a diffuse contaminating foreground signal. Indeed the Galactic tSZ effect would produce a variation in temperature about three orders of magnitude smaller than the CMB

primary anisotropies, at most.

4.2.1 Order of magnitude estimate of the galactic kinematic SZ effect

We will now attempt an estimate on the kSZ signal strength. The variation in temperature due to the kSZ (in the CMB rest-frame) is given by $\delta T/T_{CMB} = \overline{\tau\beta}$ which is a function of the thermal electron density and the LOS components of the electron velocities in the CMB rest-frame (Eq. 4.6). As a rough estimate, we consider a homogeneous gas distribution with electron density $n_e \sim 0.1\text{cm}^{-3}$ (Cordes & Lazio, 2002), and a constant velocity of 371km/s (see Fixsen et al., 1996) all along the LOS, with a length $L = 20\,\text{kpc}$, through the galactic plane. Hence,

$$\overline{\tau\beta} = \delta T_{kSZ}/T_{CMB} \sim \sigma_T\, L\, n_e\, \beta \sim 4 \cdot 10^{-6}.$$

This toy scenario portrays how large the kSZ effect amplitude could maximally be in the direction of the galactic plane. Though still smaller than the CMB anisotropy signal, it is significantly greater than the thermal SZ effect (about two orders of magnitude). This motivates us to undertake a more precise analysis of this phenomenon by constructing a synthetic map of the galactic kSZ effect (see sec. 4.4.2) and to investigate whether it can be a non-negligible CMB foreground (see sec. 4.5).

4.3 Polarisation due to Thomson scattering

Polarisation due to Thomson scattering depends only on the quadrupole of the incoming radiation as is briefly demonstrated in the following.

The Q and U Stokes parameters due to Thomson scattering for each LOS are computed for a local coordinate system whose xy-plane is orthogonal to the LOS and whose z-direction points to the observer. To consistently compute the Stokes parameters for all directions on the sky we adopt the convention where the x-axis points in negative $\hat{\varphi}'$ and the y-axis in negative $\hat{\theta}'$ direction of the observer-centric coordinate system whose x′ axis points towards the galactic centre while the z′ axis points towards the galactic north pole. Assuming the usual θ and φ angles for the local coordinate system we have

$$Q^{TS} = \frac{3\sigma_T}{16\pi} \int dl\, n_e(l) \int d\Omega\, \sin^2\theta\, \cos 2\varphi\, I(\theta, \varphi, l), \tag{4.8}$$

$$U^{TS} = \frac{3\sigma_T}{16\pi} \int dl\, n_e(l) \int d\Omega\, \sin^2\theta\, \sin 2\varphi\, I(\theta, \varphi, l). \tag{4.9}$$

The terms $\sin^2\theta\,\cos 2\varphi = \sqrt{8\pi/15}\left(Y_2^2(\theta,\varphi) + Y_2^{-2}(\theta,\varphi)\right)$ and $\sin^2\theta\,\sin 2\varphi = -i\sqrt{8\pi/15}\left(Y_2^2(\theta,\varphi) - Y_2^{-2}(\theta,\varphi)\right)$ are linear combinations of l=2 spherical harmonics, i.e. the quadrupole (here spherical harmonics are denoted by $Y_l^m(\theta,\varphi)$). Hence only

the quadrupole part of $I(\theta, \varphi)$ survives the integration over the whole sphere:

$$\begin{aligned} \int d\Omega \, \sin^2\theta \, \cos 2\varphi \, I(\theta,\varphi) &= \sqrt{\frac{8\pi}{15}} \, (a_{22} + a_{2-2}) \\ &= \sqrt{\frac{32\pi}{15}} \mathrm{Re}\, a_{22} \end{aligned} \tag{4.10}$$

and similarly

$$\begin{aligned} \int d\Omega \, \sin^2\theta \, \sin 2\varphi \, I(\theta,\varphi) &= -i \sqrt{\frac{8\pi}{15}} \, (a_{22} - a_{2-2}) \\ &= \sqrt{\frac{32\pi}{15}} \mathrm{Im}\, a_{22}. \end{aligned} \tag{4.11}$$

Here, the a_{lm} are the spherical harmonic coefficients. We have made use of the property $a_{l\,-m} = -1^m a^*_{lm}$ of the real valued brightness distribution, with the asterix denoting complex conjugation.

4.3.1 Estimating the relevance of the polarised signal

Here, we asses the typical strength of the polarisation signal caused by second scattering of the kSZ photons. To do so we compare it to other possible sources of polarised radiation. In order to identify the dominant polarisation signal we only have to find the strongest quadrupole source.

Table 4.1 lists the total power of all possibly relevant quadrupole sources. Notice that other foregrounds like synchrotron or dust emission present even stronger quadrupoles, however, since they have frequency dependent brightness temperatures, they can, in principle, be removed. We see that the CMB quadrupole is by far the most significant contribution. The Doppler quadrupole due to Earths motion in the CMB rest-frame is negligible, while the quadrupole due to second scattering of the kSZ effect is even smaller.

We first perform an order of magnitude estimate to obtain the upper limit for the polarised signal due to the scattering of the CMB quadrupole by galactic thermal electrons:

We refer to the CMB power spectrum given by Hinshaw et al. (2007). In their table 7, they display the quantity $\Delta T_2^2 = 211 \mu K^2$. It is given by $\Delta T_l^2 = l(l+1)C_l/(2\pi)$, and $C_l = 1/(2l+1) \sum_{m=-l}^{l} |a_{lm}|^2$. For a rough upper limit estimate, we assume all quadrupole power to be concentrated on only the real part of $a_{22} = \sqrt{5C_2}$. Assuming a homogeneous thermal electron number density $n_e \sim 0.1\,\mathrm{cm}^{-3}$ (again following Cordes & Lazio, 2002, as in section 4.2.1) along a LOS of $L \sim 20\,\mathrm{kpc}$ (say towards the galactic centre) we get,

$$Q = \sigma_T \sqrt{\frac{3}{40\pi}} L \, n_e \, \mathrm{Re}\, a_{22} \simeq 2 \cdot 10^{-2} \, \mu\mathrm{K}. \tag{4.12}$$

Quadrupole source	C_2
CMB	$221\mu\mathrm{K}^2$
relat. Doppler effect	$3.45\mu\mathrm{K}^2$
kSZ effect	$10^{-2}\mu\mathrm{K}^2$

Table 4.1: Amplitude of the quadrupole moments in order of their significance. The relativistic Doppler effect quadrupole moment is calculated for $\beta \sim 1.2 \cdot 10^{-3}$. The CMB quadrupole given by Hinshaw et al. (2007) includes this value (i.e. they do not attempt to subtract it from the measured value). The kSZ quadrupole moment is obtained from our simulation in sec. 4.4.2. Other foregrounds with frequency dependent brightness temperatures like synchrotron or dust emission are assumed to be removed.

The polarised CMB intrinsic anisotropies have maximum amplitudes of $\sim$ 10% of the total CMB anisotropies whose maxima are typically around a few 100μK (see figure 15 of Page et al., 2007). Hence, the polarisation signal due to Thomson scattering on the galactic electrons from the CMB radiation (only a few $10^{-2}\,\mu$K) is likely to be undetectable on any Q or U maps. The much weaker kSZ contribution (see table 4.1) is thus likely to be an insignificant contamination to the CMB polarisation. This is supported by detailed computations of the Thomson scattering of the CMB quadrupole by galactic electrons performed by Hirata et al. (2005). The authors verify that the galactic Thomson signal is not a significant contamination to the intrinsic CMB polarisation.

Complementary to the arguments presented in Hirata et al. (2005), in sec. 4.5.2 we confirm by means of the matched filter technique applied to our simulations that the signal is not detectable, consequently neither is the one due to the second scattering of kSZ photons.

4.4 Simulations

4.4.1 The code

We modified the Hammurabi-code originally designed for simulating Galactic synchrotron emission, as described in chapter 3 and in (Waelkens et al., 2009a; Enßlin et al., 2006), to calculate the LOS integral given in Eq. 4.6 (for the kSZ effect) and in Eq. 4.8 and 4.9 (for the polarisation due to Thomson scattering). A detailed description of the codes workings is given in App. C.1.

Galaxy model

Two input models are needed, a model for the thermal electron distribution and a model for the galactic rotation curve.

1. For the electrons we again use the Cordes & Lazio (2002) NE2001 model, also described in Sec. 3.5.1.

2. For the galactic rotation curve we assume a constant value of 220 km/s above a galactocentric distance of 2 kpc. Below this distance the velocity falls off linearly to zero while approaching the galactic centre. This is an approximation for the observed rotation curve (see e.g. Klypin et al., 2002, and references therein), which should be adequate to determine whether the galactic kSZ effect can be detected.

4.4.2 Constructing the kSZ map

The velocity of each point of the galaxy with respect to the CMB rest-frame is subdivided into two components. The rotation velocity of the galaxy (β_{rot}) and the position-independent translation velocity of the galaxy (β_{trn}). The first quantity is obtained from our rotation curve model. The later quantity is obtained by subtracting our solar systems galactic rotation velocity vector (220 km/s in $l = \pi/2$ direction) from the measured total CMB frame velocity (371km/s in $l \simeq 1.47\pi$ and $b \simeq 0.27\pi$ direction, see Fixsen et al., 1996). Since the resulting β is small($\sim 10^{-3}$), we can safely ignore relativistic effects when adding velocities.

However, relativistic effects may need to be considered for the temperature transformation. So far we obtained the $\overline{\tau\beta} = \delta T/T_{CMB}$ sky in the CMB rest-frame. The relativistic temperature transformation is given by $\delta T_{obsf} = \delta T_{cmbf}\left[\gamma\left(1 + (\beta_{tot}\,\mu_{obsf})\right)\right]^{-1}$. Here μ_{obsf} is the cosine of the angle between the opposite of the CMB frame motion direction and the LOS in the observer rest-frame and $\gamma = (1-\beta^2)^{-1/2}$. The relativistic correction to the temperature is small, in the extreme a factor $\sim (1 \pm 10^{-3})$, which can be safely ignored, leaving $\delta T_{obsf} = \delta T_{CMBf}$. Thus to obtain the kSZ map we can neglect all relativistic effects.

Finally, we obtain the kSZ map by inserting our galaxy model in Eq. 4.6. The resulting map is shown in figure 4.1. Note the local interstellar medium features of the thermal electron density model (see sec. 4.4.1). We subtracted the monopole and dipole in accordance with the standard practise of subtracting the monopole and the relativistic-Doppler-effect induced dipole from maps displaying the CMB anisotropies. Our simulations show that this has a small effect, decreasing the maximum amplitude of the map by about 20%.

The maximum amplitudes of the simulated signal are of the order of μK, in accordance with the estimate obtained in section 4.2.1, and two orders of magnitude smaller than the CMB intrinsic anisotropies.

4.4.3 Constructing the polarised Thomson scattering maps

The expressions for the Q and U stokes parameters (Eqs. 4.8 and 4.9) assume that the negative z-axis of the coordinate system coincides with the LOS direction. Thus it is necessary to compute the appropriate a_{22} coefficient for each direction on the sky. This is done by rotating a set of a_{2m} coefficients, which are given in a certain coordinate system e.g. that in which the WMAP data are presented, to the proper coordinate system in which the negative z-axis is aligned with the LOS. The procedure for rotating a_{lm} coefficients is described in detail in Varshalovich et al.

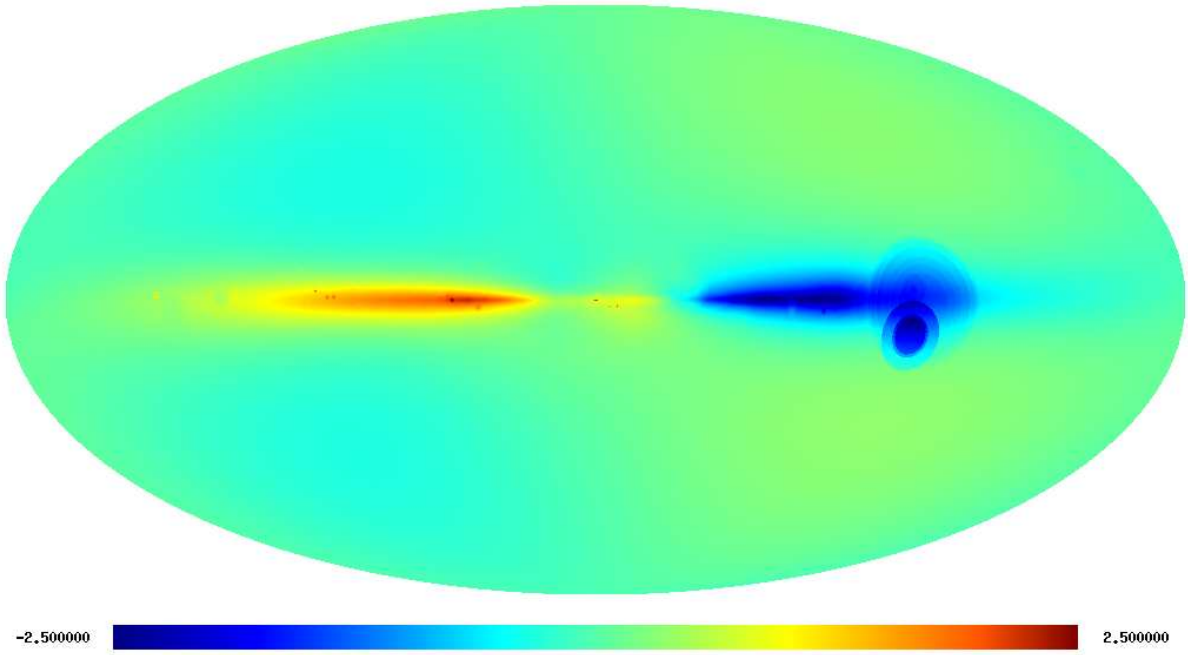

Figure 4.1: $\delta T = \overline{\tau\beta} \cdot T$ map in μK. The monopole and dipole components of the map have been subtracted in analogy to what typically is done for the observations (e.g. WMAP). Our simulation shows that the maximum amplitude of the map decreases by about 20% once the kSZ dipole is subtracted. Notice the features due to over dense or under dense regions in the local interstellar medium.

(1988) and de Oliveira-Costa et al. (2004). For completeness, we reproduce our special case in the appendix B.2. Having performed the rotation we may apply Eqs. 4.10 and 4.11 to each position on the sky, which after performing a LOS integral of the thermal electron density, finally allow us to compute Q and U, using Eqs. 4.8 and 4.9 respectively. The resulting full sky maps are shown in figures 4.2 and 4.3. The maximum amplitudes are $\sim 10^{-3}\,\mu$K, about one order of magnitude lower than our estimate in section 4.3. Out of the Q and U maps, the E and B mode spherical harmonic coefficients are obtained. Since most of the CMB polarisation power is in E modes, the B-modes signal of the polarised galactic Thomson scattering is more relevant as a CMB polarisation contamination than the corresponding E-mode signal. In sec. 4.5.2 we search for B-mode signal contamination by polarised galactic Thomson-scattering.

4.5 Filtering

In order to estimate the feasibility of a detection of the effects discussed above, we construct and apply an optimally matched filter to simulated data, where we probe for the galactic kSZ and galactic polarised Thomson scattering signatures.

The optimal matched filter was proposed for measuring radial bulk motion of galaxy clusters through their kSZ imprint (Haehnelt & Tegmark, 1996) and subsequently found a wide range

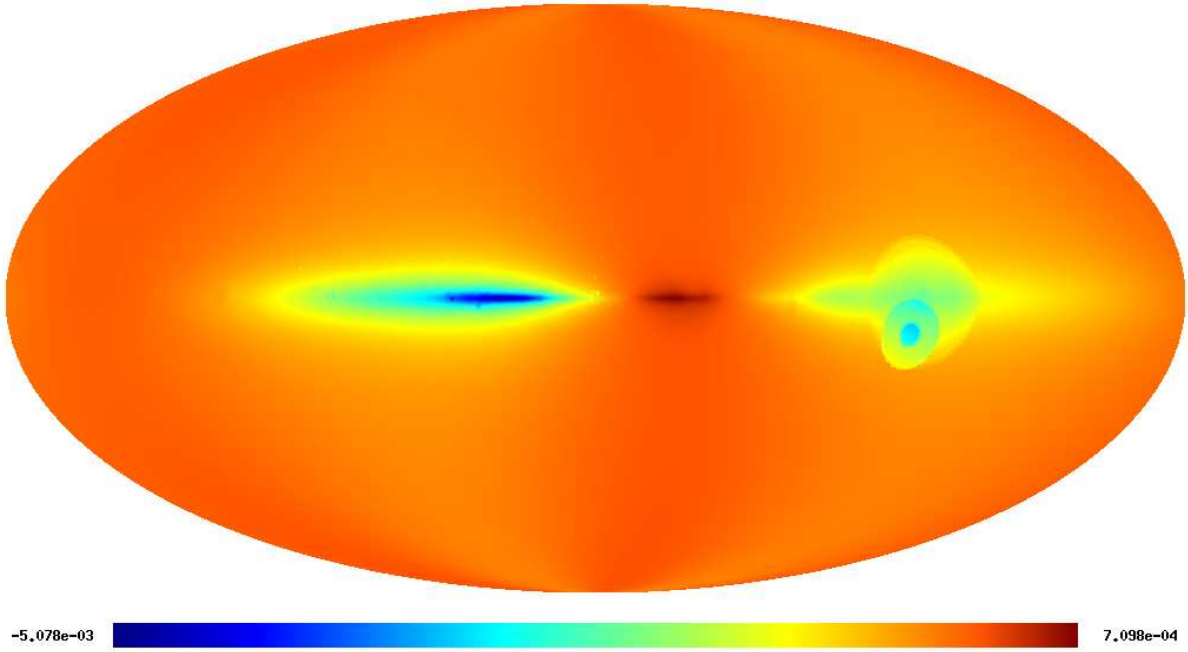

Figure 4.2: Stokes Q in μK.

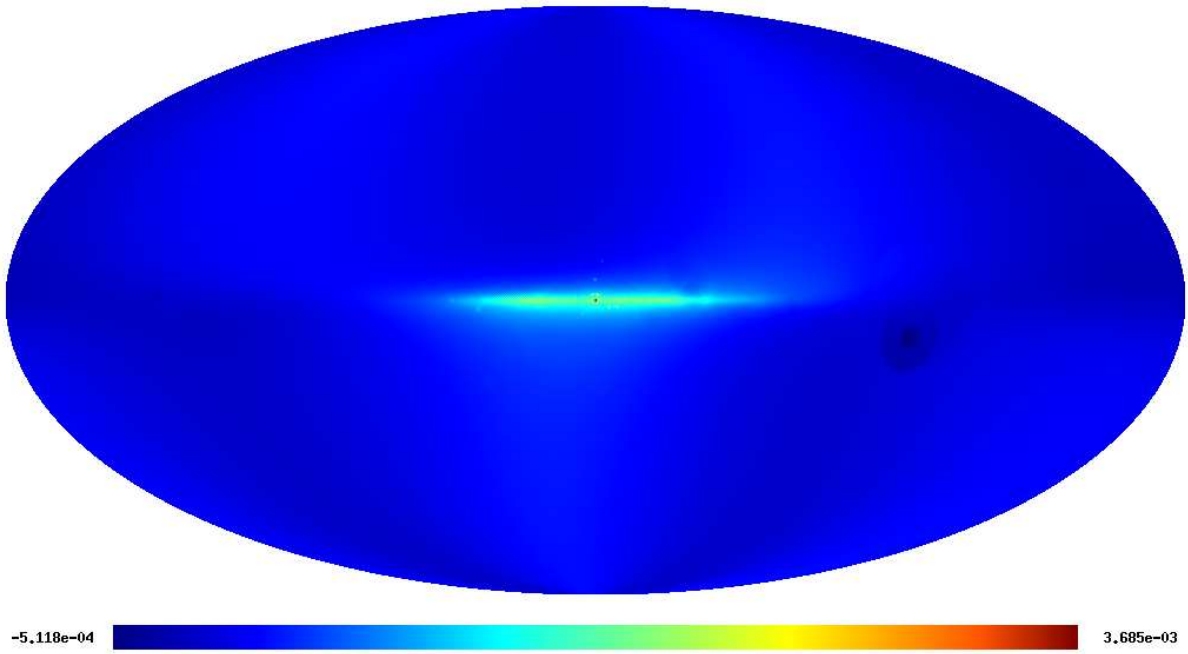

Figure 4.3: Stokes U in μK.

of applications in the literature, such as weak lensing and the RS effect (see e.g. Maturi et al., 2005, 2006). A scalar adaptive generalisation of the filter on the sphere was done by Schäfer et al. (2006), and later extended to allow non-azimuthally symmetric objects to be detected (McEwen et al., 2006). We use a similar approach to Schäfer et al. (2006). However, instead of convolving the CMB signal and the filter for various positions and orientations, we need only perform one convolution since we already know the position and orientation of our signal. Details are presented in the appendix B.1. The estimate of the maximum amplitude of the targeted signal is given by the convolution of the filter Ψ with the signal S

$$\overline{A} = \int d\Omega \, \Psi(\theta, \varphi) S(\theta, \varphi), \tag{4.13}$$

while the variance is

$$\sigma^2 \;\; = \;\; < \overline{A} >^2 - A^2 = \sum_l \sum_m C_l \, |\psi_{lm}|^2 \, . \tag{4.14}$$

Here ψ_{lm} is the spherical harmonic coefficient of the filter. The angular power spectrum of the noise (C_l) is either, in the kSZ case, the temperature angular power of the CMB plus instrumental Gaussian noise, or, in the polarised Thomson-scattering case, the B-mode angular power spectrum plus corresponding Gaussian instrumental noise. The filter is defined such that σ^2 is minimal while the bias $b = \langle \overline{A} \rangle - A = 0$ is zero.

4.5.1 Filtering on simulated data: galactic kSZ

We consider the ideal situation in which the only additional contribution to the CMB plus instrumental noise signal is the kSZ effect.

We do a simulation of the CMB sky with a sampling resolution of about 7 arcmin (corresponding to the HEALPix parameter NSIDE=512) and assume experimental characteristics expected for a Planck-like experiment, i.e. a resolution of 10 arcmin and a sensitivity of $5\,\mu$K/beam. Given that the structures of the simulated kSZ effect are mostly on larger scales (see figure 4.4), the sensitivity, instead of the resolution, is the more relevant instrumental characteristic here. We generate a kSZ map with the same sampling resolution, add it to the synthetic CMB sky and then convolve the map with a one degree Gaussian kernel. This smooths the sharp borders of the simulation and also ensures that our final map is properly sampled. The result is shown in figure 4.5, in which no evidence of the kSZ effect is visible.

As a signal template we take the same convolved kSZ map previously used in defining the data. This highly idealised approach (assuming a perfect signal template and no contamination by other Galactic emission sources) is suitable to determine the best possible filter performance.

The signal amplitude obtained by applying the filtering technique is $-10 \pm 21\mu$K, with the variance given by Eq. 4.14. The expected maximum amplitude of the kSZ map, the quantity

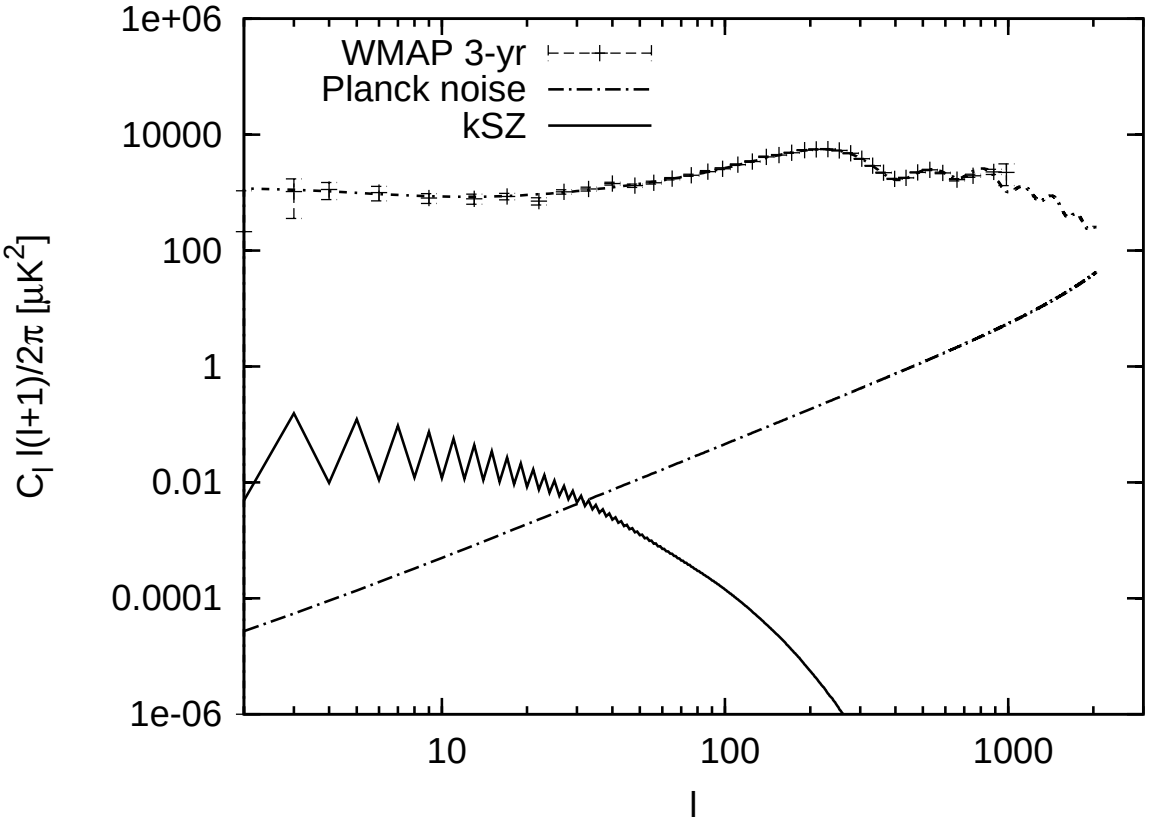

Figure 4.4: Comparing the CMB power spectrum to the simulated kSZ power spectrum. The saw like pattern for the kSZ effect power spectrum is due to the fact that even spherical harmonics are zero at the equator of the coordinate system, which in this case corresponds to the galactic plane. Hence odd modes will have more power.

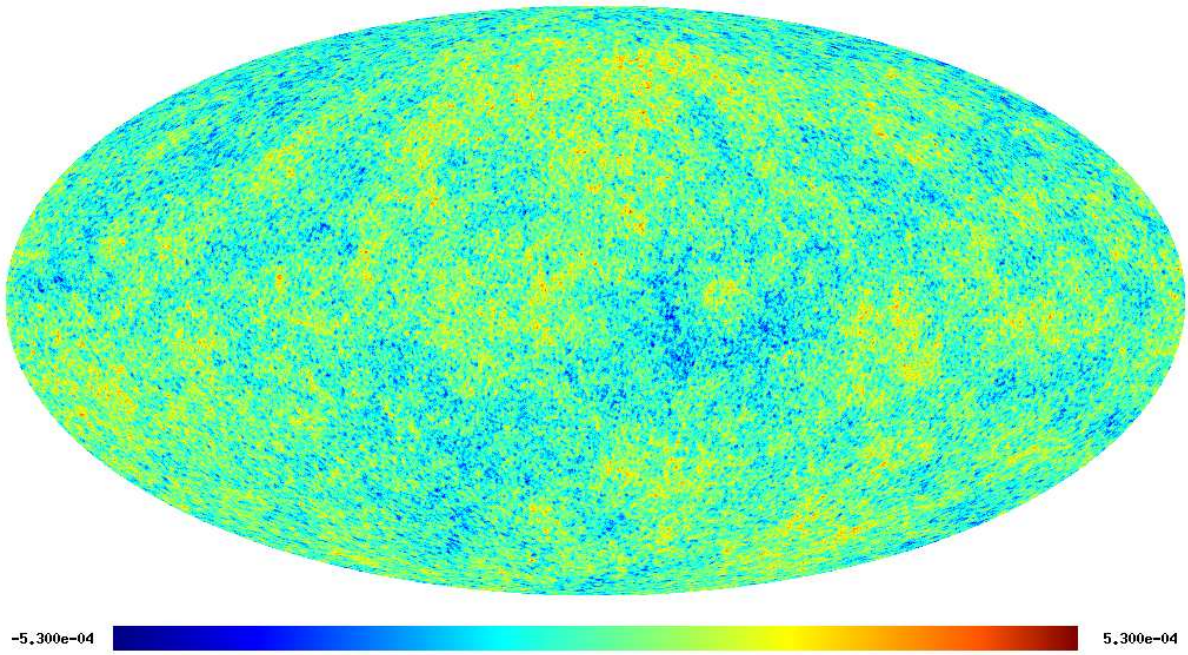

Figure 4.5: Simulated CMB sky contaminated by the simulated galactic kSZ effect.

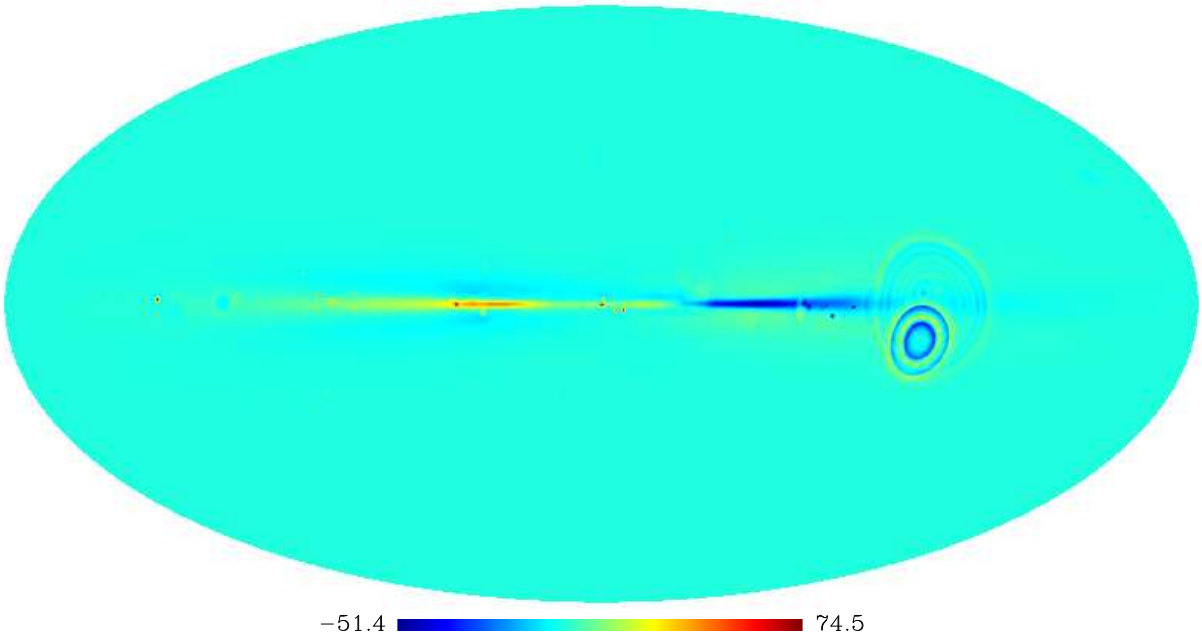

Figure 4.6: The optimally matched galactic kSZ filter. Note the features due to the local inter stellar medium components of the thermal electron density model (Cordes & Lazio, 2002).

we are estimating with the optimally matched filter, is 2.4μK, according to our model. Hence we have a signal-to-noise ratio of 0.1.

Although in this simulation no other foregrounds were present, no detection was possible, demonstrating that the galactic kSZ effect can be ignored as a CMB foreground.

4.5.2 Filtering on simulated data: the B-mode signal

The measurement of CMB B modes is the next cosmological challenge and would be very relevant for constraining inflationary models. The CMB polarised power is overwhelmingly in the E-modes, contrary the polarised galactic Thomson scattering. For this, our simulation shows a balance between the E and B-mode power on large scales, and a difference by at most one order of magnitude on smaller scales. This implies that the galactic B-mode contamination of the CMB is relatively stronger than the corresponding E-mode contamination. Therefore applying the same filtering technique as in sec. 4.5 we can investigate whether the polarised Thomson scattered B-mode signal is detectable and, if so, whether it is a relevant CMB foreground.

We use the predicted CMB BB power spectrum C_l^{BB} (as given by the CAMB code, Lewis et al., 2000) for a tensor-to-scalar ratio of 10^{-5} (following Hirata et al., 2005), plus the instrumental noise for a sensitivity of $7.6\,\mu$K/beam and a resolution of 30 arcmin (corresponding to polarisation instrumental characteristics of a Planck-like experiment), as the noise power spectrum in Eq. B.10. The tensor spherical harmonic coefficients $b_{lm}^{Thomson} \rightarrow \tau_{lm}$ for the B modes of our polarised galactic Thomson-scattering simulation are used as the spherical harmonic coefficients of our template.

This analogy to the previous case is permissible since C_l^{BB} is completely uncorrelated between each different mode (like the CMB temperature power spectrum), and the CMB B mode signal is uncorrelated with the galactic B mode signal.

We obtain an estimate of $-4 \cdot 10^{-3} \pm 5.8 \cdot 10^{-2}\mu$K, against the simulated signal amplitude of $1.6 \cdot 10^{-3}\mu$K. Since the achieved signal-to-noise ratio is ~ 0.03, the Thomson scattering by galactic thermal electrons is a negligible contribution to the CMB polarisation signal.

4.6 Chapter Conclusion

We have investigated the role of the galactic kinetic Sunyaev-Zeldovich effect as a CMB foreground, both for the total and polarised emission. This was done by means of an optimally matched filter based on a model of the signal and the expected noise power spectrum. The filter returns an unbiased estimate of the peak signal amplitude and is optimal in the sense that it provides the minimum variance for such a measure.

Regarding the non-polarised kinetic Sunyaev-Zeldovich emission as a CMB foreground, we found that, although the kinetic Sunyaev-Zeldovich effect is more relevant than the thermal

Sunyaev-Zeldovich effect, it is still not strong enough to be detectable by means of an optimally matched filter.

Our simulation for the kinetic Sunyaev-Zeldovich effect shows the signal to be concentrated on the galactic plane where the electron density is highest. The maximum amplitude of the simulated signal (the quantity estimated by the filtering procedure) is 2.4μK. Assuming an instrument with resolution of 10 arcmin and a sensitivity of $5\,\mu$K/beam, we obtain a signal amplitude of $-10 \pm 21\mu$K. Hence, no kinetic Sunyaev-Zeldovich effect signature could be detected.

We further demonstrate that the secondary scattering of kinetic Sunyaev-Zeldovich photons is negligible as a polarisation source. It is a weaker effect than the polarised emission due to Thomson scattering of CMB photons by galactic electrons. Again by means of the optimally matched filter technique, we determined that the latter effect is also irrelevant even as a CMB B-mode foreground, assuming a tensor to scalar ratio of 10^{-5} (where most of the polarised CMB power is in E-modes, and hence the B-modes are more easily contaminated). The polarised galactic Thomson-scattering signal is also concentrated on the galactic plane. The maximum amplitude of the simulated signal is $8 \cdot 10^{-4}\mu$K. Assuming an instrument with a resolution of 30 arcmin and a sensitivity of $7.6\,\mu$K/beam, we estimate an amplitude of $-4 \cdot 10^{-3} \pm 5.8 \cdot 10^{-2}\mu$K; thus no contamination of the CMB B-mode signal is detectable.

In conclusion, galactic foregrounds due to the kinetic Sunyaev-Zeldovich effect are a certainly existing, however perfectly camouflaged contamination of the CMB. Nevertheless, it is an expected physical effect which generates 1% temperature-fluctuation amplitude corrections on large scales, and thus should be taken into account when estimating the error of precision measurements as the Planck satellite will provide.

Chapter 5

Conclusion

In this work we developed and studied methods to obtain information on diffuse astrophysical magnetised plasmas at all observable scales. On small Galactic scales, magnetic turbulence can be analysed via Stokes correlators. With the HAMMURABI code models of the Galactic magnetised plasma can be confronted with observations of a wide range of its tracers, such as synchrotron emission, Faraday rotation, dispersion measure and UHECR deflection. The thermal electrons of the Galactic plasma provide a kinetic Sunyeaev Zeldovich effect signature in the CMB, which however, we show to be too low to be detected.

Stokes correlators

We demonstrated that the magnetic tension force power spectrum, a dynamically important characteristic of the turbulent magnetised plasma, can be extracted from linear combinations of the correlation functions of the observed total and polarised synchrotron radiation Stokes parameters. This is possible only under the mild assumptions of statistical isotropy, homogeneity and a power law energy distribution with a spectral index $p = 3$ of the cosmic-ray electrons originating the synchrotron radiation. Moreover we also assumed the data to be Faraday rotation free, which can generally be easily achieved at high observational frequencies.

It was also shown that in the specific case of a regular magnetic field superposed onto a statistically isotropic field, the tension force power spectrum can still be measured and additionally the magnetic power spectrum is also obtainable as a function of the observables. The scenario of a completely isotropic field added upon a regular field, as discussed, could be possible if the regular field is much weaker than the average random field. Proper numerical simulations for testing if these hypothesised conditions are realistic are still required.

The robustness of the developed estimator for the tension force power spectrum was tested on three-dimensional simulations. This permitted us to obtain the tension force power spectrum directly from the simulation box and thereafter compare it with corresponding estimates based on the two-dimensional mock observations derived from the simulation.

Two different scenarios were considered, the first being a magneto-hydro-dynamical simulation result, and the second being a divergence-free Gaussian random field realisation

(hence, not really a simulation) generated from the magnetic power spectrum computed from the first case. Though it is well known that turbulent magnetic fields do not present Gaussian statistics, the toy case is sufficient to show the estimators capacity of discriminating between essentially different dynamical scenarios. Moreover, the importance of the tension force spectrum is highlighted, as both cases have exactly the same magnetic power spectrum, and can therefore be discriminated only by higher order statistics like the tension force spectrum. We showed that the tension force spectrum estimator traces the real spectrum well, and can easily differentiate between our two test cases, paving the way for a future application to real data.

Hammurabi

The magnetised inter-stellar-medium also encompasses larger scales where turbulence no longer dictates the dynamics of the plasma. To specifically study the Galactic magnetised plasma as a whole, we developed a code called HAMMURABI to simulate the observation of Galactic magnetised plasma tracers. As shown, HAMMURABI is capable of simulating mock data of total and polarised synchrotron emission, rotation measure, dispersion measure, and free-free emission observations, as well as computing the expected small angular deflections of Ultra-High-Energy-Cosmic-Rays by the Galactic magnetic field. The confrontation of mock observations, resulting from the different three-dimensional Galactic magnetised plasma models with corresponding real observations imposes constraints on the properties of the magnetised inter-stellar-medium plasma, and permits to derive essential characteristics of it.

We have presented three works, which we took part in, attempting to constrain the properties of the Galactic magnetised plasma using the HAMMURABI code. The merits of testing the models against a wide range of different tracers, instead of only one sort of observation as is, for practical reasons, commonly done, has been demonstrated. One of these works, Sun et al. (2008), suggested that the scale-height of the Galactic thermal electron density should be larger by about a factor two than previously thought, such that the models would fit the observations in a theoretically plausible way. This finding was confirmed by a latter independent study by Gaensler et al. (2008).

The Galactic kinetic Sunyaev Zeldovich effect

In the last part of our work we studied the contamination of the cosmic microwave background by the Galactic kinetic Sunyaev-Zeldovich effect. Using an altered version of the HAMMURABI code, a simple model of the Galactic rotation curve, measurements of Earth's velocity in the cosmic microwave background rest frame, and the current state of the art model for Galactic thermal electron distribution, the Cordes & Lazio (2002) model, we simulated the expected Galactic kinetic Sunyaev-Zeldovich effect. To study its detectability we developed an altered version of an optimal linear matched filter for this signal, as well as for the mentioned work related to the detection of the Rees-Schiama effect (Maturi et al., 2007). Such filters return an estimate of the maximum amplitude of the signal with minimal variance, hence the designation 'optimal'.

We demonstrated that, although much more significant than the Galactic thermal Sunyaev-Zelovich effect, the Galactic kinetic Sunyaev-Zeldovich effect can safely be ignored as a cosmic microwave background contamination.

The maximum amplitude of the simulated signal is $2.4\,\mu$K. Assuming an instrument with resolution of 10 arcmin and a sensitivity of $5\,\mu$K/beam, we obtain a signal amplitude of $-10 \pm 21\mu$K. We stress that this result is obtained for very idealised conditions, assuming that all other foregrounds had been perfectly removed.

Moreover we investigated the importance of the second scattering of kinetic Sunyaev-Zeldovich photons on Galactic thermal electrons as a polarised foreground. It was demonstrated that the effect is negligible if compared to the Thomson scattering of cosmic microwave background quadrupole photons on the Galactic thermal electrons. The signal due to Thomson scattering, however, was shown, by means of the linear matched filter method we developed, not to be a significant polarisation contamination either. The maximum amplitude of the simulated signal being $8 \cdot 10^{-4}\mu$K, and assuming an instrument with a resolution of 30 arcmin and a sensitivity of $7.6\,\mu$K/beam, we estimated an amplitude of $-0.44 \pm 5.8 \cdot 10^{-2}\mu$K. Therefore no contamination of the CMB B-mode signal has to be feared, and conversely the kinetic Sunyaev-Zeldovich effect cannot be used as a probe for the Galactic thermal electron density.

5.1 Outlook

A considerable fraction of the work presented in this dissertation relies on the availability of radio observations. Present data will be hugely enriched by a number of powerful radio observatories, such as LOFAR, SKA and forerunners thereof, scheduled to begin operations in the coming years. This should provide fertile ground for potential future applications and extensions of the Stokes correlators method as well as of the HAMMURABI code, as presented in the following.

Stokes correlators

It would be critical for an application of the Stokes correlators method to obtain observations of a region where isotropy and statistical homogeneity of the magnetic turbulence hold, at least approximatively.

The next logical step is thus to ascertain if such conditions are already satisfied in available polarised radio observations of galaxy clusters. Potential deviations from the optimal scenario and their effect on the tension force power spectrum estimator could then be studied on numerical simulations which mimic the conditions in the target object.

Even if current data do not yet allow for an application of our method, the unprecedented resolution and sensitivity of next generation radio observatories should present ample opportunity to probe the ISM and the ICM with the Stokes correlators method.

A further and more ambitious step would be to extend the approach used for deriving the Stokes correlators to other sorts of observables such as dust emission or dust absorption.

Upcoming telescopes such as ALMA should provide unprecedented resolution in mm-wavelength observations, driving the need to develop analysis tools to properly explore these data.

The HAMMURABI code

In its current incarnation the HAMMURABI code is suitable to be applied to a number of existing problems.

In Sun et al. (2008) we focused on global magnetised ISM modelling, while ignoring the local inter-stellar-medium features,. However, a large fraction of the sky at radio frequencies is dominated by the North Polar Spur, thought to be a supernova remnant, and the Fan, particularly in polarised emission. An analysis of these local features, similar to the one done for the global ISM, would give us clues into the inner workings of the Galaxy, which is permeated by similar supernovae remnants, believed to be the stirring mechanisms of dynamos and MHD turbulence. Furthermore, our understanding of the local features as foregrounds would greatly benefit polarised CMB science.

Moreover HAMMURABI high resolution simulations can be used for feasibility studies of experiments such as SKA, LOFAR. The simulation outputs allow proposed data analysis to be tested prior to the telescopes real observations.

It was mentioned that the assumption of a power-law spectral index for the cosmic-ray electrons does not hold over large frequency ranges of the synchrotron spectrum. Therefore implementing the capacity to handle any cosmic-ray energy spectrum would be required. Although this would imply much longer computation times, upcoming CMB polarisation experiments might require such refinements of the simulations.

A currently ongoing expansion of the Hammurabi code is the implementation of dust absorption and emission physics, given the wealth of total and polarised data in mm-wavelengths expected from telescopes such as Planck, ALMA and optical/infra-red ground-based observations of polarised starlight. Inference of Galactic magnetic field properties from dust absorption data is more common in the literature than the theoretically more difficult polarised dust emission problem and would therefore be performed first. Dust physics allows us to constrain the magnetic field independently of the cosmic ray electron distribution (as is the case in synchrotron analysis).

Several new techniques for magnetised ISM structure inference have been developed and could also be implemented in the HAMMURABI code. Methods such as atom alignment measurements (Yan & Lazarian, 2008a) use polarised spectroscopy to measure the full magnetic field vector using the Doppler shift to help determine the spatial location of that same vector. The chance of obtaining three dimensional measurements, instead of line-of-sight integrals such as synchrotron flux observations, presents outstanding opportunities for understanding the magnetised ISM.

Faraday tomography (Brentjens & de Bruyn, 2005) is another novel technique being increasingly used. Here a multi-frequency polarised synchrotron observation permits to study

the relative distribution of synchrotron-emitting and Faraday-rotating regions along the line-of-sight. HAMMURABI simulations take into account differential Faraday rotation, as well as beam depolarisation and can therefore be used to generate detailed Faraday tomography mock observations of the Galactic magnetised plasma, which permits to study many properties of the ISM.

Diffuse magnetised plasmas are ever more present in modern astrophysics. Their comprehension is of importance for scientific problems ranging from the understanding of small scale magnetic turbulence in the magnetised inter-stellar-medium and intra-cluster-medium, star formation, dynamics of plasma processes of the intra-cluster-medium to the determination of foregrounds of the cosmic microwave background radiation.

Appendix A

Stokes correlators

A.1 Synchrotron Emission and the Stokes Parameters

A spatially homogeneous, pitch-angle-isotropic and power-law distributed in energy relativistic-electron population is assumed [Eq. 2.9], The resulting synchrotron emission is partially linearly polarised. Its intensity and polarisation depend solely on the magnitude and orientation of the magnetic field $\vec{B}_\perp$ projected onto the plane perpendicular to the line of sight and on the electron distribution [Eq. 2.9].

The synchrotron emissivity (i.e., power per unit volume per frequency per solid angle) is usually subdivided into two components, respectively perpendicular and parallel to $\vec{B}_\perp$: following Rybicki & Lightman (1979),

$$\begin{aligned} j_\perp(\omega, \vec{x}) &= [F(p) + G(p)]\, \omega^{(1-p)/2} |\vec{B}_\perp(\vec{x})|^{(p+1)/2} \\ j_\parallel(\omega, \vec{x}) &= [F(p) - G(p)]\, \omega^{(1-p)/2} |\vec{B}_\perp(\vec{x})|^{(p+1)/2}, \end{aligned} \tag{A.1}$$

where $\omega = 2\pi\nu$, ν is the observation frequency, $\vec{x}$ is the spatial position, p is the spectral index of the electron distribution [Eq. 2.9] and

$$\begin{aligned} F(p) &= \frac{\sqrt{3}\, e^3}{32\pi^2 m_e c^2} \left(\frac{2m_e c}{3e}\right)^{(1-p)/2} C \\ &\quad \times \Gamma\left(\frac{p}{4} - \frac{1}{12}\right) \frac{2^{(p+1)/2}}{p+1} \Gamma\left(\frac{p}{4} + \frac{19}{12}\right), \\ G(p) &= \frac{\sqrt{3}\, e^3}{32\pi^2 m_e c^2} \left(\frac{2m_e c}{3e}\right)^{(1-p)/2} C \\ &\quad \times \Gamma\left(\frac{p}{4} - \frac{1}{12}\right) 2^{(p-3)/2} \Gamma\left(\frac{p}{4} + \frac{7}{12}\right), \end{aligned} \tag{A.2}$$

where m_e is the electron mass, e is its charge, c is the speed of light, and C is the prefactor of the electron distribution [Eq. 2.9].

The specific intensity I and the polarised specific intensity PI are given by the following line-of-sight integrals (see Burn, 1966):

$$\begin{aligned} \mathrm{I}(\omega, \vec{x}_\perp) &= \int_{\text{there}}^{\text{here}} dz \left[j_\perp(\omega, \vec{x}) + j_\parallel(\omega, \vec{x}) \right], \\ \mathrm{PI}(\omega, \vec{x}_\perp) &= \int_{\text{there}}^{\text{here}} dz \left[j_\perp(\omega, \vec{x}) - j_\parallel(\omega, \vec{x}) \right] e^{-2i\chi(\vec{x})}, \end{aligned} \tag{A.3}$$

where z is the line-of-sight coordinate, $\vec{x}_\perp = (x, y)$ is the position vector in the plane of the sky (perpendicular to the line of sight) and the polarisation angle is given by

$$\chi(\vec{x}) = \chi_0(\vec{x}) + \lambda^2 \mathrm{RM}(\vec{x}), \tag{A.4}$$

where $\lambda = c/\nu$ is wavelength of the observed emission, the intrinsic polarisation angle is

$$\chi_0(\vec{x}) = \tan^{-1} \frac{B_y}{B_x}, \tag{A.5}$$

and the Faraday rotation measure

$$\mathrm{RM}(\vec{x}) = \frac{e^3}{2\pi m_e^2 c^4} \int_{\text{there}}^{\text{here}} dz\, n_{\text{th}e}(\vec{x}) B_z(\vec{x}), \tag{A.6}$$

where $n_{\text{th}e}$ is the density of thermal electrons and B_z the projection of the magnetic field on the line of sight.

The Stokes parameters are now defined as follows

$$I = \int d\Omega\, \mathrm{I}, \qquad Q - iU = \int d\Omega\, \mathrm{PI}, \tag{A.7}$$

where the integration is over the solid angle of the angular resolution element (the observational beam). If the spectral index is taken to be $p = 3$ and the Faraday rotation in Eq. A.4 is assumed to be negligible (as discussed in Sect. 2.4.3), the Stokes parameters depend quadratically on the components of the magnetic field perpendicular to the line of sight, $B_x = B_\perp \cos\chi_0$ and $B_y = B_\perp \sin\chi_0$. Indeed, using the above definitions, we get

$$\begin{aligned} I &= 2F(3)\, \omega^{-1} \int d\Omega \int_{\text{there}}^{\text{here}} dz \left(B_x^2 + B_y^2 \right), \\ Q &= 2G(3)\, \omega^{-1} \int d\Omega \int_{\text{there}}^{\text{here}} dz \left(B_x^2 - B_y^2 \right), \\ U &= 2G(3)\, \omega^{-1} \int d\Omega \int_{\text{there}}^{\text{here}} dz\, 2 B_x B_y. \end{aligned} \tag{A.8}$$

From these formulae, we recover the analytically convenient definitions of the Stokes

parameters, Eq. 2.10, by dropping the dimensional prefactors and the integration over the angular resolution element and normalising the integrals by the depth of the emission region.

Somewhat more generally, for arbitrary p, but still neglecting the Faraday rotation, we have

$$\begin{aligned} I &= 2F(p)\,\omega^{(1-p)/2} \int d\Omega \int_{\text{there}}^{\text{here}} dz \left(B_x^2 + B_y^2\right)^{(p-3)/4} \left(B_x^2 + B_y^2\right), \\ Q &= 2G(p)\,\omega^{(1-p)/2} \int d\Omega \int_{\text{there}}^{\text{here}} dz \left(B_x^2 + B_y^2\right)^{(p-3)/4} \left(B_x^2 - B_y^2\right), \\ U &= 2G(p)\,\omega^{(1-p)/2} \int d\Omega \int_{\text{there}}^{\text{here}} dz \left(B_x^2 + B_y^2\right)^{(p-3)/4} 2B_x B_y. \end{aligned} \tag{A.9}$$

These formulae are the basis for Eq. 2.39.

A.2 Fourth-Order Correlation Tensor and Its Representation in Terms of Stokes Correlators

In this Appendix, we derive the general form of the 4th-order correlation tensor $C_{ij,mn}$ [Eq. 2.12] for a statistically homogeneous and isotropic magnetic field and show what part of the relevant statistical information can be recovered using Stokes correlators.

A.2.1 Symmetries and the General Form of $C_{ij,mn}$

In Eq. 2.33, the tensor $C_{ij,mn}$ is written in Fourier space in terms of the mean field $\overline{B}_i$ and of the second-, 3rd-, and 4th-order correlation tensors of the fluctuating field b_i, denoted $c_{i,m}$, $c_{ij,m}$ and $c_{ij,mn}$. Each of these correlation tensors depends on a certain number of scalar correlation functions (see, e.g., Robertson, 1940). This number can be constrained if we take into account some intrinsic properties of correlation tensors (permutation of indices), of the field they are constructed from (it is a real, divergence-free field), and additional symmetries we assume (homogeneity and isotropy). Let us implement these constraints. The procedure is least cumbersome when applied to the second-order correlation tensor. We will explain it in detail on this example and then proceed analogously with the 3rd- and 4th-order correlators. All further calculations will be in Fourier space, but exactly analogous calculations can be done in position space if it is necessary to compute position-space correlators.

Second-Order Correlation Tensor

For a statistically isotropic field, the second-order correlation tensor depends on three scalar functions—this is shown by constructing $c_{i,m}$ out of all possible isotropic second-rank tensors. In three dimensions, the available building blocks for these tensors are δ_{im}, ϵ_{imp} and $\hat{k}_i$, the unit

vector in the direction of $\vec{k}$. Therefore,

$$c_{i,m}(\vec{k}) = \frac{1}{2}\left[m_1\delta_{im} + m_2\hat{k}_i\hat{k}_m\right] + im_3\epsilon_{imp}\hat{k}_p, \tag{A.10}$$

where the scalar coefficients m_1, m_2, m_3 can only depend on $k = |\vec{k}|$.

Since $b_i(\vec{k})$ is a Fourier transform of a real function, we must have $b_i(-\vec{k}) = b_i^*(\vec{k})$, whence

$$c_{i,m}(-\vec{k}) = c_{i,m}^*(\vec{k}). \tag{A.11}$$

It is easy to see that this implies that m_1, m_2 and m_3 are real (the factor of i in front of m_3 was chosen deliberately to arrange for this outcome).

Since $c_{i,m}$ is a correlation tensor, it has a symmetry with respect to permutation of its indices:

$$c_{m,i}(\vec{k}) = \langle b_m^*(\vec{k})b_i(\vec{k})\rangle = c_{i,m}^*(\vec{k}). \tag{A.12}$$

This does not bring any new information beyond the reality of m_1, m_2 and m_3. Finally, the magnetic field is solenoidal, $k_i b_i(\vec{k}) = 0$, so we must have

$$k_i c_{i,m} = k_m c_{i,m} = 0. \tag{A.13}$$

This gives $m_2 = -m_1$, so the general form of the second-order correlation tensor is

$$c_{i,m}(\vec{k}) = \frac{1}{2}\, m_1(k)\left(\delta_{im} - \hat{k}_i\hat{k}_m\right) + im_3(k)\epsilon_{imp}\hat{k}_p, \tag{A.14}$$

i.e., it depends only on two scalar functions. If we take the trace of this tensor, we obtain the magnetic-energy power spectrum [Eq. 2.2]:

$$M(k) = 4\pi k^2 c_{i,i}(k) = 4\pi k^2 m_1(k), \tag{A.15}$$

so we do not need to know m_3 if we are only interested in the power spectrum. Vogt & Enßlin (2003, 2005) used this property to propose a way to measure the magnetic power spectrum solely in terms of the scalar correlation function of the Faraday rotation measure associated with a given magnetic-field distribution: although only one scalar function was available this way, assuming isotropy and restricting one's attention to a particular quantity of physical interest made it possible to make do with incomplete information. We follow the same basic philosophy in this paper, primarily as applied to the 4th-order statistics.

Note that m_3 is a measure of reflection (parity, or mirror) non-invariance of the magnetic field. If $m_3 \neq 0$, the field has helicity. If we demand mirror symmetry of the field,

$$c_{i,m}(-\vec{k}) = c_{i,m}(\vec{k}), \tag{A.16}$$

we find $m_3 = 0$. We will see that normally we do not have to make this assumption because in many cases, the mirror-noninvariant terms are not present in the quantities of interest (as was the case with the power spectrum).

Third-Order Correlation Tensor

Analogously to the above, we construct the general isotropic 3rd-order tensor as follows

$$\begin{aligned} c_{ij,m}(\vec{k}) &= i\left(a_1\delta_{ij}\hat{k}_m + a_2\delta_{im}\hat{k}_j + a_3\delta_{jm}\hat{k}_i + a_4\hat{k}_i\hat{k}_j\hat{k}_m\right) + a_5\epsilon_{ijm} \\ &\quad + a_6\epsilon_{ijp}\hat{k}_p\hat{k}_m + a_7\epsilon_{imp}\hat{k}_p\hat{k}_j + a_8\epsilon_{jmp}\hat{k}_p\hat{k}_i, \end{aligned} \tag{A.17}$$

where $a_1, \ldots, a_8$ are functions of $k = |\vec{k}|$ only.

Reality of the fields h_{ij} and b_m implies

$$c_{ij,m}(-\vec{k}) = c^*_{ij,m}(\vec{k}), \tag{A.18}$$

whence $a_1, \ldots, a_8$ are all real.

Permutation symmetry,

$$c_{ji,m}(\vec{k}) = c_{ij,m}(\vec{k}), \tag{A.19}$$

implies $a_2 = a_3$, $a_5 = a_6 = 0$, and $a_7 = a_8$.

Solenoidality of the magnetic field implies

$$k_m c_{ij,m}(\vec{k}) = 0, \tag{A.20}$$

whence $a_1 = 0$ and $a_4 = -2a_2$.

Thus, the general form of the 3rd-order correlation tensor is

$$\begin{aligned} c_{ij,m}(\vec{k}) &= ia_2(k)\left(\delta_{im}\hat{k}_j + \delta_{jm}\hat{k}_i - 2\hat{k}_i\hat{k}_j\hat{k}_m\right) \\ &\quad + a_7(k)\left(\epsilon_{imp}\hat{k}_p\hat{k}_j + \epsilon_{jmp}\hat{k}_p\hat{k}_i\right). \end{aligned} \tag{A.21}$$

Fourth-Order Correlation Tensor

In the 4th order, the number of terms in the general tensor becomes quite large. Constructing this general form out of the usual building blocks, δ_{ij}, $\hat{k}_i$ and ϵ_{ijm}, we get, via straightforward

combinatorics,

$$\begin{aligned} c_{ij,mn}(\vec{k}) &= c_1\delta_{ij}\delta_{mn} + c_2\delta_{im}\delta_{jn} + c_3\delta_{in}\delta_{jm} \\ &+ c_4\delta_{ij}\hat{k}_m\hat{k}_n + c_5\delta_{mn}\hat{k}_i\hat{k}_j \\ &+ c_6\delta_{im}\hat{k}_j\hat{k}_n + c_7\delta_{in}\hat{k}_j\hat{k}_m + c_8\delta_{jm}\hat{k}_i\hat{k}_n + c_9\delta_{jn}\hat{k}_i\hat{k}_m \\ &+ c_{10}\hat{k}_i\hat{k}_j\hat{k}_m\hat{k}_n \\ &+ i\Big(c_{11}\epsilon_{ijm}\hat{k}_n + c_{12}\epsilon_{ijn}\hat{k}_m + c_{13}\epsilon_{imn}\hat{k}_j + c_{14}\epsilon_{jmn}\hat{k}_i \\ &+ c_{15}\epsilon_{ijp}\hat{k}_p\delta_{mn} + c_{16}\epsilon_{mnp}\hat{k}_p\delta_{ij} + c_{17}\epsilon_{imp}\hat{k}_p\delta_{jn} \\ &+ c_{18}\epsilon_{inp}\hat{k}_p\delta_{jm} + c_{19}\epsilon_{jmp}\hat{k}_p\delta_{in} + c_{20}\epsilon_{jnp}\hat{k}_p\delta_{im} \\ &+ c_{21}\epsilon_{ijp}\hat{k}_p\hat{k}_m\hat{k}_n + c_{22}\epsilon_{mnp}\hat{k}_p\hat{k}_i\hat{k}_j + c_{23}\epsilon_{imp}\hat{k}_p\hat{k}_j\hat{k}_n \\ &+ c_{24}\epsilon_{inp}\hat{k}_p\hat{k}_j\hat{k}_m + c_{25}\epsilon_{jmp}\hat{k}_p\hat{k}_i\hat{k}_n + c_{26}\epsilon_{jnp}\hat{k}_p\hat{k}_i\hat{k}_m\Big), \end{aligned} \tag{A.22}$$

where $c_1, \ldots, c_{26}$ are functions of $k = |\vec{k}|$ only. Note that there are no terms of the form $\epsilon_{ijp}\hat{k}_p\epsilon_{mnq}\hat{k}_q$ because

$$\begin{aligned} \epsilon_{ijp}\epsilon_{mnq} &= \delta_{im}\delta_{jn}\delta pq + \delta_{in}\delta jq\delta_{pm} + \delta_{iq}\delta jm\delta_{pn} \\ &- \delta_{im}\delta_{jq}\delta_{pn} - \delta_{in}\delta_{jm}\delta pq - \delta_{iq}\delta_{jn}\delta_{pm}, \end{aligned} \tag{A.23}$$

so such terms are already present in the general form we have constructed.

Reality of the field $h_{ij} = b_i b_j$ implies

$$c_{ij,mn}(-\vec{k}) = c^*_{ij,mn}(\vec{k}), \tag{A.24}$$

whence $c_1, \ldots, c_{26}$ are all real.

There are three permutation symmetries:

$$c_{ji,mn}(\vec{k}) = c_{ij,mn}(\vec{k}) \tag{A.25}$$

gives $c_2 = c_3$, $c_6 = c_8$, $c_7 = c_9$, $c_{11} = c_{12} = c_{15} = c_{21} = 0$, $c_{13} = c_{14}$, $c_{17} = c_{19}$, $c_{18} = c_{20}$, $c_{23} = c_{25}$, $c_{24} = c_{26}$,

$$c_{ij,nm}(\vec{k}) = c_{ij,mn}(\vec{k}), \tag{A.26}$$

gives additionally $c_6 = c_7$, $c_8 = c_9$, $c_{13} = c_{14} = c_{16} = c_{22} = 0$, $c_{17} = c_{18}$, $c_{19} = c_{20}$, $c_{23} = c_{24}$, $c_{25} = c_{26}$, and, finally,

$$c_{mn,ij}(\vec{k}) = c^*_{ij,mn}(\vec{k}) \tag{A.27}$$

gives $c_4 = c_5$.

Assembling all this information, we find that the general 4th-order correlation tensor only depends on 7 scalar functions:

$$\begin{aligned} c_{ij,mn}(\vec{k}) &= c_1(k)\delta_{ij}\delta_{mn} + c_2(k)\left(\delta_{im}\delta_{jn} + \delta_{in}\delta_{jm}\right) \\ &\quad + c_4(k)\left(\delta_{ij}\hat{k}_m\hat{k}_n + \delta_{mn}\hat{k}_i\hat{k}_j\right) \\ &\quad + c_6(k)\left(\delta_{im}\hat{k}_j\hat{k}_n + \delta_{in}\hat{k}_j\hat{k}_m + \delta_{jm}\hat{k}_i\hat{k}_n + \delta_{jn}\hat{k}_i\hat{k}_m\right) \\ &\quad + c_{10}(k)\hat{k}_i\hat{k}_j\hat{k}_m\hat{k}_n \\ &\quad + ic_{17}(k)\left(\epsilon_{imp}\hat{k}_p\delta_{jn} + \epsilon_{inp}\hat{k}_p\delta_{jm}\right. \\ &\qquad\qquad \left. + \epsilon_{jmp}\hat{k}_p\delta_{in} + \epsilon_{jnp}\hat{k}_p\delta_{im}\right) \\ &\quad + ic_{23}(k)\left(\epsilon_{imp}\hat{k}_p\hat{k}_j\hat{k}_n + \epsilon_{inp}\hat{k}_p\hat{k}_j\hat{k}_m\right. \\ &\qquad\qquad \left. + \epsilon_{jmp}\hat{k}_p\hat{k}_i\hat{k}_n + \epsilon_{jnp}\hat{k}_p\hat{k}_i\hat{k}_m\right). \end{aligned} \tag{A.28}$$

A.2.2 Observables in the Case of Zero Mean Field

Let us first examine the case $\overline{B} = 0$, so we are only concerned with the 4th-order statistics. We will need explicit expressions for the coordinate-dependent components of the tensor $c_{ij,mn}$ in terms of the coordinate-invariant functions c_1, c_2, c_4, c_6, c_{10}, c_{17} and c_{23} [Eq. A.28]. As the polarised emission data on the magnetic field arrives in the form of line-of-sight integrals (Sect. 2.4.4), we have to set $k_z = 0$ everywhere—no information on the field variation in this direction is available. However, because of the assumed isotropy, the dependence of the invariant scalar functions on $k_\perp = |\vec{k}_\perp|$ contains the same information as their dependence on $k = |\vec{k}|$. Let us denote by φ the angle between $\vec{k}_\perp$ and the x axis. This means that we set $\hat{\vec{k}} = (\cos\varphi, \sin\varphi, 0)$. Then the components perpendicular to the line of sight are

$$\begin{aligned} c_{xx,xx}(\vec{k}_\perp) &= c_1 + 2c_2 + (2c_4 + 4c_6)\cos^2\varphi + c_{10}\cos^4\varphi, \\ c_{yy,yy}(\vec{k}_\perp) &= c_1 + 2c_2 + (2c_4 + 4c_6)\sin^2\varphi + c_{10}\sin^4\varphi, \\ c_{xx,yy}(\vec{k}_\perp) &= c_1 + c_4 + c_{10}\sin^2\varphi\cos^2\varphi, \\ c_{xy,xy}(\vec{k}_\perp) &= c_2 + c_6 + c_{10}\sin^2\varphi\cos^2\varphi, \\ c_{xx,xy}(\vec{k}_\perp) &= (c_4 + 2c_6)\cos\varphi\sin\varphi + c_{10}\cos^3\varphi\sin\varphi, \\ c_{yy,xy}(\vec{k}_\perp) &= (c_4 + 2c_6)\cos\varphi\sin\varphi + c_{10}\cos\varphi\sin^3\varphi. \end{aligned} \tag{A.29}$$

These are the only components of $c_{ij,mn}$ that are directly sampled by the polarised emission. The components parallel to the line of sight are

$$\begin{aligned} c_{zz,zz}(\vec{k}_\perp) &= c_1 + 2c_2, \\ c_{xx,zz}(\vec{k}_\perp) &= c_1 + c_4 \cos^2\varphi, \\ c_{yy,zz}(\vec{k}_\perp) &= c_1 + c_4 \sin^2\varphi, \\ c_{xz,xz}(\vec{k}_\perp) &= c_2 + c_6 \cos^2\varphi, \\ c_{yz,yz}(\vec{k}_\perp) &= c_2 + c_6 \sin^2\varphi, \\ c_{xz,yz}(\vec{k}_\perp) &= c_6 \sin\varphi\cos\varphi. \end{aligned} \tag{A.30}$$

Information about these components can only be obtained by relying on the isotropy assumption as they are expressed in terms of the same invariant scalar functions as the perpendicular components. Note that setting $k_z = 0$ has led to all information being lost about the mirror-asymmetric part of the tensor, so no quantity involving c_{17} or c_{23} can ever be reconstructed from polarised emission.

Stokes Correlators

Using Eq. A.29 and the expressions for the Stokes correlators given by Eq. 2.15, we get

$$\begin{aligned} \Sigma_{II}(\vec{k}_\perp) &= 4\,(c_1 + c_2 + c_4 + c_6) + c_{10}, \\ \Sigma_{QQ}(\vec{k}_\perp) &= 4\,(c_2 + c_6) + c_{10}\cos^2 2\varphi, \\ \Sigma_{UU}(\vec{k}_\perp) &= 4\,(c_2 + c_6) + c_{10}\sin^2 2\varphi, \\ \Sigma_{IQ}(\vec{k}_\perp) &= (2c_4 + 4c_6 + c_{10})\cos 2\varphi, \\ \Sigma_{IU}(\vec{k}_\perp) &= (2c_4 + 4c_6 + c_{10})\sin 2\varphi, \\ \Sigma_{QU}(\vec{k}_\perp) &= c_{10}\sin 2\varphi\cos 2\varphi, \end{aligned} \tag{A.31}$$

Note that Σ_{IQ} and Σ_{IU} contain the same information and so do Σ_{QU} and $\Sigma_{QQ} - \Sigma_{UU}$. The relations between them follow immediately from Eq. A.31 and are given by Eq. 2.24.

Thus, only 4 of the Stokes correlators are independent: Σ_{II}, two of Σ_{QQ}, Σ_{UU}, Σ_{QU} and one of Σ_{IQ}, Σ_{IU}. We see that in Eq. A.31, these 4 independent observables are expressed in terms of 5 invariant scalar functions, c_1, c_2, c_4, c_6 and c_{10}, which cannot, therefore, all be reconstructed from polarised emission data even if isotropy is assumed (as we explained earlier, two other functions, c_{17} and c_{23}, which complete the full set of 7 alluded to in Sect. 2.4.4, can never be known from polarised-emission data).

The relations between the Stokes correlators and the invariant scalar functions given by Eq. A.31 contain angular dependence. It will be convenient for practical calculations to express

all observables in terms of angle averages (i.e., averages over all orientations of $\vec{k}_\perp$):

$$\begin{aligned}
\Sigma_1(k) &= \frac{1}{2\pi}\int d\varphi\, \Sigma_{II} = 4\,(c_1 + c_2 + c_4 + c_6) + c_{10}, \\
\Sigma_2(k) &= \frac{1}{2\pi}\int d\varphi\, (\Sigma_{QQ} + \Sigma_{UU}) = 8\,(c_2 + c_6) + c_{10}, \\
\Sigma_3(k) &= \frac{1}{2\pi}\int d\varphi\, [(\Sigma_{QQ} - \Sigma_{UU})\cos 4\varphi + 2\Sigma_{QU}\sin 4\varphi] = c_{10}, \\
\Sigma_4(k) &= \frac{1}{2\pi}\int d\varphi\, (\Sigma_{IQ}\cos 2\varphi + \Sigma_{IU}\sin 2\varphi) = 2c_4 + 4c_6 + c_{10}.
\end{aligned} \tag{A.32}$$

These formulae again give us 4 independent observable scalar functions, but now the quality of the statistics should be improved by the angle averaging. We will find that it is most convenient for practical calculations to use $\Sigma_1, \ldots, \Sigma_4$ as the basic set of observables (see Sect. A.2.2).

General Observable Quantities

Thus, only some 4th-order statistical quantities are observable. It is not hard to work out the condition for them to be so. First, as we already explained in our discussion of Eq. A.29, Stokes correlators carry no information about anything that involves the measures of mirror asymmetry of the field c_{17} and c_{23}. Let us then restrict our attention to quantities that contain only the remaining 5 invariant scalar functions that determine the 4th-order two-point statistics [Eq. A.28]. In general, we would be looking for a scalar function that has the form

$$\Phi(k) = f_1 c_1(k) + f_2 c_2(k) + f_4 c_4(k) + f_6 c_6(k) + f_{10} c_{10}(k), \tag{A.33}$$

where $f_1, \ldots, f_{10}$ are some known coefficients, which can be functions of k. Let us try to express this quantity in terms of Stokes correlators: this amounts to finding coefficients $\alpha, \beta, \gamma, \delta$, which can be functions of k and φ, such that

$$\Phi(k) = \frac{1}{4}\left(\alpha\Sigma_{II} + \beta\Sigma_{QQ} + \gamma\Sigma_{UU} + \delta\,\frac{\Sigma_{IQ}}{\cos 2\varphi}\right). \tag{A.34}$$

Using Eq. A.31, we get

$$\begin{aligned}
\Phi(k) &= \alpha c_1 + (\alpha + \beta + \gamma)\, c_2 + \left(\alpha + \frac{\delta}{2}\right) c_4 + (\alpha + \beta + \gamma + \delta)\, c_6 \\
&\quad + \frac{1}{4}\left(\alpha + \beta\cos^2 2\varphi + \gamma\sin^2 2\varphi + \delta\right) c_{10}.
\end{aligned} \tag{A.35}$$

Comparing this with Eq. A.33, we get

$$\begin{aligned}
\alpha &= f_1, \\
\beta &= \frac{1}{2}\left(f_2 - f_1 + \frac{3f_1 - f_2 - 4f_4 + 8f_{10}}{\cos 4\varphi}\right), \\
\gamma &= \frac{1}{2}\left(f_2 - f_1 - \frac{3f_1 - f_2 - 4f_4 + 8f_{10}}{\cos 4\varphi}\right), \\
\delta &= 2\,(f_4 - f_1) = f_6 - f_2.
\end{aligned} \tag{A.36}$$

The last formula gives two expressions for δ. In general, they do not have to be compatible and if they are not, the quantity $\Phi(k)$ cannot be expressed in terms of Stokes correlators. Thus, we have derived a simple criterion: only those quantities $\Phi(k)$ given by Eq. A.33 are observable for which

$$2f_1 - f_2 - 2f_4 + f_6 = 0. \tag{A.37}$$

If Eq. A.37 is satisfied, Eq. A.36 and Eq. A.34 give us a practical method for calculating Φ. As any interesting physical quantity Φ has to be independent of the angle φ between the wave vector $\vec{k}_\perp$ and the x axis of the coordinate system in which the Stokes parameters are measured, we are allowed to average over φ:

$$\Phi(k) = \frac{1}{8\pi}\int_0^{2\pi} d\varphi W(\varphi)\left[\alpha\Sigma_{II} + \beta\Sigma_{QQ} + \gamma\Sigma_{UU} + \delta\,\frac{\Sigma_{IQ}}{\cos 2\varphi}\right], \tag{A.38}$$

where $W(\varphi)$ is some weight function, which must satisfy $(1/2\pi)\int_0^{2\pi} d\varphi W(\varphi) = 1$. The weighting does not theoretically affect the result, so $W(\varphi)$ can be chosen arbitrarily.

The possibility of angle averaging with a weight function and a certain redundancy of information available from the Stokes correlators, as expressed by Eq. 2.24, mean that there are, in general, many different ways of reconstructing observable quantities. In theory they are all equivalent, but in practice one has to choose one with the aim of reducing noise and offsetting the potentially detrimental effect of singularities in the coefficients associated with factors of $1/\cos 2\varphi$ and $1/\cos 4\varphi$.

One method, which we have found to be quite effective, of avoiding this problem is to pick as our basic set of 4 observable scalar functions not the Stokes correlators themselves but the combinations of their angle averages given by Eq. A.32. Repeating the procedure we have just followed, we seek $\Phi(k)$ in the form

$$\Phi(k) = \frac{1}{4}\left(\alpha_1\Sigma_1 + \alpha_2\Sigma_2 + \alpha_3\Sigma_3 + \alpha_4\Sigma_4\right), \tag{A.39}$$

where the coefficients $\alpha_1, \ldots, \alpha_4$ are now functions of k only [there is no longer any angular

dependence on either side of Eq. A.39]. Using Eq. A.32, this becomes

$$\begin{aligned}\Phi(k)=&\alpha_1 c_1 + (\alpha_1 + 2\alpha_2)\, c_2 + \left(\alpha_1 + \frac{\alpha_4}{2}\right) c_4 + (\alpha_1 + 2\alpha_2 + \alpha_4)\, c_6 \\ &+ \frac{1}{4}\,(\alpha_1 + \alpha_2 + \alpha_3 + \alpha_4)\, c_{10}.\end{aligned} \tag{A.40}$$

Comparing this expression with Eq. A.33 as before, we get

$$\begin{aligned}\alpha_1 &= f_1, \\ \alpha_2 &= \frac{1}{2}\,(f_2 - f_1)\,, \\ \alpha_3 &= \frac{1}{2}\,(3f_1 - f_2 - 4f_4 + 8f_{10})\,, \\ \alpha_4 &= 2(f_4 - f_1) = f_6 - f_2,\end{aligned} \tag{A.41}$$

and the observability criterion is again given by Eq. A.37. Eq. A.39 together with Eq. A.32 and Eq. A.41 give another expression for a general observable $\Phi(k)$, defined by Eq. A.33 and subject to the constraint Eq. A.37.

Tension-Force Power Spectrum

In Sect. 2.4.6, we split the tension-force power spectrum into the directly observable part [Eq. 2.28], which could be recovered from the Stokes correlators without any assumptions, and the non-directly-observable part Φ_2 [Eq. 2.29], which could only be reconstructed using some assumed symmetries of the 4th-order correlation tensor. Assuming isotropy, we infer from Eq. A.30

$$\Phi_2 = k^2(c_2 + c_6). \tag{A.42}$$

Using Eq. A.29 to express $c_2 + c_6$ in terms of the perpendicular components of the tensor $c_{ij,mn}$, we immediately recover Eq. 2.30 and the rest follows as explained in Sect. 2.4.6.

This was an *ad hoc* derivation specific to the tension-force power spectrum. Let us now demonstrate how the general method laid out in Sect. A.2.2 works for this quantity.

Substituting Eq. A.28 into Eq. 2.26, we get

$$\Phi(k) = k^2\,[c_1(k) + 4c_2(k) + 2c_4(k) + 6c_6(k) + c_{10}(k)]\,, \tag{A.43}$$

a particular case of Eq. A.33. The observability criterion given by Eq. A.37 is satisfied, so,

using Eq. A.34 and Eq. A.36, we obtain

$$\begin{aligned}\Phi(k) &= \frac{1}{4}k^2\left[\Sigma_{II} + \frac{1}{2}\left(3 - \frac{1}{\cos 4\varphi}\right)\Sigma_{QQ}\right. \\ &\quad \left. + \frac{1}{2}\left(3 + \frac{1}{\cos 4\varphi}\right)\Sigma_{UU} + \frac{2}{\cos 2\varphi}\Sigma_{IQ}\right],\end{aligned} \tag{A.44}$$

which can be angle-averaged with some weight function according to Eq. A.38.

An alternative expression in terms of averaged Stokes correlators follows from Eq. A.39 and Eq. A.41:

$$\Phi(k) = \frac{1}{4}k^2\left(\Sigma_1 + \frac{3}{2}\Sigma_2 - \frac{1}{2}\Sigma_3 + 2\Sigma_4\right). \tag{A.45}$$

Substituting for $\Sigma_1, \ldots, \Sigma_4$ from Eq. A.32, we arrive at

$$\begin{aligned}\Phi(k) = \frac{k^2}{8\pi}\int_0^{2\pi} d\varphi\Big[&\Sigma_{II} + 2\left(\Sigma_{IQ}\cos 2\varphi + \Sigma_{IU}\sin 2\varphi\right) - \Sigma_{QU}\sin 4\varphi \\ &+ \frac{1}{2}\left(3 - \cos 4\varphi\right)\Sigma_{QQ} + \frac{1}{2}\left(3 + \cos 4\varphi\right)\Sigma_{UU}\Big].\end{aligned} \tag{A.46}$$

Our final formula for the tension-force power spectrum, Eq. 2.31, follows from Eq. A.46 upon multiplication by $4\pi k^2$ (the wave-vector-space volume factor). Note that the integrand in Eq. A.46 reduces back to Eq. A.44 if we make use of Eq. 2.24, but the advantage of Eq. A.46 is that it does not contain any singular coefficients.

A.2.3 Observables in the Case of Weak Mean Field

If a weak mean field is present, we proceed analogously to Sect. A.2.2. It is understood that the mean field is sufficiently weak so as not to break the isotropy of the fluctuating part of the field. Then, using Eq. 2.33, Eq. A.10 and Eq. A.21 and setting $k_z = 0$ to express the line-of-sight

integrals, we find

$$\begin{aligned}
C_{xx,xx}(\vec{k}_\perp) &= c_{xx,xx}(\vec{k}_\perp) + 2\overline{B}_x^2 \sin^2\varphi\, m_1, \\
C_{yy,yy}(\vec{k}_\perp) &= c_{yy,yy}(\vec{k}_\perp) + 2\overline{B}_y^2 \cos^2\varphi\, m_1, \\
C_{xx,yy}(\vec{k}_\perp) &= c_{xx,yy}(\vec{k}_\perp) - 2\overline{B}_x\overline{B}_y \sin\varphi\cos\varphi\, m_1 \\
&\quad + 4i\left(\overline{B}_x \sin\varphi + \overline{B}_y \cos\varphi\right)\sin\varphi\cos\varphi\, a_2, \\
C_{xy,xy}(\vec{k}_\perp) &= c_{xy,xy}(\vec{k}_\perp) + \frac{1}{2}\left(\overline{B}_x \cos\varphi - \overline{B}_y \sin\varphi\right)^2 m_1, \\
C_{xx,xy}(\vec{k}_\perp) &= c_{xx,xy}(\vec{k}_\perp) - \overline{B}_x \sin\varphi\left(\overline{B}_x \cos\varphi - \overline{B}_y \sin\varphi\right) m_1 \\
&\quad - 2i\left(\overline{B}_x \sin\varphi - \overline{B}_y \cos\varphi\right)\sin^2\varphi\, a_2, \\
C_{yy,xy}(\vec{k}_\perp) &= c_{yy,xy}(\vec{k}_\perp) + \overline{B}_y \cos\varphi\left(\overline{B}_x \cos\varphi - \overline{B}_y \sin\varphi\right) m_1 \\
&\quad + 2i\left(\overline{B}_x \sin\varphi - \overline{B}_y \cos\varphi\right)\cos^2\varphi\, a_2,
\end{aligned} \tag{A.47}$$

where the components of $c_{ij,mn}(\vec{k}_\perp)$ are given by Eq. A.29 and Eq. A.30.

Stokes Correlators

Using Eq. A.47 and Eq. 2.15, we find that the Stokes correlators are

$$\begin{aligned}
\Sigma_{II}(\vec{k}_\perp) &= 2\left(\overline{B}_x \sin\varphi - \overline{B}_y \cos\varphi\right)^2 m_1 + \text{4th order}, \\
\Sigma_{QQ}(\vec{k}_\perp) &= 2\left(\overline{B}_x \sin\varphi + \overline{B}_y \cos\varphi\right)^2 m_1 + \text{4th order}, \\
\Sigma_{UU}(\vec{k}_\perp) &= 2\left(\overline{B}_x \cos\varphi - \overline{B}_y \sin\varphi\right)^2 m_1 + \text{4th order}, \\
\Sigma_{IQ}(\vec{k}_\perp) &= 2\left(\overline{B}_x^2 \sin^2\varphi - \overline{B}_y^2 \cos^2\varphi\right) m_1 \\
&\quad - 4i\left(\overline{B}_x \sin\varphi - \overline{B}_y \cos\varphi\right)\sin 2\varphi\, a_2 + \text{4th order}, \\
\Sigma_{IU}(\vec{k}_\perp) &= -\left[\left(\overline{B}_x^2 + \overline{B}_y^2\right)\sin 2\varphi - 2\overline{B}_x\overline{B}_y\right] m_1 \\
&\quad + 4i\left(\overline{B}_x \sin\varphi - \overline{B}_y \cos\varphi\right)\cos 2\varphi\, a_2 + \text{4th order}, \\
\Sigma_{QU}(\vec{k}_\perp) &= -\left[\left(\overline{B}_x^2 - \overline{B}_y^2\right)\sin 2\varphi + 2\overline{B}_x\overline{B}_y \cos 2\varphi\right] m_1 \\
&\quad - 4i\left(\overline{B}_x \sin\varphi - \overline{B}_y \cos\varphi\right) a_2 + \text{4th order},
\end{aligned} \tag{A.48}$$

where the 4th-order parts of the correlators are given by Eq. A.31.

Thus, the Stokes correlators now contain not just the 4th-order statistics but also some information about the second- and 3rd-order correlation functions of the field, namely, the magnetic-field power spectrum $m_1(k)$ [see Eq. A.10] and the 3rd-order correlation function $a_2(k)$ [Eq. A.21]. We are not particularly interested in a_2 and notice that all terms containing it can be eliminated from Eq. A.48 simply by taking the real part of the Stokes correlators Σ_{IQ}, Σ_{IU} and

Σ_{QU}. We will now isolate the second- and 4th-order contributions to the Stokes correlators and calculate the power spectra of the magnetic field and of the tension force.

Magnetic-Field Power Spectrum

There are several formulae that allow one to distill m_1 from the Stokes correlators. They are all derived by assembling appropriate linear combinations of the correlators and angle averaging. The simplest such formulae are found by noticing that the angle averages of the 4th-order parts of Σ_{IQ}, Σ_{IU} and of $\Sigma_{QQ} - \Sigma_{UU}$ vanish [see Eq. A.31], so

$$\begin{aligned}
\frac{1}{2\pi}\int_0^{2\pi} d\varphi\, \mathrm{Re}\Sigma_{IQ} &= \left(\overline{B}_x^2 - \overline{B}_y^2\right) m_1, \\
\frac{1}{2\pi}\int_0^{2\pi} d\varphi\, \mathrm{Re}\Sigma_{IU} &= 2\overline{B}_x\overline{B}_y m_1, \\
\frac{1}{2\pi}\int_0^{2\pi} d\varphi\, (\Sigma_{QQ} - \Sigma_{UU}) &= 8\overline{B}_x\overline{B}_y m_1,
\end{aligned} \tag{A.49}$$

The standard one-dimensional magnetic-field power spectrum is defined with an additional wave-number-space volume factor of $4\pi k^2$ [Eq. A.15]—the resulting expressions for it are given in Eq. 2.37.

It is also possible to construct formulae that formally do not require angle averaging at all: using the fact that for certain combinations of the Stokes correlators the 4th-order contributions must vanish [assuming isotropy; see Eq. 2.24], we find

$$\begin{aligned}
m_1 &= \frac{\mathrm{Re}\left(\Sigma_{IQ}\sin 2\varphi - \Sigma_{IU}\cos 2\varphi\right)}{\left(\overline{B}_x^2 - \overline{B}_y^2\right)\sin 2\varphi - 2\overline{B}_x\overline{B}_y\cos 2\varphi}, \\
m_1 &= -\frac{(\Sigma_{QQ} - \Sigma_{UU})\sin 4\varphi - 2\mathrm{Re}\Sigma_{QU}\cos 4\varphi}{2\left[\left(\overline{B}_x^2 - \overline{B}_y^2\right)\sin 2\varphi - 2\overline{B}_x\overline{B}_y\cos 2\varphi\right]}.
\end{aligned} \tag{A.50}$$

Since m_1 is independent of the orientation of the wave vector, these expressions can be averaged over the angle φ with arbitrary weight functions. Note that in order to compute the shape of the spectrum from Eq. A.50, we do not need to know the magnitude of the mean field but we do need its orientation (in the plane perpendicular to the line of sight).

In practice, we expect the formulae given by Eq. A.49 to work better than those given by Eq. A.50 because the latter rely on exact cancellations that are probably not going to happen with very high precision in realistic situations. Even moderate errors in cancelling the 4th-order correlators could then easily overwhelm the second-order ones: indeed, the terms in Eq. A.48 involving the mean field are small because the mean field was assumed to be weak: $\overline{B}^2 \ll \langle b^2\rangle$, so $\overline{B}^2 m_1 \ll c_{ij,mn}$. In Eq. A.49, the cancellation of the 4th-order correlators comes from angle averaging and there is hope that $m_1(k)$ could be recovered (but see the caveat at the end of

Sect. 2.4.7).

Magnitude and Orientation of the Mean Field

The orientation of the mean field (or, rather, its projection on the plane perpendicular to the line of sight) can be easily determined from the Stokes parameters themselves: the angle Θ between the mean field and the x axis satisfies

$$\tan 2\Theta = \frac{2\overline{B}_x\overline{B}_y}{\overline{B}_x^2 - \overline{B}_y^2} = \frac{\langle U\rangle}{\langle Q\rangle}. \tag{A.51}$$

Note that $\tan 2\Theta$ tells us the orientation but not the sign of the mean field. This angle can also be determined from the Stokes correlators via Eq. A.49:

$$\tan 2\Theta = \frac{\int_0^{2\pi} d\varphi\, \mathrm{Re}\Sigma_{IU}}{\int_0^{2\pi} d\varphi\, \mathrm{Re}\Sigma_{IQ}} = \frac{\int_0^{2\pi} d\varphi\, (\Sigma_{QQ} - \Sigma_{UU})}{4\int_0^{2\pi} d\varphi\, \mathrm{Re}\Sigma_{IQ}}, \tag{A.52}$$

but the validity of these formulae, unlike that of Eq. A.51, is predicated on assuming the statistical isotropy of the fluctuating field. If this assumption is well satisfied, the value of $\tan 2\Theta$ obtained from Eq. A.52 should be independent of k.

The magnitude of the mean field is a slightly more complicated quantity to determine. From the total emission intensity [see Eq. 2.10],

$$\langle I\rangle = \overline{B}_\perp^2 + \langle b_x^2\rangle + \langle b_y^2\rangle = \overline{B}_\perp^2 + \frac{2}{3}\langle b^2\rangle, \tag{A.53}$$

where $\overline{B}_\perp^2 = \overline{B}_x^2 + \overline{B}_y^2$ and the last expression follows from assuming the statistical isotropy of the fluctuating field $\vec{b}$. Thus, from averaging I, we can calculate the total energy density of the magnetic field but not individually the magnitudes of the mean and fluctuating fields. On the other hand, once we know Θ, we can find $\overline{B}_\perp^2 m_1$ from Eq. A.49 or Eq. A.50. Let us integrate this quantity over all wavenumbers and denote the result by A:

$$\overline{B}_\perp^2 \int_0^\infty dk\, 4\pi k^2 m_1(k) = \overline{B}_\perp^2 \langle b^2\rangle = A. \tag{A.54}$$

Then $\langle b^2\rangle = A/\overline{B}_\perp^2$ and substituting this into Eq. A.53, we arrive at a biquadratic equation for $\overline{B}_\perp$, whose solution is

$$\overline{B}_\perp^2 = \frac{1}{2}\left(\langle I\rangle - \sqrt{\langle I\rangle^2 - \frac{8}{3}A}\right) \simeq \frac{2}{3}\frac{A}{\langle I\rangle}. \tag{A.55}$$

We have chosen the "−" root because we are assuming $\overline{B}^2 \ll \langle b^2\rangle$ (weak mean field). While we

do not really need to know $\overline{B}_\perp^2$ to disentangle the second- and 4th-order statistics in Eq. A.48, we can use Eq. A.55 to check that the mean field really is weak:

$$\overline{B}_\perp^2 \ll \langle I \rangle. \tag{A.56}$$

Fourth-Order Quantities

Now that we know the mean field and $m_1(k)$, we can use this information in Eq. A.48 to isolate the 4th-order statistics in the Stokes correlators and then proceed to calculating all observable 4th-order quantities in the same way it was done in Sect. A.2.2. In general, this involves subtracting from the (real part of) the Stokes correlators the terms that contain m_1 [Eq. A.48] so that only the 4th-order contributions [Eq. A.31] remain. Doing this requires knowing $\overline{B}_\perp^2 m_1(k)$ (see Sect. A.2.3) and the orientation of the mean field [Eq. A.51]. Subtracting the second-order contributions from the the averaged Stokes correlators introduced in Eq. A.32 is a particularly simple operation: substituting from Eq. A.48 into Eq. A.32 and carrying out the angle averages, we get

$$\begin{aligned}
\Sigma_1(k) &= \overline{B}_\perp^2 m_1 + \text{4th order}, \\
\Sigma_2(k) &= 2\overline{B}_\perp^2 m_1 + \text{4th order}, \\
\Sigma_3(k) &= \text{4th order}, \\
\Sigma_4(k) &= -\frac{3}{4}\overline{B}_\perp^2 m_1 + \text{4th order},
\end{aligned} \tag{A.57}$$

where the 4th-order parts are given by Eq. A.32 and real part of the Stokes correlators is taken everywhere to eliminate the contributions from the 3rd-order statistics.

Tension-Force Power Spectrum

To find the tension-force power spectrum when $\overline{B} \neq 0$, substitute Eq. 2.33 into Eq. 2.26 and use the solenoidality of the magnetic field [Eq. A.13 and Eq. A.20]:

$$\Phi = \overline{B}_j \overline{B}_n k_j k_n c_{i,i} + \overline{B}_n k_n k_j \left(c_{ij,i} + c^*_{ij,i} \right) + k_j k_n c_{ij,in}. \tag{A.58}$$

From Eq. A.21, we see that the second term vanishes. Using Eq. A.10 to express the first term in terms of the magnetic-field power spectrum, setting $\vec{k} = k_\perp(\cos\varphi, \sin\varphi, 0)$ (line-of-sight integral) and angle-averaging over φ, we get

$$\Phi(k) = \frac{1}{2} k^2 \overline{B}_\perp^2 m_1(k) + \text{4th order}, \tag{A.59}$$

where the 4th-order part is given by Eq. A.43 and is calculated from Stokes correlators in the same way as in Sect. A.2.2. Namely, using Eq. A.45 and Eq. A.57, we get

$$\Phi(k) = \frac{1}{4}k^2\left(\Sigma_1 + \frac{3}{2}\Sigma_2 - \frac{1}{2}\Sigma_3 + 2\Sigma_4 - \frac{1}{2}\overline{B}_\perp^2 m_1\right), \tag{A.60}$$

where $\Sigma_1, \ldots, \Sigma_4$ are defined in Eq. A.32 (with real parts taken of the Stokes correlators) and $\overline{B}_\perp^2 m_1$ is calculated via one of the formulae given in Sect. A.2.3. Eq. 2.38 follows upon multiplication by the wave-number-space volume factor $4\pi k^2$.

Appendix B

Operations with spherical harmonics

B.1 Filter derivation

In this section we describe how to obtain an optimally matched filter function $\Psi(\theta, \varphi) = \sum_l \sum_m \psi_{lm} Y_l^m(\theta, \varphi)$ for attempting to detect a non azimuthally-symmetric target signal (such as the signal due to e.g. the galactic kSZ or the B mode due to galactic Thomson scattering) in the presence of a Gaussian random noise (e.g. the sum of CMB anisotropies, total or polarised, and the instrumental noise). We used such a filtering procedure in investigations of the RS effect (Maturi et al., 2007).

Following the arguments layed out by Haehnelt & Tegmark (1996), Maturi et al. (2005) and Schäfer et al. (2006), we assume the data to be composed of the statistically homogeneous CMB anisotropies, some instrumental Gaussian random noise and the targeted signal. The expansion of the data in spherical harmonics ($Y_l^m(\theta, \varphi)$) is

$$S(\theta, \varphi) = \sum_l \sum_m s_{lm} Y_l^m(\theta, \varphi), \tag{B.1}$$

where we model the complex coefficient s_{lm} as

$$s_{lm} = A\tau_{lm} + a_{lm}. \tag{B.2}$$

We choose A to be the maximum amplitude of the targeted signal, while the morphology is encoded in the complex spherical harmonic coefficient τ_{lm}. The sum of the CMB and the noise sky is $a_{lm} = a'_{lm} + n_{lm}$, where n_{lm} is the instrumental noise modelled as a white Gaussian random noise field. Note that the ensemble average $\langle a_{lm} \rangle = 0$.

In the studies mentioned above, the convolution of the filter with the total signal is performed for all positions on the sky (or the corresponding analogous on the plane), in effect generating a

convolution map described by

$$\Psi * S = \int d\Omega\, \Psi(\theta - \alpha, \varphi - \beta) S(\theta, \varphi). \tag{B.3}$$

In our case, however, we know the precise position and orientation of our target signal, therefore we need only to evaluate the convolution for a single position on the sky. We define the estimate of the target signal strength to be

$$\overline{A} = \int d\Omega\, S(\theta, \varphi) \Psi(\theta, \varphi). \tag{B.4}$$

We want to estimate the real peak amplitude of the target effect accurately. Hence we enforce an unbiased estimate

$$b = A - < \overline{A} >= 0, \tag{B.5}$$

with variance

$$\sigma^2 \quad = \quad \langle \overline{A}^2 \rangle - A^2 = \sum_l \sum_m C_l \left|\psi_{lm}\right|^2 . \tag{B.6}$$

We enforce the condition that the variance be minimal by means of Lagrange multipliers. We are looking for the filter Ψ which would give the smallest error for the estimate in Eq. B.4, subject to the constraint of being unbiased (Eq. B.5). Thus we solve

$$\frac{\partial}{\partial \Psi^*} \left(\sigma^2 - \lambda b - \lambda' b^* \right) = 0. \tag{B.7}$$

The resulting filter is given by

$$\psi_{lm} = \frac{\lambda \tau_{lm}}{C_l}, \tag{B.8}$$

which, when substituted in Eq. B.5, yields

$$\lambda = \frac{1}{\sum_l \sum_m \left(\left|\tau_{lm}\right|^2 / C_l \right)} \quad \text{and} \tag{B.9}$$

$$\psi_{lm} = \frac{1}{\sum_l \sum_m \left(\left|\tau_{lm}\right|^2 / C_l \right)} \frac{\tau_{lm}}{C_l}. \tag{B.10}$$

Analogous to the flat space results in Haehnelt & Tegmark (1996), the filter gives preference to modes where the ratio of the target signal to the noise is largest. The estimate of the target signal amplitude is performed using Eq. B.4 with the error given by B.6 and the filter by B.10.

a_{2m}	complex value
a_{22}	$(-14.41 - i18.8)/\sqrt{2}$
a_{21}	$(-0.05 + i4.86)/\sqrt{2}$
a_{20}	11.48

Table B.1: The a_{lm} coefficients calculated from the real valued coefficients in table 6 of Hinshaw et al. (2007). These coefficients are obtained for the z-axis of the coordinate system pointing to the galactic north pole.

B.2 Rotating spherical harmonic coefficients

Here we describe how a set of spherical harmonic quadrupole coefficients (a_{2m}) transforms under a rotation of the coordinate system. In particular we obtain the rotated spherical harmonic coefficient needed for computing the Stokes Q and U parameters (Eqs. 4.8 and 4.9 in sec. 4.3).

The real-valued a_{2m} coefficients for the CMB radiation given by Hinshaw et al. (2007), are related to the complex-valued spherical harmonics (the convention in this paper) as listed in table B.2 .

The transformation of spherical harmonics under a rotation described by the Euler angles α, β and γ is given by Varshalovich et al. (1988):

$$\hat{Y}_l^{m'}(\hat{\theta},\hat{\varphi}) = \sum_{m=-l}^{l} D^l_{mm'}(\alpha,\beta,\gamma) Y_l^m(\theta,\varphi),$$

where $D^l_{mm'}(\alpha,\beta,\gamma)$ is the Wigner-D symbol. The hat denotes quantities in the rotated coordinate system, otherwise quantities are taken to be in the usual coordinate system where z points towards the galactic north pole. In our case, the inverse transformation is needed,

$$Y_l^{m'}(\theta,\varphi) \quad = \quad \sum_{m=-l}^{l} {D^l_{m'm}}^*(\alpha,\beta,\gamma) \hat{Y}_l^m(\hat{\theta},\hat{\varphi}). \tag{B.11}$$

The inverse of the Wigner-D symbol is given by

$${D^{-1}}^l_{mm'}(\alpha,\beta,\gamma) = {D^l_{m'm}}^*(\alpha,\beta,\gamma), \tag{B.12}$$

here the asterix denotes complex conjugation.

We can write the total quadrupole intensity as a combination of spherical harmonics in any coordinate system

$$I_{l=2}(\theta,\varphi) \quad = \quad \sum_{m=-2}^{2} a_{2m} Y_2^m(\theta,\varphi) = \sum_{m=-2}^{2} \hat{a}_{2m} \hat{Y}_2^m(\hat{\theta},\hat{\varphi}). \tag{B.13}$$

Substituting B.11 in B.13, multiplying by $Y_2^2(\theta,\varphi)$, and performing an integral over the

whole sphere yields,

$$\hat{a}_{22} = \sum_{m'=-2}^{2} a_{2m'} {D^2_{m'2}}^*(\alpha, \beta, \gamma). \tag{B.14}$$

The Wigner-D symbol is ${D^2_{m'2}}^*(\alpha, \beta, \gamma) = e^{im'\alpha} {d^2_{m'2}}^*(\beta) e^i m\gamma$, with

$${d^2_{m'2}}^*(\beta) = [(2+m')!(2-m')!4!]^{1/2} \frac{\cos^{(2+m')}(\beta/2) \sin^{(2-m')}(\beta/2)}{(2-m')!(2+m')!}.$$

We require the value of $\hat{a}_{22}$ in a coordinate system which has its negative z-axis pointing in the direction specified by the usual θ and φ angles. The corresponding Euler angles are

$$\gamma = -\pi/2\,,\ \beta = \pi - \theta\,,\ \alpha = \varphi - \pi.$$

Note that this means that the x-axis and y-axis point in negative φ and negative θ directions, respectively. This is the coordinate system in which the Stokes Q and U parameters are calculated in this work.

Inserting $\hat{a}_{22}$ in Eqs. 4.10 and 4.11 and multiplying these with the corresponding LOS integral of the thermal-electron density and the appropriate constant pre-factor yields Eqs. 4.8 and 4.9.

Appendix C

Technical details of the Hammurabi code

C.1 The 3D HEALPix grid

The HAMMURABI code generates HEALPix maps with an angular resolution defined by the parameter NSIDE = 2^k, where $k \in [0, 13]$ (the maximum k is a computational limit; it could be extended only by alterations to the original HEALPix package). The integration volume has a cone-like geometry. To minimise the non-homogeneous volume sampling induced by that, the integration volume is consecutively subdivided into so-called subbeams. Each section of these subbeams is contained in a shell centred on Earth. We shall call this grid the 3D HEALPix grid.

This subdivision depends on

- the radial length Δr of each volume unit in the observation beam,
- how many shells $H_{\max}$ in total there will be,
- what resolution, or equivalently what $\mathrm{NSIDE}_{\mathrm{obs}}$ the observation shell has,
- and finally the shell number of the observation shell H_{obs} (See an example in Fig. C.1).

The distances at which the beam is split, or equivalently the upper boundaries [1] of the shells, are given by

$$d_i = R_{max} 2^{i - H_{\max}} \,, \tag{C.1}$$

where the index $i \in [1, H_{\max}]$. Due to the disk-like shape of our galaxy, the effective radius out to which we perform our computations varies and decreases sharply towards high latitudes and towards the anti-centre direction.

The maximum volume for each shell is a constant corresponding approximately to

$$V_{max} = 4\pi d_{H_{\mathrm{obs}}}^2 \frac{\Delta r}{12 \cdot \mathrm{NSIDE}_{\mathrm{obs}}^2}. \tag{C.2}$$

[1] The code will automatically round down d_i to a multiple of Δr.

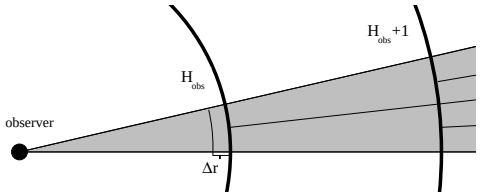

Figure C.1: An example of the 3D HEALPix grid. For simplicity, it is presented in 2D. The gray shaded area corresponds to the integration volume.

We suggest [2] a definition of Δr such that the maximum volume unit at the largest shell is close to a cubic form.

We note that the maximum volume unit V_{max} decreases with higher observation resolution. It defines the minimum scale that can be resolved wit the code for a certain resolution. Fluctuations smaller than that cannot be resolved by the code. This is a formal upper limit, since the Galactic regions more likely to contain small-scale fluctuations are probably not at the far end of the observation volume, where V_{max} is located, but instead at regions closer to the observer, where the spatial resolution is finer.

C.2 Line of sight integration

For the i-th volume element of a cone, according to the formulae in Sect. 3.3, we compute the following,

$$
\begin{cases}
I_i^{\rm syn} &= C_I B_{i,t}^{(1+p)/2} \nu^{(1-p)/2} e^{-\tau_i} \Delta r \\
P_i &= C_P B_{i,\perp}^{(1+p)/2} \nu^{(1-p)/2} e^{-\tau_i} \Delta r \\
\Delta RM_i &= \frac{a_0}{2} \left(n_{e,i-1} B_{LOS,i-1} + n_{e,i} B_{LOS,i} \right) \Delta r \\
\chi_i &= \sum_{j=1}^{i} RM_j \lambda^2 + \chi_{i,0} \\
Q_i &= P_i \cos(2\chi_i) \\
U_i &= P_i \sin(2\chi_i) \\
B_{x,i} &= B_{i,t} \cos(\chi_{i,0}) \\
B_{y,i} &= B_{i,t} \sin(\chi_{i,0}) \\
\Delta\tau_i &= \frac{8.235}{2} \times 10^{-2} \nu^{-2.1} \left(T_{e,i-1}^{-1.35} EM_{i-1} + T_{e,i}^{-1.35} EM_i \right) \\
\Delta EM_i &= n_{e\,i}^2 \Delta r \\
I_i^{\rm ff} &= 0.5 \left(T_{e,i-1} + T_{e,i} \right) e^{-\tau_i} (e^{\Delta\tau_i} - 1) \\
\Delta\overline{\tau\beta}_i^{kSZ} &= \sigma_T n_{e,i} \beta_i \Delta r \\
\Delta f_i &= \frac{3\sigma_T}{16\pi} n_{e,i} \Delta r
\end{cases}
\tag{C.3}
$$

[2] Choices of any other constant are of course possible.

We note that the calculated Stokes values U_i and Q_i for each volume element include the effect of foreground RM. Furthermore, total and polarised synchrotron emission are subject to free-free absorption (the $e^{-\tau}$ term), which is only relevant at frequencies well below 408MHz (see e.g. Sun et al., 2008). The CR electrons are assumed to follow a power law with an energy spectral index p (see Sect. 3.3.2). The values C_I and C_P are dependent on the spatially dependent spectral index p and the spatial distribution component of the cosmic rays C, and can be obtained from formulae given in Sect. 3.3 and Rybicki & Lightman (1979). The intrinsic polarisation angle $\chi_{i,0}$ is locally defined as zero if the magnetic field is pointing in a positive Galactic-coordinates l-direction and $\pi/2$ when the magnetic field is pointing in a positive Galactic-coordinates b-direction. The free-free emission is taken from Rohlfs & Wilson (1996). The spatially varying thermal electron temperature T_e is given by Eq. 3.11. Finally, depending on the user's needs, not all computations in Eq. C.3 are necessary and can be deactivated.

The intensities, RM, τ, and UDMs for a pixel are straightforward to compute. They consist of an integral of the contributions from all volume units below (Eq. C.4). For the intensities, in case of a subdivision of the observation cone into subcones, the computation is completed by averaging the set of subcones. However, this is not the case for the UDM, τ, and RM values, since they are found to be linearly dependent on λ^3, $\lambda^{2.1}$ and λ^2 respectively, where λ is the wavelength. Beam averaging would destroy this linear behaviour.[3] The UHECR deflection measure is given by $UDM = \sqrt{UDM_x^2 + UDM_y^2}$, while the deflection orientation is given by $\Theta_{\mathrm{defl}} = \arctan \frac{UDM_x}{UDM_y}$.

$$
\begin{cases}
I & = & \sum_i I_i \\
Q & = & \sum_i Q_i \\
U & = & \sum_i U_i \\
RM_i & = & \sum_j^i \Delta RM_j \\
\tau_i & = & \sum_j^i \Delta\tau_j \\
UDM_x & = & \sum_i B_{x,i}\Delta r \\
UDM_y & = & \sum_i B_{x,i}\Delta r \\
\overline{\tau\beta}^{kSZ} & = & \sum_i \Delta\overline{\tau\beta}_i^{kSZ} \\
Q^{TS} & = & \sqrt{\frac{32\pi}{15}}\mathrm{Re}\, a_{22} \sum_i \Delta f_i \\
U^{TS} & = & \sqrt{\frac{32\pi}{15}}\mathrm{Im}\, a_{22} \sum_i \Delta f_i
\end{cases}
\tag{C.4}
$$

[3]The final RM, τ, and UDM value is defined as the sum of the highest possible resolution sub-beam of all parent beam contributions. Thus, one intensity pixel might have several corresponding RM,τ, and UDM pixels.

C.3 Magnetic field models

For the convenience of the reader we present the parameterisations of the Galactic magnetic field following Page et al. (2007) and Sun et al. (2008). All parameters are presented in the usual cylindrical coordinates, with respect to an origin located at the Galactic centre. The x-axis of the coordinate system points in the opposite direction of the Sun, while the z-axis points towards the Galactic north.

- Page et al. (2007) writes

$$\vec{B}(r,\varphi,z) = B_0 \left[\cos\psi(r)\,\cos\chi(z)\hat{r} + \right. \tag{C.5}$$

$$\left. \sin\psi(r)\,\cos\chi(z)\hat{\varphi} + \sin\chi(z)\hat{z}\right] \tag{C.6}$$

  Here $\psi(r) = \psi_0 + \psi_1 ln(r/8\text{kpc})$, $\chi(z) = \chi_0 \tanh(z/1\text{kpc})$. The radial variable $r \in [3\text{kpc}, 8\text{kpc}]$, $\chi_0 = 25^o$, $\psi_1 = 0.9^o$ and $\psi_0 = 27^o$. B_0 is not specified in Page et al. (2007) and we put $B_0 = 4\,\mu G$.

- While Sun et al. (2008) presents some suggestions for fields, and we select their *ASS+RING* parameterisation:

$$\begin{cases} B^D_{\hat{r}} &= D_1(R,\varphi,z) D_2(R,\varphi,z) \sin p \\ B^D_{\hat{\varphi}} &= -D_1(R,\varphi,z) D_2(R,\varphi,z) \cos p \\ B^D_{\hat{z}} &= 0 \end{cases} \tag{C.7}$$

  where

$$D_1(r,z) = \begin{cases} B_0 \exp\left(-\dfrac{r-R_\odot}{R_0} - \dfrac{|z|}{z_0}\right) & r > R_c \\ B_c & r \leqslant R_c \end{cases} \tag{C.8}$$

  and $R_0 = 10$ kpc, $z_0 = 1$ kpc, $R_c = 5$ kpc, $B_0 = 2\,\mu$G, and $B_c = 2\,\mu$G. and

$$D_2(r) = \begin{cases} +1 & r > 7.5 \text{ kpc} \\ -1 & 6 \text{ kpc} < r \leqslant 7.5 \text{ kpc} \\ +1 & 5 \text{ kpc} < r \leqslant 6 \text{ kpc} \\ -1 & r \leqslant 5 \text{ kpc} \end{cases} \tag{C.9}$$

  while the halo field is given by,

$$B^H_\varphi(r,z) = B^H_0 \frac{1}{1 + \left(\dfrac{|z| - z^H_0}{z^H_1}\right)^2} \frac{r}{R^H_0} \exp\left(-\frac{r - R^H_0}{R^H_0}\right) \tag{C.10}$$

and the parameters are $z_0^H = 1.5$ kpc, $B_0^H = 10\,\mu$G, $R_0^H = 4$ kpc, $z_1^H = 0.2$ kpc (for $|z| < z_0^H$), and $z_1^H = 0.4$ kpc (otherwise).

C.3.1 Tinyakov and Tkachev model

The Tinyakov & Tkachev (2002) model is based on RM data and interpretation thereof by a number of works (Rand & Kulkarni, 1989; Rand & Lyne, 1994; Han & Qiao, 1994; Indrani & Deshpande, 1999; Han et al., 1997, 1999; Frick et al., 2001; Beck, 2001; Sofue & Fujimoto, 1983; Vallee, 1991; Han, 2002). It has been used for cosmic ray proton propagation studies (Tinyakov & Tkachev, 2002; Kachelrieß et al., 2007). In cylindrical coordinates the parametrisation is,

$$\begin{cases} B_{\hat{r}} &= B(r,\theta,z)\sin pitch\,, \\ B_{\hat{\varphi}} &= B(r,\theta,z)\cos pitch\,, \\ B_{\hat{z}} &= B(r,\theta,z)\,. \end{cases} \tag{C.11}$$

Where

$$\begin{aligned} B(r,\theta,z) &= \mathrm{sign}(z) exp\left(-\frac{|z|}{h}\right) B(r,\theta)\,, \\ B(r,\theta) &= B(r)\cos\left(\theta - \beta ln\left(\frac{r}{R_{Sun}}\right) + \varphi\right)\,, \\ B(r) &= \begin{cases} B_0 \dfrac{R_{Sun}}{r\cos\varphi} & r \geqslant 4\mathrm{kpc} \\ B(r = 4\mathrm{kpc}) & r < 4\mathrm{kpc} \end{cases}\,. \end{aligned} \tag{C.12}$$

At a maximum distance of 20 kpc from the Galactic centre, the field is set to zero. The constant phase φ is $\varphi = \beta ln\,(1 + d/R_{Sun}) - \pi/2$ and $\beta = 1/\tan pitch$. The parameters given by Tinyakov & Tkachev (2002) are $B_0 = 1.4\,\mu$G, $pitch = -8$ deg, $d = -0.5$ kpc and $h = 1.5$ kpc. The units of B are μG.

C.3.2 The Harari model

Harari et al. (1999) following (Sofue & Fujimoto, 1983; Stanev, 1997; Beck et al., 1996) proposed a field of the same structure as in Eq. C.11 with $B(r,\theta,z) = f(z)B(r,\theta)$ (in μG), where

$$f(z) = \frac{1}{2\cosh(z/z_1)} + \frac{1}{2\cosh(z/z_2)}\,,$$

and $B(r,\theta)$ is as in Eq. C.12 (and with the same definitions of φ and β). Finally, $B(r) = \frac{3R_{Sun}}{r}\tanh^3(r/r_1)$. The parameters given by Harari et al. (1999) are $z_1 = 0.3$kpc, $z_2 = 4$kpc, $pitch = -10$ deg, $r_1 = 2$kpc and $d = -4.69$kpc. At a maximum distance of 20 kpc from the Galactic centre, the field is set to zero.

C.3.3 The Jansson model

Jansson et al. (2007) present a slightly altered version of the Han & Qiao (1994) parametrisation. The basic structure is the one of Eq. C.11, with $B(r, \theta, z) = B(r, \theta)$,

$$B(r, \theta, z) = B(r, \theta) e^{\frac{z}{z_0}}, \tag{C.13}$$

$$B(r, \theta) = B(r) \cos\left(\theta - \beta ln\left(\frac{r}{r_0}\right)\right), \tag{C.14}$$

$$B(r) = \begin{cases} b_0 \dfrac{r_c}{r} & r \geqslant r_c \text{kpc} \\ b_0 & r < r_c \text{kpc} \end{cases}.$$

Here $r_0 = (R_{Sun} + d) e^{\tan pitch\, \pi/2}$. At a maximum distance of 20 kpc from the Galactic centre, the field is set to zero. In Jansson et al. (2007) a parameter scan for b_0, r_c and z_0 with $pitch = -10\,\text{deg}$ and $r_0 = 10.55\text{kpc}$ (following Stanev, 1997) is performed, however no unique best-fit parameters are found. As an exercise to test the fitting method, Jansson et al. (2007) generate a mock observation using the following values $b_0 = 3.5\mu\text{G}$, $r_c = 10\text{kpc}$, $z_0 = 1.15\text{kpc}$, $pitch = -10\,\text{deg}$ and $r_0 = 10.55\text{kpc}$, which they then attempt to recover. See Sect. 3.5.3 for details.

C.3.4 The Aumont model

This model is a refined version of the Page et al. (2007) one, and is presented in Aumont (2007). It is parametrised as

$$\vec{B}(r, \varphi, z) = B_0 \left[\cos(\varphi + \beta) ln(r/r_0) \sin p\, \cos\chi(z) \hat{r} + \right. \tag{C.15}$$

$$\left. - \cos(\varphi + \beta) ln(r/r_0) \cos p\, \cos\chi(z) \hat{\varphi} + \sin\chi(z) \hat{z}\right]. \tag{C.16}$$

Here $r_0 = 8\text{kpc}$.

Acknowledgements

Hurray! It's done! So, I would like to thank my supervisor Torsten, for giving me a chance in this business and for his patience and comprehension in those moments when my amazing organisation went out the window (such as when I was losing planes or forgetting the laptop in Ringberg). Also, he somehow stood my single mindedness, and with his intuition about physics pointed me the right way to avoid another week wasted at debugging some code! Furthermore, apart from some physics, he also thought me how to do snowball fights the German way.

I am also indebted to Alex Schekochihin. There is no way I could have finished this dissertation without his meticulous care about mathematics, which more than once proved to be the solution to the problem I was facing. I also benefited from his particularly clear thoughts and patience for explaining them.

I am also indebted to Martin Reinecke, whose expertise in C++ programming and the like were enormously helpful. Had he not been around to solve a problem of a week in 5min, this work would have been way harder (and would certainly have taken much longer!).

It was a great pleasure to work with Tess Jaffe on the Hammurabi code. I had but to ask, and a week latter whatever code I required was available and working!

I would also like to thank Ronnie "the Babylonian" Jansson for his invaluable assistance in testing the Hammurabi code.

I am also indebted to Matteo Maturi and his patience with an over-eager PhD student trying to publish his first paper.

I was fortunate to have a very fruitful collaboration with Xiaohui Sun and Wolfgang Reich. During our work on Xiaohui's paper, and his thorough bug-hunting the Hammurabi code underwent a field test which was paramount for obtaining the published version. Moreover, they have shown (also to me!), thanks to their expertise in fields I am not versed in, what could actually be achieved with the Hammurabi code.

I would also like to thank Simon White for granting me a shot at astrophysics, and for singing Christmas songs in Italian with me.

Also, I want to thank the good will and patience of our secretary staff: Maria, Cornelia and Gabi, without whom nothing here works.

I also want to thank my brothers in arms, currently or formerly at the MPA-ESO-MPE-IPP and other organisations, which helped me out with this thesis, and life in general by

being heroes, very cool, and occasionally providing food for me: Paola, Paula, Gloria Sala, Luis Carlos, Mona (super fanciulla) Frommert, Giovanni Tardini, Stuart (for lots of comedy moments wisdom and english translations), Team D'Angelo (for her woolly arguments and all that), Giulia Ventimiglia-Werner, Silvia, Magi, Mattia Righi, Umberto Maio (also for the PhD template and moments of comedy in general), Joern Dunkel, Bjoern M. Schaefer, Monique, Anna A. (for being simpatica), Luca R., Luca G. (for the moments of comedy), T. Jaffe, Prof. Dr. Anna L. Watts, Daniele Pierini (also for references on dust physics), N. Hammer (for lots of pdf, ps etc... tricks), Wang Jie, Wang Lan, Anja v.d.L., Michael B., Karina K., Marcelo M., Vivienne "Über da" Wild. I most certainly have forgotten someone! Sorry!!

Some other reasonably cool people are: Jeremy "factor 7" Blaizot, Eric and Dimitri "Jimmy Neutron" Gadotti.

Finally I would like to thank my parents and family, whose guidance and support are a totally awesome hyper important thing to have around!

André

Bibliography

Armstrong, J. W., Cordes, J. M., & Rickett, B. J. 1981, Nature, 291, 561

Armstrong, J. W., Rickett, B. J., & Spangler, S. R. 1995, ApJ, 443, 209

Aumont, J. 2007, PhD in astrophysiks, Laboratoire de Physique Subatomique et de Cosmologie de Grenoble, LPSC Grenoble

Baumann, D., Jackson, M. G., Adshead, P., et al. 2008, ArXiv e-prints

Beck, R. 2001, Space Science Reviews, 99, 243

Beck, R. 2008, arXiv:0804.4594

Beck, R., Brandenburg, A., Moss, D., Shukurov, A., & Sokoloff, D. 1996, ARA&A, 34, 155

Beck, R. & Gaensler, B. M. 2004, New Astronomy Review, 48, 1289

Beck, R., Shoutenkov, V., Ehle, M., et al. 2002, A&A, 391, 83

Berkhuijsen, E. M., Mitra, D., & Mueller, P. 2006, Astronomische Nachrichten, 327, 82

Beuermann, K., Kanbach, G., & Berkhuijsen, E. M. 1985, A&A, 153, 17

Biermann, L. 1950, Zeitschrift Naturforschung Teil A, 5, 65

Birkinshaw, M. 1999, Phys. Rep., 310, 97

Boldyrev, S. 2006, Phys. Rev. Lett., 96, 115002

Bottino, M., Banday, A. J., & Maino, D. 2008, arXiv:0807.1865

Brandenburg, A. & Subramanian, K. 2005, Phys. Rep., 417, 1

Brentjens, M. A. & de Bruyn, A. G. 2005, A&A, 441, 1217

Brown, J. C., Taylor, A. R., Wielebinski, R., & Mueller, P. 2003, ApJL, 592, L29

Burn, B. J. 1966, MNRAS, 133, 67

Carilli, C. L., Perley, R. A., & Harris, D. E. 1994, MNRAS, 270, 173

Carilli, C. L. & Taylor, G. B. 2002, ARA&A, 40, 319

Chandran, B. D. G. & Cowley, S. C. 1998, Phys. Rev. Lett., 80, 3077

Chyży, K. T., Beck, R., Kohle, S., Klein, U., & Urbanik, M. 2000, A&A, 355, 128

Clarke, T. E. & Ensslin, T. A. 2006, AJ, 131, 2900

Cordes, J. M. & Lazio, T. J. W. 2002, ArXiv Astrophysics e-prints

Cordes, J. M. & Lazio, T. J. W. 2003, ArXiv Astrophysics e-prints

de Oliveira-Costa, A., Tegmark, M., Gaensler, B. M., et al. 2008, MNRAS, 388, 247

de Oliveira-Costa, A., Tegmark, M., Zaldarriaga, M., & Hamilton, A. 2004, Phys. Rev. D, 69, 063516

Dineen, P. & Coles, P. 2005, MNRAS, 362, 403

Dolag, K., Hansen, F. K., Roncarelli, M., & Moscardini, L. 2005, MNRAS, 363, 29

Draine, B. T. & Lazarian, A. 1998, ApJL, 494, L19+

Drury, L. O. 1983, Rep. Prog. Phys., 46, 973

Dunkley, J., Komatsu, E., Nolta, M. R., et al. 2008, arXiv:0803.0586

Eilek, J. A. 1989a, AJ, 98, 244

Eilek, J. A. 1989b, AJ, 98, 256

Eilek, J. A. & Owen, F. N. 2002, ApJ, 567, 202

Enßlin, T. A. & Vogt, C. 2003, A&A, 401, 835

Enßlin, T. A. & Vogt, C. 2006, A&A, 453, 447

Enßlin, T. A., Waelkens, A., Vogt, C., & Schekochihin, A. A. 2006, Astron. Nachr., 327, 626

Finkbeiner, D. P., Davis, M., & Schlegel, D. J. 1999, ApJ, 524, 867

Fixsen, D. J., Cheng, E. S., Gales, J. M., et al. 1996, ApJ, 473, 576

Frick, P., Stepanov, R., Shukurov, A., & Sokoloff, D. 2001, MNRAS, 325, 649

Gaensler, B. M. 2006, Astron. Nachr., 327, 387

Gaensler, B. M., Dickey, J. M., McClure-Griffiths, N. M., et al. 2001, ApJ, 549, 959

Gaensler, B. M., Madsen, G. J., Chatterjee, S., & Mao, S. A. 2008, ArXiv e-prints, 808

Gaisser, T. K. & Stanev, T. 2004, Physics Letters B, 592, 228

Goldreich, P. & Sridhar, S. 1995, ApJ, 438, 763

Górski, K. M., Hivon, E., Banday, A. J., et al. 2005, ApJ, 622, 759

Govoni, F., Murgia, M., Feretti, L., et al. 2006, A&A, 460, 425

Greisen, K. 1966, Physical Review Letters, 16, 748

Guidetti, D., Murgia, M., Govoni, F., et al. 2008, A&A, 483, 699

Haehnelt, M. G. & Tegmark, M. 1996, MNRAS, 279, 545

Hajian, A., Hernandez-Monteagudo, C., Jimenez, R., Spergel, D., & Verde, L. 2007, astro-ph/0705.3245, 705

Han, J. 2002, in American Institute of Physics Conference Series, Vol. 609, Astrophysical Polarized Backgrounds, ed. S. Cecchini, S. Cortiglioni, R. Sault, & C. Sbarra, 96–101

Han, J. L., Ferriere, K., & Manchester, R. N. 2004, ApJ, 610, 820

Han, J. L., Manchester, R. N., Berkhuijsen, E. M., & Beck, R. 1997, A&A, 322, 98

Han, J. L., Manchester, R. N., Lyne, A. G., Qiao, G. J., & van Straten, W. 2006, ApJ, 642, 868

Han, J. L., Manchester, R. N., & Qiao, G. J. 1999, MNRAS, 306, 371

Han, J. L. & Qiao, G. J. 1994, A&A, 288, 759

Harari, D., Mollerach, S., & Roulet, E. 1999, Journal of High Energy Physics, 8, 22

Harari, D., Mollerach, S., & Roulet, E. 2000, Journal of High Energy Physics, 2, 35

Haslam, C. G. T., Klein, U., Salter, C. J., et al. 1981, A&A, 100, 209

Haslam, C. G. T., Salter, C. J., Stoffel, H., & Wilson, W. E. 1982, A&A Supp., 47, 1

Haugen, N. E., Brandenburg, A., & Dobler, W. 2004, Phys. Rev. E, 70, 016308

Haverkorn, M., Brown, J. C., Gaensler, B. M., & McClure-Griffiths, N. M. 2008, ApJ, 680, 362

Haverkorn, M., Gaensler, B. M., Brown, J. C., et al. 2006a, ApJL, 637, L33

Haverkorn, M., Gaensler, B. M., McClure-Griffiths, N. M., Dickey, J. M., & Green, A. J. 2006b, ApJS, 167, 230

Haverkorn, M., Katgert, P., & de Bruyn, A. G. 2003, A&A, 403, 1045

Heiles, C. 2000, AJ, 119, 923

Hinshaw, G., Nolta, M. R., Bennett, C. L., et al. 2007, ApJS, 170, 288

Hinshaw, G., Weiland, J. L., Hill, R. S., et al. 2008, ArXiv e-prints, 803

Hirata, C. M., Loeb, A., & Afshordi, N. 2005, Phys. Rev. D, 71, 063531

Hooper, D., Finkbeiner, D. P., & Dobler, G. 2007, Phys. Rev. D, 76, 083012

Howard, A. M. & Kulsrud, R. M. 1997, ApJ, 483, 648

Indrani, C. & Deshpande, A. A. 1999, New Astronomy, 4, 33

Iroshnikov, R. S. 1963, Astron. Zh., 40, 742

Jaegers, W. J. 1987, A&A Supp., 71, 603

Jansson, R., Farrar, G. R., Waelkens, A., & Enßlin, T. A. 2007, ArXiv e-prints, 708

Jelić, V., Zaroubi, S., Labropoulos, P., et al. 2008, MNRAS, 891

Johnston-Hollitt, M., Hollitt, C. P., & Ekers, R. D. 2004, in The Magnetized Interstellar Medium, 13–18

Kachelrieß, M., Serpico, P. D., & Teshima, M. 2007, Astroparticle Physics, 26, 378

Kitaura, F. S. & Ensslin, T. A. 2007, ArXiv e-prints, 705

Klypin, A., Zhao, H., & Somerville, R. S. 2002, ApJ, 573, 597

Kolmogorov, A. 1941, Akademiia Nauk SSSR Doklady, 30, 301

Kraichnan, R. H. 1965, Phys. Fluids, 8, 1385

Laing, R. A., Bridle, A. H., Parma, P., & Murgia, M. 2008, MNRAS, 391, 521

Larmor, J. 1919, in Reports of the 87th Meeting of the British Association for the Advancement of Science, ed. J. Murray, 159

Lazarian, A. 1992, Astronomical and Astrophysical Transactions, 3, 33

Lazarian, A. 2003, Journal of Quantitative Spectroscopy and Radiative Transfer, 79, 881

Lazio, T. J. W., Cordes, J. M., de Bruyn, A. G., & Macquart, J.-P. 2004, New Astronomy Review, 48, 1439

Lewis, A., Challinor, A., & Lasenby, A. 2000, ApJ, 538, 473

Markevitch, M., Mazzotta, P., Vikhlinin, A., et al. 2003, ApJL, 586, L19

Maturi, M., Dolag, K., Waelkens, A., Springel, V., & Ensslin, T. 2007, ArXiv e-prints, A&A accepted, 708

Maturi, M., Ensslin, T., Hernandez-Monteagudo, C., & Rubino-Martin, J. A. 2006, astro-ph/0602539

Maturi, M., Meneghetti, M., Bartelmann, M., Dolag, K., & Moscardini, L. 2005, A&A, 442, 851

McEwen, J. D., Hobson, M. P., & Lasenby, A. N. 2006, astro-ph/0612688

Miville-Deschenes, M. ., Ysard, N., Lavabre, A., et al. 2008, ArXiv e-prints, 802

Moss, D. & Shukurov, A. 1996, MNRAS, 279, 229

Moss, D. & Sokoloff, D. 2008, A&A, 487, 197

Narayan, R. & Medvedev, M. V. 2001, ApJL, 562, L129

Page, L., Hinshaw, G., Komatsu, E., et al. 2007, ApJS, 170, 335

Parker, E. N. 1970, ApJ, 162, 665

Parker, E. N. 1973, Ap&SS, 22, 279

Peterson, J. D. & Webber, W. R. 2002, ApJ, 575, 217

Pohl, M. & Esposito, J. A. 1998, ApJ, 507, 327

Price, D. J. & Bate, M. R. 2008, MNRAS, 385, 1820

Price, D. J., Bate, M. R., & Dobbs, C. L. 2008, ArXiv e-prints

Pringle, J. E. & Rees, M. J. 1972, A&A, 21, 1

Prouza, M. & Šmída, R. 2003, A&A, 410, 1

Quireza, C., Rood, R. T., Bania, T. M., Balser, D. S., & Maciel, W. J. 2006, ApJ, 653, 1226

Rand, R. J. & Kulkarni, S. R. 1989, ApJ, 343, 760

Rand, R. J. & Lyne, A. G. 1994, MNRAS, 268, 497

Reich, P. & Reich, W. 1986, A&A Supp., 63, 205

Reich, P. & Reich, W. 1988a, A&A Supp., 74, 7

Reich, P. & Reich, W. 1988b, A&A, 196, 211

Reich, P., Testori, J. C., & Reich, W. 2001, A&A, 376, 861

Reich, W. 2006, arXiv:astro-ph/0603465

Reynolds, R. J., Haffner, L. M., & Tufte, S. L. 1999, ApJL, 525, L21

Robertson, H. P. 1940, Proc. Camb. Philos. Soc., 36

Roettiger, K., Stone, J. M., & Burns, J. O. 1999, ApJ, 518, 594

Roger, R. S., Costain, C. H., Landecker, T. L., & Swerdlyk, C. M. 1999, A&A Supp., 137, 7

Rohlfs, K. & Wilson, T. L. 1996, Tools of Radio Astronomy (Tools of Radio Astronomy, XVI, 423 pp. 127 figs., 20 tabs.. Springer-Verlag Berlin Heidelberg New York. Also Astronomy and Astrophysics Library)

Russel M. Kulsrud. 2005, Plasma Physics for Astrophysics (Princeton University Press)

Ruzmaikin, A., Sokolov, D., & Shukurov, A. 1989, MNRAS, 241, 1

Rybicki, G. B. & Lightman, A. P. 1979, Radiative processes in astrophysics (New York, Wiley-Interscience, 1979.)

Schäfer, B. M., Pfrommer, C., Hell, R. M., & Bartelmann, M. 2006, MNRAS, 370, 1713

Schekochihin, A., Cowley, S., Maron, J., & Malyshkin, L. 2002, Phys. Rev. E, 65, 016305

Schekochihin, A. A. & Cowley, S. C. 2005, arXiv:astro-ph/0507686

Schekochihin, A. A. & Cowley, S. C. 2006, Phys. Plasmas, 13, 056501

Schekochihin, A. A. & Cowley, S. C. 2007, Turbulence and Magnetic Fields in Astrophysical Plasmas (Magnetohydrodynamics: Historical Evolution and Trends), 85–+

Schekochihin, A. A., Cowley, S. C., Dorland, W., et al. 2007, arXiv:0704.0044

Schekochihin, A. A., Cowley, S. C., Taylor, S. F., Maron, J. L., & McWilliams, J. C. 2004, ApJ, 612, 276

Schnitzeler, D. H. F. M., Katgert, P., Haverkorn, M., & de Bruyn, A. G. 2007, A&A, 461, 963

Schuecker, P., Finoguenov, A., Miniati, F., Böhringer, H., & Briel, U. G. 2004, A&A, 426, 387

Shakura, N. I. & Syunyaev, R. A. 1973, A&A, 24, 337

Simard-Normandin, M., Kronberg, P. P., & Button, S. 1981, ApJS, 45, 97

Sofue, Y. & Fujimoto, M. 1983, ApJ, 265, 722

Sokoloff, D. & Shukurov, A. 1990, Nature, 347, 51

Spangler, S. R. 1982, ApJ, 261, 310

Spangler, S. R. 1983, ApJL, 271, L49

Stanev, T. 1997, ApJ, 479, 290

Steenbeck, M., Krause, F., & Rädler, K. H. 1966, Zeitschrift Naturforschung Teil A, 21, 369

Strong, A. W., Moskalenko, I. V., & Ptuskin, V. S. 2007, Ann. Rev. Nucl. Particle Sci., 57, 285

Strong, A. W., Moskalenko, I. V., & Reimer, O. 2004, ApJ, 613, 962

Subramanian, K., Shukurov, A., & Haugen, N. E. L. 2006, MNRAS, 366, 1437

Sun, X. H., Reich, W., Waelkens, A., & Enßlin, T. A. 2008, A&A, 477, 573

Sunyaev, R. A. & Zeldovich, I. B. 1980, ARA&A, 18, 537

Sunyaev, R. A. & Zeldovich, Y. B. 1972, Comments on Astrophysics and Space Physics, 4, 173

Sur, S., Shukurov, A., & Subramanian, K. 2007, MNRAS, 377, 874

Tateyama, C. E., Abraham, Z., & Strauss, F. M. 1986, A&A, 154, 176

Taylor, A. R., Gibson, S. J., Peracaula, M., et al. 2003, AJ, 125, 3145

Tegmark, M. & Efstathiou, G. 1996, MNRAS, 281, 1297

The Pierre Auger Collaboration. 2007, Science, 318, 938

Tinyakov, P. G. & Tkachev, I. I. 2002, Astroparticle Physics, 18, 165

Tucci, M., Martínez-González, E., Vielva, P., & Delabrouille, J. 2005, MNRAS, 360, 935

Vallee, J. P. 1991, ApJ, 366, 450

Vallée, J. P. 2008, ApJ, 681, 303

Varshalovich, D. A., Moskalev, A. N., & Khersonskii, V. K. 1988, Quantum Theory of Angular Momentum (Quantum Theory of Angular Momentum, by D. A. Varshalovich, A. N. Moskalev, A. N. Kherosonskii, ISBN 9971-50-107-4. World Scientific Publishing Co Pte Ltd., 1988.)

Vogt, C. & Enßlin, T. A. 2003, A&A, 412, 373

Vogt, C. & Enßlin, T. A. 2005, A&A, 434, 67

Waelkens, A., Jaffe, T., Reinecke, M., Kitaura, F. S., & Enßlin, T. A. 2009a, A&A, 495, 697

Waelkens, A., Maturi, M., & Enßlin, T. 2008, MNRAS, 383, 1425

Waelkens, A., Schekochihin, A., & Enßlin, T. 2009b, Submitted to MNRAS

Westerhout, G., Seeger, C. L., Brouw, W. N., & Tinbergen, J. 1962, Bull. Astron. Inst. Ned., 16, 187

Westfold, K. C. 1959, ApJ, 130, 241

Widrow, L. M. 2002, Reviews of Modern Physics, 74, 775

Wielebinski, R., Shakeshaft, J. R., & Pauliny-Toth, I. I. K. 1962, The Observatory, 82, 158

Wolleben, M., Landecker, T. L., Reich, W., & Wielebinski, R. 2006, A&A, 448, 411

Yan, H. & Lazarian, A. 2006, ApJ, 653, 1292

Yan, H. & Lazarian, A. 2008a, ApJ, 677, 1401

Yan, H. & Lazarian, A. 2008b, ApJ, 673, 942

Zatsepin, G. T. & Kuz'min, V. A. 1966, Soviet Journal of Experimental and Theoretical Physics Letters, 4, 78

Refereed publications

- *Probing magnetic turbulence by synchrotron polarimetry: the tension-force spectrum from Stokes correlators*
  Waelkens A., Schekochihin A., Enßlin T.
  2009, MNRAS Submitted

- *Simulating polarized Galactic synchrotron emission at all frequencies, the Hammurabi code*
  Waelkens A., Jaffe T., Reinecke M., Kitaura F., Enßlin T.
  2009, A&A, 495, 697

- *Radio observational constraints on Galactic 3D-emission models*
  Sun X. H., Reich W., **Waelkens A.**, Enßlin T.
  2008, A&A, 477, 573

- *Camouflaged Galactic cosmic microwave background polarization foregrounds: total and polarized contributions of the kinetic Sunyaev-Zeldovich effect*
  Waelkens A., Maturi M., Enßlin T.
  2007, MNRAS, 383, 1425

- *The actual Rees-Sciama effect from the local universe*
  Maturi M., Dolag K.,**Waelkens A.**, Springel V., Enßlin T.
  2007, A&A, 476, 83

- *Future magnetic field studies using the Planck surveyor experiment*
  Enßlin T., **Waelkens A.**, Vogt C., Schekochihin A.,
  2006, AN, 327, 626

André Henri Waelkens

Born on the 08 Dec 1980 in São Paulo, Brazil

Research Interests

- astrophysical plasmas
  - Galactic magnetised inter-stellar-medium modeling
  - measuring magneto-hydro-dynamic properties of the turbulent magnetised ISM
- Galactic CMB foregrounds

Research Experience and Education

2006-2009 (expt)	**Ph.D.**, Ludwig-Maximilians Universität Thesis: *Studying MHD turbulence using radio astronomical tools* Supervisors: Dr. Torsten Enßlin and Prof. Simon White
2004-2005	**Diplom-Physiker**, Ludwig-Maximilians Universität Thesis: *Models of polarized synchrotron emission as a CMB foreground* Supervisors: Dr. Torsten Enßlin and Prof. Simon White
2000-2004	**B.S. Physics**, Universidade de São Paulo
1999	**Abitur**, Colégio Visconde de Porto Seguro, São Paulo

Teaching Experience

Mathematics support classes for minors with refugee status,
BMF (Betreung für Minderjährige Flüchtlinge) in Munich, 2007–2009

Language skills

Fluent: English, Portuguese, German

Intermediate: French, Italian

Outside Interests

Basketball - Fishing - Cooking